# Vortex-induced Vibration of Slender Structures in Unsteady Flow

by

## Jung-Chi Liao

M.S. Mechanical Engineering (1998)
Massachusetts Institute of Technology

B.S. Mechanical Engineering (1993)
National Taiwan University

Submitted to the Department of Mechanical Engineering in
Partial Fulfillment of the Requirements for the Degree of
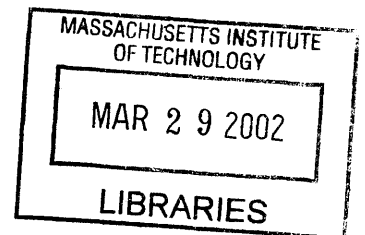Doctor of Philosophy

at the

Massachusetts Institute of Technology

February 2002

© 2001 Jung-Chi Liao. All rights reserved.

Signature of Author:_____

<div align="right">
Department of Mechanical Engineering
October 1, 2001
</div>

Certified by: _____

<div align="right">
J. Kim Vandiver
Professor of Ocean Engineering
Thesis Supervisor
</div>

Accepted by:_____

<div align="right">
Ain A. Sonin
Professor of Mechanical Engineering
Chairman, Department Committee on Graduate Students
</div>

# Vortex-induced Vibration of Slender Structures in Unsteady Flow

by

## Jung-Chi Liao

Submitted to the Department of Mechanical Engineering on
October 1, 2001 in Partial Fulfillment of the Requirements
for the Degree of Doctor of Philosophy

## Abstract

Vortex-induced vibration (VIV) results in fatigue damage of offshore oil exploration and production structures. In recent years, the offshore industry has begun to employ curved slender structures such as steel catenary risers in deep-water offshore oil systems. The top-end vessel motion causes the slender riser to oscillate, creating an unsteady and non-uniform flow profile along the riser. The purpose of this research is to develop a VIV prediction model for slender structures under top-end periodic motions. The key approach to this problem requires identifying the dimensionless parameters important to the unsteady VIV.

A set of data from a large-scale model test for highly compliant risers conducted by industry is available. The spectral analysis of the data showed a periodic pattern of the response frequencies. A constant Strouhal (St) number model was proposed such that shedding frequencies change with local inline velocities. The Keulegan-Carpenter number (KC) controls the number of vortex pairs shed per cycle. A KC threshold larger than 40 was found to have significant response for a long structure with finite length excitation region. An approximate solution to the response of an infinite beam with a finite excitation length was obtained; this solution provided an explanation for the high KC threshold. A model for an equivalent reduced damping Sg under a non-uniform, unsteady flow was proposed. This equivalent reduced damping Sg was used to establish a prediction model for the VIV under top-end periodic motions. A time domain simulation of unsteady VIV was demonstrated by using Green's functions. The turning point problem wave propagation was solved for a pipe resting on a linearly varying stiffness foundation. Simple rules were established for conservative estimation of TDP fatigue damage with soil interactions. Guidelines for model test experiment design were provided based on dimensional analysis and scaling rules.

Thesis Supervisor: J. Kim Vandiver

Title: Dean of Undergraduate Research
      Professor of Ocean Engineering

# Acknowledgements

First, I would like to take this opportunity to thank my thesis supervisor, Professor J. Kim Vandiver. It is my great pleasure to work with him. He provided me the ability of engineering thinking rather than mathematical thinking. This will be a treasure for my entire professional career. He also guided me to approach the important problem in the field. I thank him for all the effort to enhance my physical sense.

Also, I would like to thank my committee members, Professor T. R. Akylas in Mechanical Engineering and Professor E. Kausel in Civil Engineering. They gave me great support and guidance in the committee meetings. Professor Akylas served as the chair of the committee and I would like to thank him for his encouragement. Professor M. S. Triantafyllou helped me in the first committee meeting and gave suggestions in the research direction. Thank Professor H. Cheng for his time in the discussion of the asymptotic method. Thank Professor A. Whittle for the discussion of soil properties. Thank Dr. R. Rao for the discussion of the signal processing in wave propagation.

I would like to thank my group mates Dr. Yongming Cheng, Dr. Enrique Gonzalez, and Chadwick T. Musser. They are good friends and provided supports in the research. Thank my Taiwanese friends Prof. Yu-Hsuan Su, Dr. Juin-Yu Lai, Dr. Koling Chang, Dr. Su-Ru Lin, Dr. Ginger Wang, Dr. Chen-Pang Yeang, Chen-Hsiang Yeang, Ching-Yu Lin, Chung-Yao Kao, Yi-San Lai, Hui-Ying Hsu, Shyn-Ren Chen, Yi-Ling Chen, Dr. Steve Feng, Te-San Liao, Mrs. Su, Dr. Sean Shen, Dr. Yu-Feng Wei, Bruce Yu, Jung-Sheng Wu, Rei-Hsiang Chiang, Flora Sun, Chun-Yi Wang, Dr. Ching-Te Lin for their supports during the time of my doctoral study.

Finally, I would like to thank my fiancée Kai-Hsuan Wang, for her endless love and support in this period of time. She gave me all the encouragements to accomplish this work. And I would like to thank my dear parents, for their long-distance love and support to help me facing all the difficulties. This thesis is dedicated to them, my dearest parents.

# Table of Contents

# Chapter 1 Introduction

## 1.1 Problem Statement

Vortex-induced vibration (VIV) is an important source of fatigue damage of offshore oil exploration and production risers. These slender structures experience both current flow and top-end vessel motions, which give rise to the flow-structure relative motion and cause VIV. The top-end vessel motion causes the riser to oscillate and the corresponding flow profile appears unsteady. In recent years, the industry has begun to employ curved slender structures such as steel catenary risers in deep-water applications. The configurations of the curved structures determine the flow profiles along the structures and therefore affect the VIV fatigue damage rates. Also, these long slender structures tend to have low fundamental frequencies, so VIV of these long structures is often in higher modes, e.g., 30th mode or even 100th mode. At these high modes with hydrodynamic damping, the dynamic response is often propagating waves rather than standing waves.

This thesis focuses on vortex-induced vibration problems for slender structures under unsteady flow situations. The unsteady flow here is confined to cases involving the top-end periodic motion of the structure. The purpose of understanding the VIV behavior is to estimate the fatigue damage rate of structures. Three typical configurations of slender risers used in industry are shown in Figures 1.1 to 1.3: the Combined Vertical Axis Riser, or CVAR (Figure 1.1), the Lazy Wave Steel Catenary Riser, or LWSCR (Figure 1.2), and the Steel Catenary Riser, or SCR (Figure 1.3). These three configurations were evaluated in a model test conducted by PMB/Bechtel in 1998. Under top-end periodic excitation of the CVAR model, examples of inline acceleration at one location and the spatial variation of the velocity along the riser are shown in Figures 1.4 and 1.5. As can be seen in these figures, the flow is both non-uniform and unsteady. The principal goal of this thesis is to develop a VIV prediction model for slender structures under top-end periodic motions based on available data, considering the effects of the non-uniform, unsteady flow and very high mode number. In order to achieve this goal, we have to identify important dimensionless parameters with respect to the unsteady problem and use these parameters

to characterize the dynamic behavior of the VIV response. Using dimensionless parameters, we can extend the results from the available tests to predict the motion of new structures.
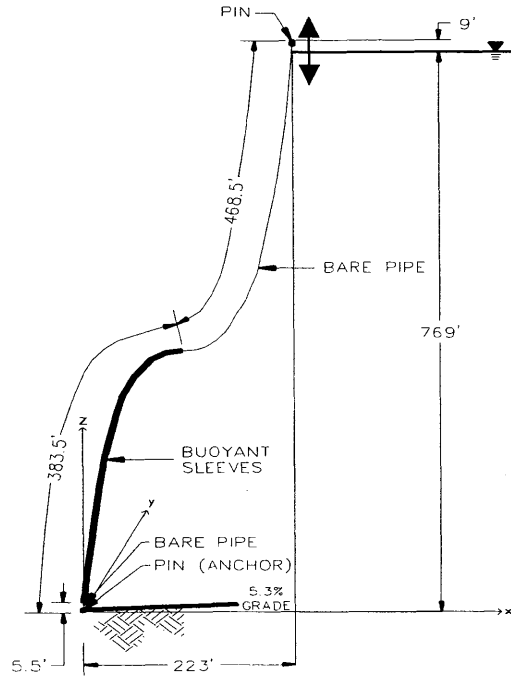


Figure 1.1. Combined Vertical Axis Riser (CVAR).

10
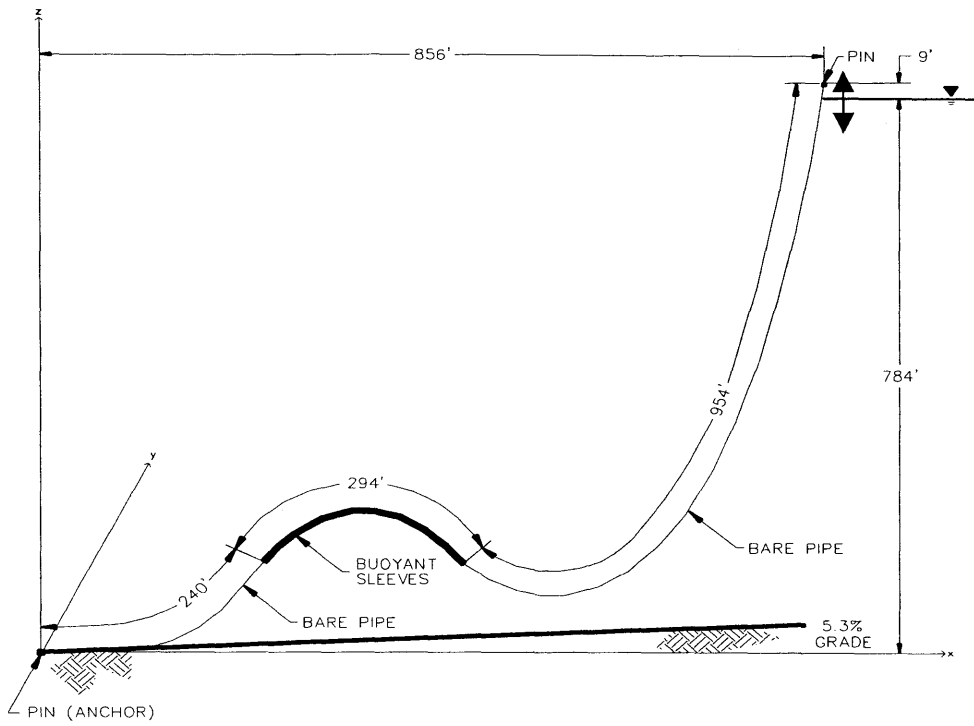
Figure 1.2. Lazy Wave Steel Catenary Riser (LWSCR).
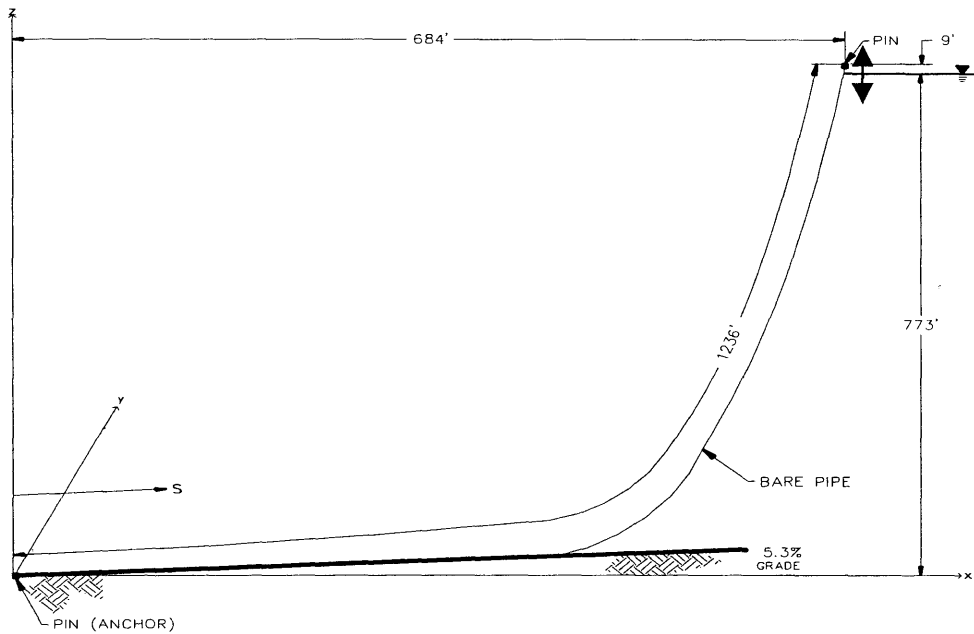


Figure 1.3. Steel Catenary Riser (SCR).

11
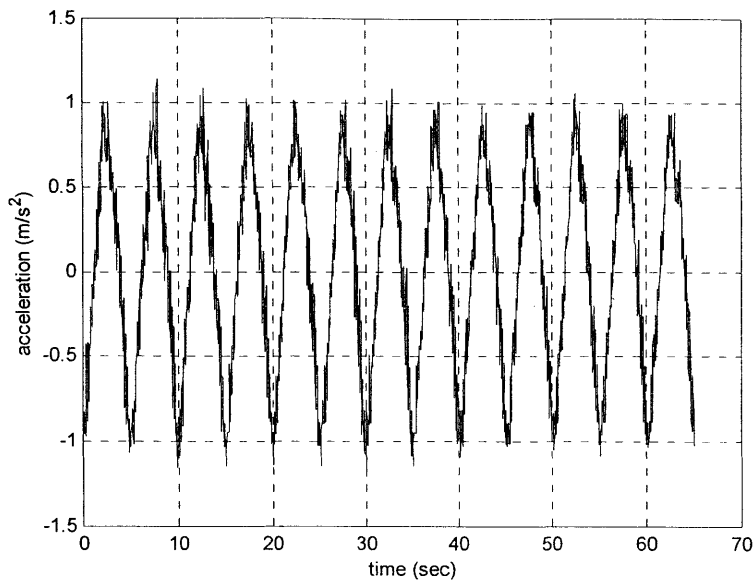
Figure 1.4. Acceleration time series in the in-plane direction for top-end amplitude 2 ft, top-end period 5 sec, at pup 3.
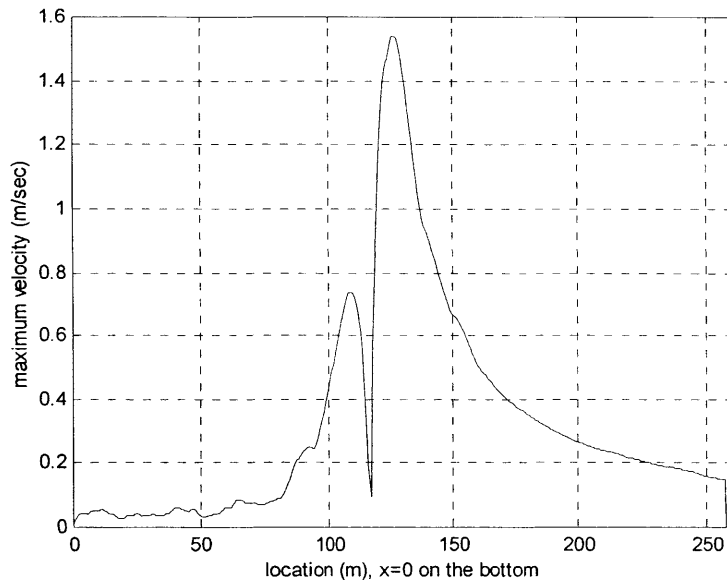


Figure 1.5. The flow profile of the maximum velocities along CVAR. Top-end motion: sinusoidal with A=3 ft and T=3 sec.

In addition to the major goal of developing the unsteady VIV model, we explore other important issues as shown in Figures 1.1 to 1.3. 1). Top-end periodic motion is a problem with a moving boundary condition. We explore the moving boundary effects for the

system. 2). The effects of the structural discontinuity between the buoyant pipe and the bare pipe will be investigated. 3). At the sea floor, the influence of the soil interactions on the riser dynamics will be studied.

**1.2 Overview of the Thesis**

Chapter 2 provides the background for this research. Section 2.1 identifies the dimensionless parameters related to the unsteady VIV problem. Section 2.2 introduces the available data from industry. The data will be analyzed later in the thesis. Section 2.3 reviews the research related to steady VIV and the wave-induced vibrations.

Chapter 3 discusses the dispersion relations for the systems we are interested in. The knowledge of the dispersion relation is very important for understanding the wave behavior later. Section 3.1 elaborates on the derivation of the dispersion relations. Section 3.2 discusses the root loci for the dispersion relations of several model systems. Section 3.3 verifies of the dispersion relations between measurements and theoretical results.

Chapter 4 explores the effects of varying material properties and boundary conditions, which include structural discontinuities and soil interactions. Section 4.1 introduces the cutoff frequency. Section 4.2 develops the WKB method to solve the system with spatial-varying properties. Section 4.3 develops the mathematical tools to solve the varying foundation stiffness problem. Section 4.4 analyzes the data for the effects of material discontinuity and soil interactions. Section 4.5 compares different soil interaction models and provides the guidelines to simplify the problem.

Chapter 5 establishes the unsteady VIV model by developing the equivalent reduced damping for non-uniform, unsteady flow. Section 5.1 reviews the approach to be used and previews the final results. Section 5.2 discusses the influence of the top-end periodic motion on the inline amplitudes along the riser. Section 5.3 gives examples to demonstrate the physical meaning of the reduced damping and the effects of the power-in

length. Section 5.4 establishes an excitation frequency model for unsteady VIV. Section 5.5 discusses the importance of the KC number. Section 5.6 demonstrates the procedure of solving for the unsteady VIV of a spring-mounted cylinder, by using the concept of reduced damping. Section 5.7 develops the equivalent reduced damping model for the unsteady VIV. Section 5.8 illustrates the relationship between the RMS A/D and the equivalent reduced damping. Section 5.9 uses the non-dimensional frequency to explain the observed results from model tests. Section 5.10 describes the procedure of predicting the fatigue damage rate based on the equivalent reduced damping.

Chapter 6 summarizes this thesis. Section 6.1 discusses the insights we have gained from this research. Section 6.2 provides guidelines for model test design by scaling laws. Section 6.3 lists the new contributions of this thesis, while Section 6.4 suggests future research directions.

# Chapter 2 Background

Before entering into the details of the unsteady VIV problem, we need to understand some background knowledge useful for later theoretical developments and experimental data analysis. The dimensional analysis will include the introduction of all dimensionless parameters important to unsteady VIV. The review of the steady current VIV problem and the wave-induced vibration problem provides the direction in which we should proceed for analysis of the unsteady VIV problem.

## 2.1 Dimensional Analysis

Dimensional analysis enables us to find the dimensionless parameters related to the problem of interest, and also facilitates the scaling between the prototype and the model test. First we list the variables associated with the VIV problem of a slender cylinder in water under a top-end periodic motion excitation. This slender cylinder can be modeled as a tensioned beam with structural damping. These variables and their units are listed in Table 2.1.

Table 2.1. The independent variables related to the unsteady VIV under the top-end periodic motion.

| Fluid | | Structure | | | | | |
|---|---|---|---|---|---|---|---|
| Density | Viscosity | Mass/Length | Young's Modulus | Moment of Inertia | Damping Ratio | Diameter | Length |
| $\rho_f$ | $\mu$ | $m$ | $E$ | $I$ | $\varsigma_s$ | $D$ | $L$ |
| $ML^{-3}$ | $ML^{-1}T^{-1}$ | $ML^{-1}$ | $ML^{-1}T^{-2}$ | $L^4$ | 1 | L | L |

| Others | | | Top-end Excitation | | Soil |
|---|---|---|---|---|---|
| Water Depth | Top Tension | Gravity | Amplitude | Frequency | Stiffness/Length |
| $h$ | $T$ | $g$ | $A$ | $f_{ext}$ | $K$ |
| L | $MLT^{-2}$ | $LT^{-2}$ | L | $T^{-1}$ | $ML^{-1}T^{-2}$ |

There are 14 variables in total for the system. In this table, Young's modulus and the moment of inertia always come together as the bending stiffness, so we can regard $EI$ as one variable, and the number of variables becomes 13. With the Pi theorem, we are able to reduce the variables to 10 dimensionless parameters that characterize this problem. A variable that is frequently used in the dimensional analysis for fluids is flow velocity. We use the magnitude of the top-end periodic velocity, defined as

$$V_0 = 2\pi f_{ext} A,$$

to substitute the top-end excitation frequency. The dimension of $V_0$ is $LT^{-1}$. There are many possible combinations of these parameters to create 10 dimensionless groups. One set of 10 dimensionless groups is:

$$\frac{\mu}{\rho_f V_0 D}, \frac{m}{\rho_f D^2}, \frac{EI}{\rho_f V_0^2 D^4}, \varsigma_s, \frac{L}{D}, \frac{h}{D}, \frac{T}{\rho_f V_0^2 D^2}, \frac{gD}{V_0^2}, \frac{A}{D}, \frac{K}{\rho_f V_0^2}. \qquad (2.1)$$

Some groups are well known. For example, we introduce the top-end maximum Reynolds number as

$$Re_0 = \frac{\rho_f D V_0}{\mu}. \qquad (2.2)$$

Because the top-end motion is sinusoidal, the Reynolds number may change with time, but the defined $Re_0$ is a constant. Mass ratio is expressed as $\dfrac{m}{\rho_f D^2}$, comparing the mass per unit length of the structure and of the fluid. A physically meaningful mass ratio should include the added mass effect in the numerator. The added mass per unit length can be written as

$$m_a = C_m \rho_f \pi \frac{D^2}{4}, \qquad (2.3)$$

where $C_m$ is the added mass coefficient, affected by the shape of the structure and the dynamics of the fluid. The total mass per unit length is

$$m_t = m + m_a. \qquad (2.4)$$

16

Thus, the mass ratio $\dfrac{m_t}{\rho_f D^2}$ is physically important, while the $\dfrac{m}{\rho_f D^2}$ can be obtained

without knowing the details of the hydrodynamics (good for scaling). For the

dimensionless parameter with respect to tension (written as $\dfrac{T}{\rho_f V_0^2 D^2}$ above), we should

consider the geometric shape of a catenary riser. The solution of the shape for a catenary
cable is

$$y = \frac{T_0}{mg}(\cosh\frac{mgx}{T_0} - 1), \tag{2.5}$$

where $T_0$ is the horizontal tension of the cable. Thus, a physically meaningful

dimensionless parameter is $\dfrac{T}{mgD}$, which controls the static shape of the riser. For the

dimensionless parameter with respect to the bending stiffness $EI$, a better expression is to

compare the relative importance between the bending effect and the tension effect. If the

bending effect dominates, we can apply a beam model for the problem, while if the

tension effect dominates, we can use a string model. The term $\dfrac{EI\gamma^2}{T}$ represents the

comparison between bending and tension, where $\gamma$ is the wave number for the

propagating wave, written as

$$\gamma = \sqrt{\frac{-T + \sqrt{T^2 + 4mEI(2\pi f)^2}}{2EI}}. \tag{2.6}$$

From this equation, we see that it is required to know the vibration frequency $f$ in order to

obtain the wave number. Without knowing the response, we can still express the ratio as

$\dfrac{EI}{TD^2}$ to be one dimensionless parameter. The Froude number (Fr) is introduced as

$$Fr = \frac{V_0}{\sqrt{gD}}, \tag{2.7}$$

which is a ratio of the inertial effect to the gravitational effect. For a horizontal riser

moving vertically in the fluid, this parameter expresses the relative importance of the

hydrodynamic force and the hydrostatic force. The Keulegan-Carpenter number (KC),

defined as

17

$$KC = \frac{2\pi A}{D}, \qquad (2.8)$$

is used to characterize the top-end amplitude of the excitation. Under a top-end periodic excitation, the local amplitudes along the riser vary depending on the top-end amplitude. We can also define the KC number in terms of any local velocity so that the KC number will be a spatially varying dimensionless parameter. Finally, a dimensionless parameter is needed to express the effects of the soil stiffness. For a tensioned beam on an elastic foundation, there is a cutoff frequency corresponding to the soil stiffness:

$$f_{cut} = \frac{1}{2\pi} \sqrt{\frac{K}{m_t}}, \qquad (2.9)$$

where $K$ is the soil stiffness per unit length, and $m_t$ is the total mass per unit length. The comparison between the cutoff frequency and the wave frequency, or the ratio $\dfrac{f}{f_{cut}}$, is important to determine the behavior of the wave propagation. Without knowing the response, we can define an alternative dimensionless parameter as $\dfrac{V_0/D}{\sqrt{K/m}}$ to characterize the effects of the soil stiffness. To sum up, the following 10 dimensionless parameters specify the fluid properties, the structural properties, and the excitation:

$$Re_0, \frac{m}{\rho_f D^2}, \frac{EI}{TD^2}, \varsigma_s, \frac{L}{D}, \frac{h}{D}, \frac{T}{mgD}, Fr, KC, \frac{V_0/D}{\sqrt{K/m}}. \qquad (2.10)$$

All the above parameters are independent variables to fully characterize the problem. Here we discuss some more dimensionless parameters important to the unsteady VIV. These parameters are functions of some of the parameters shown in Equation 2.10. The significance of these dimensionless parameters will be demonstrated in this thesis. First, to define these parameters, the maximum normal velocity along the riser is more important that the top-end maximum velocity. The location where the local maximum normal velocity occurs depends on the riser configuration. We note $V_{max}$ as the maximum normal velocity. The dimensionless parameters Re, Fr, and KC can also be defined by the maximum normal velocity, and are noted as $Re_{max}, Fr_{max,}$ and $KC_{max}$. Several physically meaningful variables regarding these dimensionless parameters are the natural frequency,

the vortex shedding frequency, and the response (vibration) frequency. For a tensioned beam with pinned-pinned boundary conditions, the formula for the natural frequency is

$$f_{nat} = \frac{1}{2\pi} \sqrt{\frac{EI}{m_t}(\frac{n\pi}{L})^4 + \frac{T}{m_t}(\frac{n\pi}{L})^2}, \qquad (2.11)$$

where $m_t$ is the total mass per unit length. This natural frequency formula is valid for a tensioned beam with a constant tension and a constant bending stiffness. For a tensioned beam with spatially varying properties, the natural frequency will be more complicated, but the combined effect of $EI$, $T$, and $m_t$ will be similar. The ratio between the response frequency and the natural frequency, $\frac{f}{f_n}$, tells which mode the response frequency corresponds to, and we can also use response mode number $n$ as a dimensionless parameter. For the vortex shedding frequency, it is necessary to introduce the Strouhal number (St). The St number for a uniform flow is defined as

$$St = \frac{f_s D}{V}, \qquad (2.12)$$

where $f_s$ is the shedding frequency, and $V$ is the flow velocity. In general, St is a function of mass ratio, Re and KC. The St relationship for the unsteady flow problem will be explored in the later part of the thesis, while from Equation 2.12 we that infer the shedding frequency will be a function of the diameter and the flow velocity even for unsteady VIV. The response frequency is influenced by the shedding frequency. The non-dimensional frequency, defined as $\frac{fD}{V_{max}}$ and specified here as $f_{nd}$, is an important parameter closely related to the St number. Notice that this parameter is defined by the vibration frequency rather than the shedding frequency in St. The non-dimensional frequency is the inverse of the reduced velocity, and we will use this parameter to discuss the analyzed results in Chapter 5.

The lift coefficient, defined by

$$C_L = \frac{F_L}{\frac{1}{2}\rho_f D V^2}, \qquad (2.13)$$

19

is used to specify the excitation force in the VIV direction (the transverse direction). Similarly, the drag coefficient, defined as

$$C_D = \frac{F_D}{\frac{1}{2}\rho_f D V^2},$$  (2.14)

controls the riser motion in the inline direction. The hydrodynamic damping ratio $\varsigma_h$, determined by various damping models and influenced by the flow velocity, the vibration frequency, and the response amplitude, is also a very important dimensionless parameter. The effects of the structural damping and the hydrodynamic damping always come together, so we write the combination as

$$\varsigma = \varsigma_s + \varsigma_h,$$  (2.15)

where $\varsigma$ is the total damping ratio. The reduced damping, defined for the steady VIV problem as

$$S_g = \frac{R\omega}{\rho_f V^2},$$  (2.16)

will be employed in the response prediction of the unsteady case and is defined carefully there. The term $R$, the damping coefficient per unit length including the effects of the structural damping and the hydrodynamic damping, can be written as:

$$R = 2m_t\omega\varsigma.$$  (2.17)

The reduced damping $S_g$ expresses the relative importance of the energy consumption and the energy entering the system. In Chapter 5, we will show the significance of this parameter in a steady flow and extend the results to the unsteady flow problem. The product of the mode number and the damping ratio $n\varsigma$, also called the wave propagation parameter, is a critical parameter to determine whether we should use a modal model or a wave model to approach the problem. Later in the thesis we will also show that this parameter is essential for analyzing the moving boundary effects of the top-end periodic excitation. One more important parameter is the length ratio of the power-in region, $\frac{L_{power-in}}{L}$. The power-in length is controlled by the riser configuration, and all the known geometrical related parameters can determine the riser configuration. Another way to represent the power-in length is by the number of wavelengths in the power-in region,

noted as $N_{in}$. We will show that the product $N_{in}\varsigma$ is essential to specify the effects of the finite length power input.

In summary, the physically meaningful dimensionless parameters are as follows:

$$Re_0, \frac{m_t}{\rho_f D^2}, \frac{EI\gamma^2}{T}, \frac{L}{D}, \frac{h}{D}, \frac{T}{mgD}, Fr, KC, \frac{f}{f_{cut}}, St, f_{nd}, C_L, C_D, S_g, n\varsigma, N_{in}\varsigma. \quad (2.18)$$

## 2.2 Available Data

A large-scale model test for highly compliant risers (HCR) has been conducted by PMB/Bechtel under a joint industry project. The experiments were performed at a lake without significant current flows. Three different riser configurations were tested: the Combined Vertical Axis Riser, or CVAR (Figure 1.1), the Lazy Wave Steel Catenary Riser, or LWSCR (Figure 1.2), and the Steel Catenary Riser, or SCR (Figure 1.3). The configurations of LWSCR and CVAR were formed with the buoyant pipes installed in specific portions of the risers. Excitation was sinusoidal at the top end of each riser. Several excitation amplitudes and periods were conducted for each configuration. The directions of the excitation were mostly vertical, except for the tests of SCR configuration in which the directions were vertical, transverse horizontal, and 45° horizontal. Eight sets of sensors were installed along the riser for each configuration. Each set of sensors was mounted in a short tube, which was called a 'pup'. Each pup contained 2 accelerometers in the in-plane direction (in the plane of the curvature) and 2 accelerometers in the out-of-plane direction (perpendicular to the in-plane direction). Each sensor had 2 strain gages in both directions at the middle of the pup.

The sinusoidal excitation at the top caused the whole riser to oscillate, and the relative velocity between the riser and water generated vortices that induced vibrations mainly in the direction perpendicular to the flow direction. For example, when the SCR (Figure 1.3) was excited vertically with a sinusoidal motion of amplitude A and period T, the whole riser oscillated with period T in the plane of the curvature. The amplitudes of the sinusoidal motions along the riser depended on the catenary shape. At each location, the vortices generated by the relative motion in the in-plane direction induced vibration in the

out-of-plane direction. The relative velocity between the riser and water in the in-plane direction was basically sinusoidal. This varying velocity is different from the velocity in a steady current case, where the vortex patterns follow the Strouhal relationship. It is therefore a challenge to figure out the VIV frequency content for this unsteady problem.

The 8 sets of sensors (pups) were connected to the risers in different locations for each configuration. Table 2.2 shows the locations of all pups in 3 configurations. Pup 7 was out of order during the test, so we will omit it for the later analysis. It can be seen that one pup was close to the top of the SCR, while the other pups for the SCR and all the pups for LWSCR and CVAR were located in the middle portion of the risers.

Table 2.2. Distance (ft) from anchor to top of each sensor for three configurations.

| Pup number | CVAR | LWSCR | SCR |
|---|---|---|---|
| On anchor | 5.5 | 5.5 | 5.5 |
| Pup8 | 331.5 | 487.5 | 259.5 |
| Pup 7 | 357.5 | 513.5 | 285.5 |
| Pup 6 | 371.5 | 527.5 | 311.5 |
| Pup 5 | 385.5 | 541.5 | 325.5 |
| Pup 4 | 399.5 | 555.5 | 339.5 |
| Pup 3 | 413.5 | 569.5 | 353.5 |
| Pup 2 | 427.5 | 583.5 | 379.5 |
| Pup 1 | 453.5 | 609.5 | 1221.5 |
| On top | 849.5 | 1485.5 | 1233.5 |

An impulse response test was also conducted by hitting a point close to the top end of the riser with a heavy hammer. This test is called the 'whack test'. This test is useful to understand the wave propagation behavior of the riser and to determine the measured dispersion relation for the riser.

## 2.3 Previous Research

The VIV problem for a flexible cylinder under uniform flow has been extensively studied (Griffin, 1985, Sarpkaya, 1979, Bearman, 1984). Hartlen and Currie (1970) provided a lift-oscillator model to approach the lock-in behavior of VIV. A VIV program SHEAR 7, developed by Prof. Vandiver in MIT group, is used in industry mostly for fatigue damage rate estimation under steady shear current. Some of the previous knowledge concerning this topic is included in this program as well as in Vandiver's work (1993).

For VIV under unsteady current, several experiments were carried out for structures under sinusoidal oscillatory flow or sinusoidal oscillating structures in still water. To see the vortex patterns in oscillatory flow, Williamson (1985), and Williamson and Roshko (1988) used flow visualization techniques to capture the evolution of the vortices near the structure. Sarpkaya (1976, 1986) and Justesen (1989) measured forces under oscillatory flow in the range of 1-30 for KC number. Sumer and Fredsoe (1988) tested VIV of a free cylinder in waves. For VIV of curved structures or inclined structures, very little research has been conducted up to now. Kozakiewicz et al. (1995) studied the influence of oblique attack of current flow. Triantafyllou (1991) reported the dynamic response of curved cable structures under added mass and drag force effects. Bearman *et al.* (1984) proposed a frequency varying forcing model for the harmonically oscillating flow. Ferrari and Bearman (2000) modified the original model and carried out numerical simulations. Blevins' book (1990) provided a thorough and compact resource for a variety of flow-induced vibration topics.

# Chapter 3 Dispersion Relation

## 3.1 Derivation of the Dispersion Relation

The governing equation for a damped tensioned beam (Bernoulli-Euler beam) on an elastic foundation is:

$$\frac{\partial^2}{\partial x^2}\left(EI\frac{\partial^2 y}{\partial x^2}\right) - \frac{\partial}{\partial x}\left(T\frac{\partial y}{\partial x}\right) + m\frac{\partial^2 y}{\partial t^2} + c\frac{\partial y}{\partial t} + ky = q(x,t), \tag{3.1}$$

where $y$ is the response at location $x$ and time $t$, $E$ is the Young's modulus, $I$ is the moment of inertia, $T$ is the tension, $m$ is mass per unit length, $c$ is the linear damping coefficient, $k$ is the elastic foundation stiffness per unit length, and $q$ is the excitation force. We first assume all the coefficients here are constant, and by plugging in a plane wave solution with the form $Ae^{i(\gamma x - \omega t)}$, a dispersion relation can be obtained as:

$$EI\gamma^4 + T\gamma^2 - m\omega^2 - ic\omega + k = 0. \tag{3.2}$$

There are four solutions for the wave numbers of this equation:

$$\gamma = \pm\left\{\frac{-T \pm \left[T^2 - 4EI\left(-m\omega^2 - ic\omega + k\right)\right]^{\frac{1}{2}}}{2EI}\right\}^{\frac{1}{2}}. \tag{3.3}$$

Thus, the wave numbers are functions of wave frequency, and there are four possible wave components for this governing equation. If the bending stiffness term is negligible compared with the tension term, that is, the system can be modeled as a string problem, then the dispersion relation can be written as:

$$T\gamma^2 - m\omega^2 - ic\omega + k = 0, \tag{3.4}$$

and the wave number solutions are:

$$\gamma = \pm\left(\frac{m\omega^2 + ic\omega - k}{T}\right)^{\frac{1}{2}}, \tag{3.5}$$

where we have only two wave components for the problem. In the following discussion, the wave numbers will be used to identify the behavior of the waves and also to obtain the Green's function solutions.

## 3.2 Root Loci for the Dispersion Relation

As can be seen from equations 3.3 and 3.5, wave numbers are generally complex. The real part of the wave number determines the wave propagating direction and the wavelength, while the imaginary part gives the spatial decay or growth of the wave amplitude. Thus, it is important to understand the effects of the structural properties on the wave number, and how it varies with frequency. One way of seeing this is to plot the root loci in the complex $\gamma$ domain for changing frequencies. The locations of roots in the complex wave number, $\gamma$, domain are important when calculating the Green's function for a harmonic excitation, as will be seen in Chapter 5. The problems are classified into 12 categories depending on the presence of terms, as shown in Table 3.1.

Table 3.1 Dispersion relations for the 12 classified categories.

| | String | Beam | Tensioned beam |
|---|---|---|---|
| no spring no damping | $T\gamma^2 - m\omega^2 = 0$ | $EI\gamma^4 - m\omega^2 = 0$ | $EI\gamma^4 + T\gamma^2 - m\omega^2 = 0$ |
| spring no damping | $T\gamma^2 + k - m\omega^2 = 0$ | $EI\gamma^4 + k - m\omega^2 = 0$ | $EI\gamma^4 + T\gamma^2 + k - m\omega^2 = 0$ |
| no spring damping | $T\gamma^2 - ic\omega - m\omega^2 = 0$ | $EI\gamma^4 - ic\omega - m\omega^2 = 0$ | $EI\gamma^4 + T\gamma^2 - ic\omega - m\omega^2 = 0$ |
| spring damping | $T\gamma^2 + k - ic\omega - m\omega^2 = 0$ | $EI\gamma^4 + k - ic\omega - m\omega^2 = 0$ | $EI\gamma^4 + T\gamma^2 + k - ic\omega - m\omega^2 = 0$ |

Cases without soil springs and without damping are simple. The wave numbers for a

string, a beam, and a tensioned beam are $\gamma = \pm\sqrt{\dfrac{m}{T}}\omega$, $\gamma = \pm\left(\dfrac{m}{EI}\right)^{1/4}\sqrt{\omega}, \pm i\left(\dfrac{m}{EI}\right)^{1/4}\sqrt{\omega}$,

and $\gamma = \pm\sqrt{\dfrac{-T+\sqrt{T^2+4mEI\omega^2}}{2EI}}, \pm i\sqrt{\dfrac{T+\sqrt{T^2+4mEI\omega^2}}{2EI}}$ , respectively. For a string,

there are two waves traveling to the opposite directions. For a beam and a tensioned beam, there are two propagating waves and two evanescent waves. The root loci for these three cases are shown in Figures 3.1 to 3.3. In these figures and in the following figures

for the root loci, we use solid, dashed, dotted, and dashdot lines to indicate different roots of solutions.
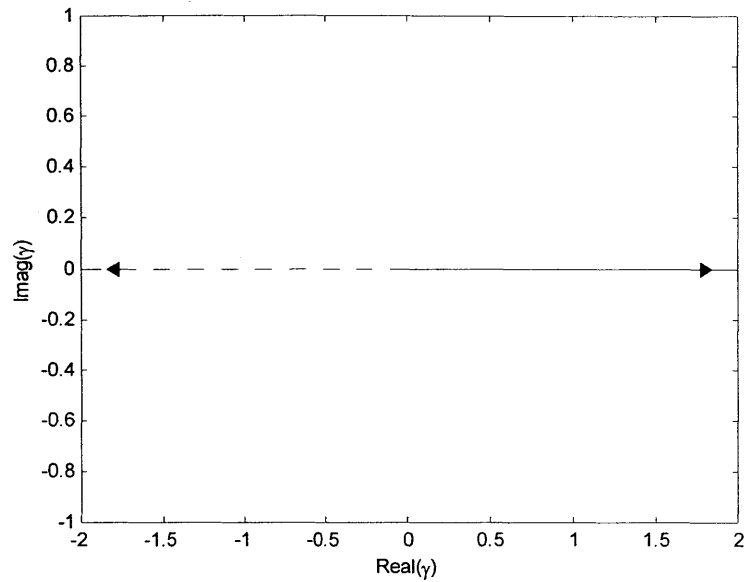


Figure 3.1. The root locus for a string in the complex $\gamma$-plane. Arrows point to the increasing wave frequency directions.
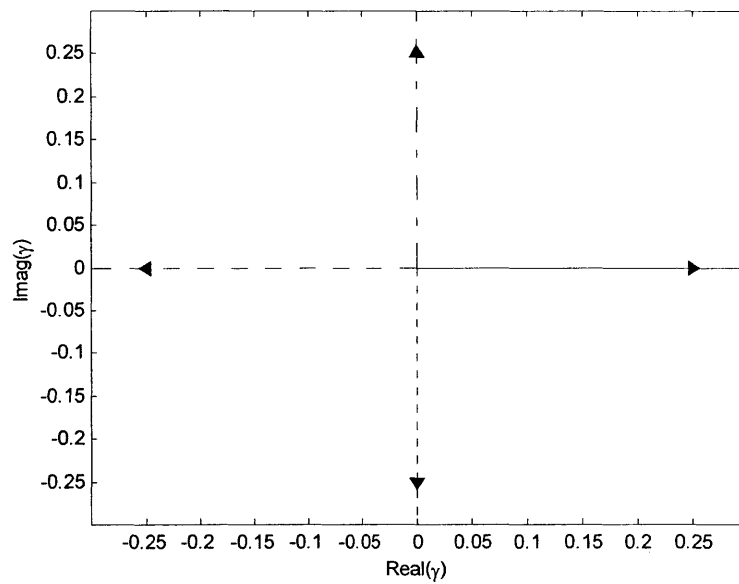


Figure 3.2. The root locus for a beam in the complex $\gamma$-plane. Arrows point to the increasing wave frequency directions.
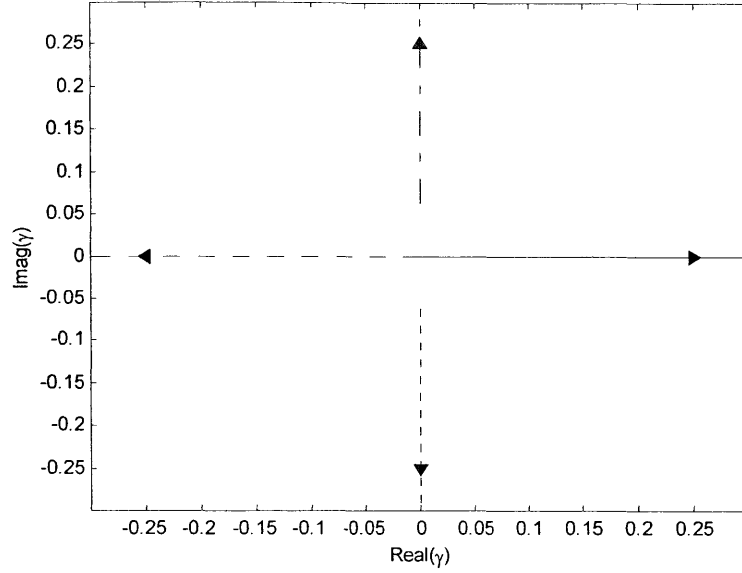
Figure 3.3. The root locus for a tensioned beam in the complex $\gamma$-plane. Arrows point to the increasing wave frequency directions.

For cases with an elastic foundation, there is a cutoff frequency $\omega_c = \sqrt{\dfrac{k}{m}}$. A cutoff frequency distinguishes the wave propagation behavior. For a string, the wave numbers are $\gamma = \pm\left(\dfrac{m\omega^2 - k}{T}\right)^{1/2}$. Thus, when the wave frequency follows the relationship $\omega > \omega_c$, both roots are real and two waves propagate to the opposite directions. When $\omega < \omega_c$, both roots are imaginary and there are two evanescent wave solutions for the problem. The root locus in the complex $\gamma$-plane is shown in Figure 3.4. It demonstrates that two roots turn to the real axis as wave frequency is larger than the cutoff frequency. For a beam, we can write the dispersion relation as $\gamma^4 = \dfrac{m\omega^2 - k}{EI}$. When $\omega > \omega_c$, the four roots are $\gamma = \pm\left(\dfrac{m\omega^2 - k}{EI}\right)^{1/4}, \pm i\left(\dfrac{m\omega^2 - k}{EI}\right)^{1/4}$, two propagating waves and two evanescent waves. When $\omega < \omega_c$, the four roots are $\gamma = \left(\dfrac{k - m\omega^2}{EI}\right)^{1/4}\left(\pm\left(\dfrac{\sqrt{2}}{2} \pm i\dfrac{\sqrt{2}}{2}\right)\right)$. Any of these

28

roots represents a wave propagating to one direction and decaying (or growing) in a

particular direction. For example, $Ae^{i(\gamma x - \omega t)}$ with $\gamma = \left( \dfrac{k - m\omega^2}{EI} \right)^{\frac{1}{4}} \left( \dfrac{\sqrt{2}}{2} + i \dfrac{\sqrt{2}}{2} \right)$

represents a wave traveling to the positive x direction and decaying in the same direction, as shown in Figure 3.5. When formulating the Green's function solution for a harmonic excitation, two of these solutions will add up to form an evanescent wave without propagating behavior. This evanescent wave is different from the evanescent wave for a string in that for the beam case the wave has an underdamped-like zero-crossing, though it is not an important issue for the system behavior. The root locus in the complex $\gamma$-plane is shown in Figure 3.6.
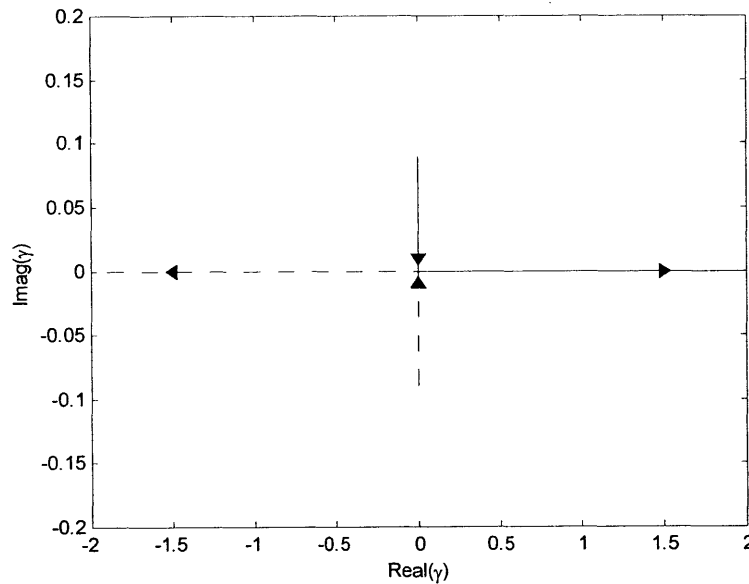
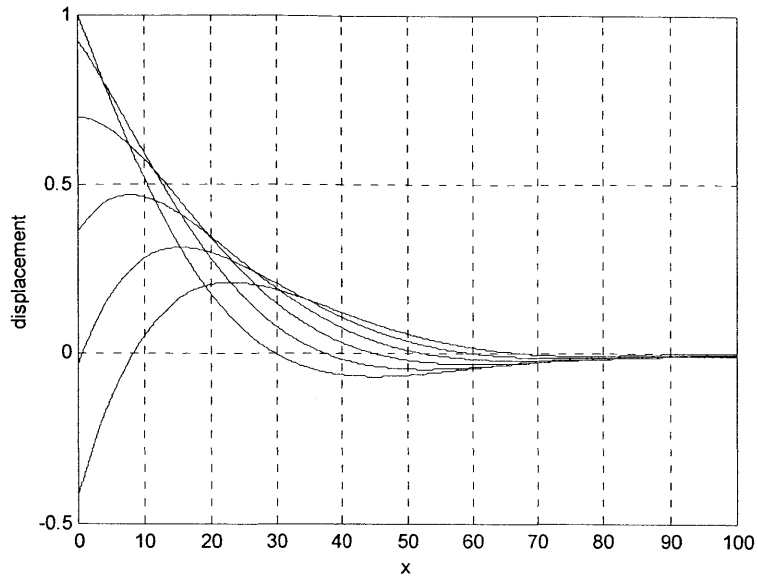Figure 3.4. The root locus for a string on an elastic foundation in the complex $\gamma$-plane.

29

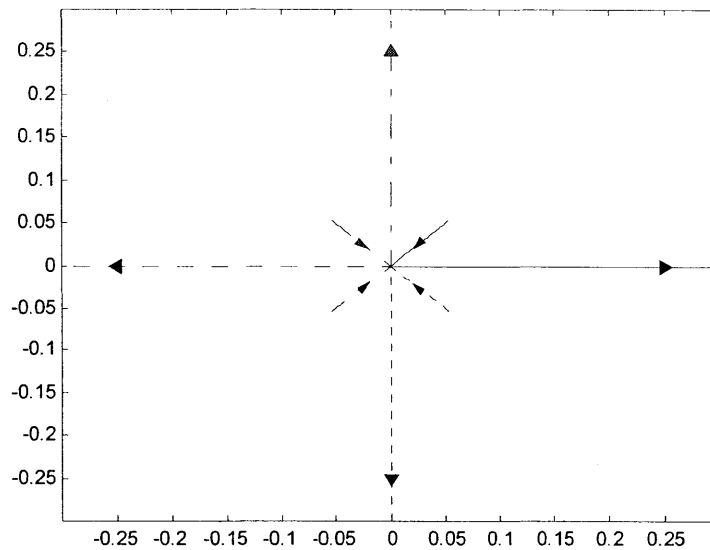Figure 3.5. The wave with decaying amplitude traveling to the right.



Figure 3.6. The root locus for a beam on an elastic foundation in the complex $\gamma$-plane.

The tensioned beam behaves mostly the same as a beam except there is another threshold for underdamped-like and overdamped-like evanescent waves. From the dispersion relation, we get $\gamma^2 = \dfrac{-T \pm \left(T^2 - 4EI(k - m\omega^2)\right)^{\frac{1}{2}}}{2EI}$ . When $\omega > \omega_c$, the four roots are

30

$$\gamma = \pm\sqrt{\frac{-T + \sqrt{T^2 - 4EI\left(k - m\omega^2\right)}}{2EI}}, \pm i\sqrt{\frac{T + \sqrt{T^2 - 4EI\left(k - m\omega^2\right)}}{2EI}} \text{ , two propagating waves}$$

and two evanescent waves. When $\omega < \omega_c$, the problem becomes more complicated.

When $T^2 > 4EIk$, the value $T^2 - 4EI\left(k - m\omega^2\right)$ of the inside square root is always

positive. The four roots are

$$\gamma = \pm i\sqrt{\frac{T - \sqrt{T^2 - 4EI\left(k - m\omega^2\right)}}{2EI}}, \pm i\sqrt{\frac{T + \sqrt{T^2 - 4EI\left(k - m\omega^2\right)}}{2EI}} \text{ , four overdamped-like}$$

evanescent waves. As $T^2 < 4EIk$, we get

$$\gamma^2 = \frac{-T \pm i\sqrt{4EI(k - m\omega^2) - T^2}}{2EI} = \sqrt{\frac{k - m\omega^2}{EI}} e^{\pm\theta} \text{ ,}$$

where $\theta = \tan^{-1}\dfrac{\sqrt{4EI(k - m\omega^2) - T^2}}{-T}$. Therefore, the wave numbers are

$$\gamma = \left(\frac{k - m\omega^2}{EI}\right)^{1/4} e^{\pm i\frac{\theta}{2}}, \left(\frac{k - m\omega^2}{EI}\right)^{1/4} e^{\pm i(\frac{\theta}{2} + \pi)} \text{ .}$$

These roots will form underdamped-like evanescent waves. The root loci are shown in

Figures 3.7 and 3.8, for $T^2 > 4EIk$ and $T^2 < 4EIk$ respectively. It is clear that there is one

cutoff frequency in Figure 3.7 above which two solutions become real, while in Figure

3.8 another threshold frequency is present for two types of evanescent waves.
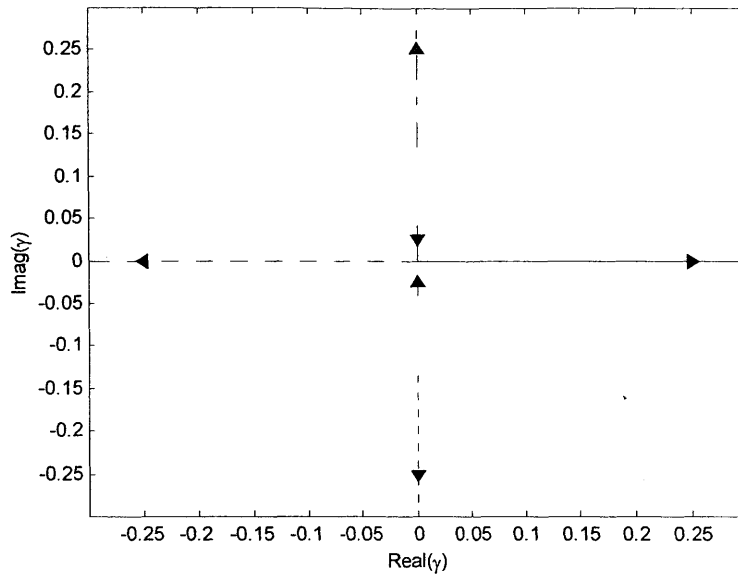
Figure 3.7. The root locus for a tensioned beam ($T^2 > 4EIk$) on an elastic foundation in the complex $\gamma$-plane.
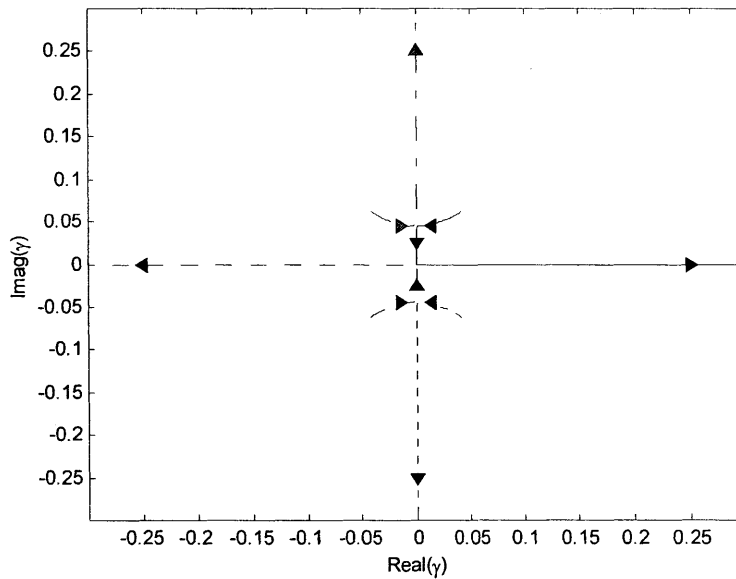


Figure 3.8. The root locus for a tensioned beam ($T^2 < 4EIk$) on an elastic foundation in the complex $\gamma$-plane.

All the above cases are energy conservative. When the energy dissipation comes into play, as the constant damping model used here, the root loci will be distorted in the complex plane. For a string with constant damping, the dispersion relation is

$T\gamma^2 - ic\omega - m\omega^2 = 0$ and the wave numbers are $\gamma = \pm\left(\dfrac{m\omega^2 + ic\omega}{T}\right)^{\frac{1}{2}}$. The root locus is

shown in Figure 3.9. As $c$ increases, the imaginary part of the wave number gets larger and this imaginary part determines the decaying effect in space. For high frequencies, the wave number approaches a constant for a constant $c$ and thus the decaying of the wave amplitude in space will be affected by the wave frequency. This is not the case for other systems such as a beam or a tensioned beam. Figures 3.10 and 3.11 show the curve distortion for a beam and a tensioned beam. Figures 3.12 to 3.15 show the root loci for three different kinds of systems with damping and spring terms. Notice that for a beam or a tensioned beam, four solutions are in four different quadrants. As can be seen from these figures, there is no clear cutoff frequency for each case. However, as the damping term is small, the behaviors become similar to the cases without damping (Figures 3.4, 3.6, 3.7, 3.8), and the cutoff frequency does give an idea of the tendency of the wave behavior.
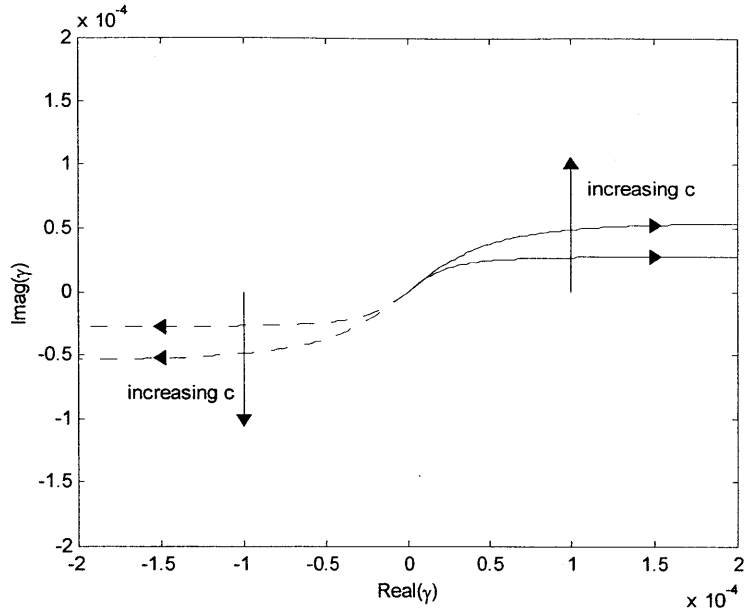
Figure 3.9. The root locus for a string with damping in the complex $\gamma$-plane. Two different values of damping are used for the two curves on each side, and larger damping constant makes absolute value of the imaginary part larger.
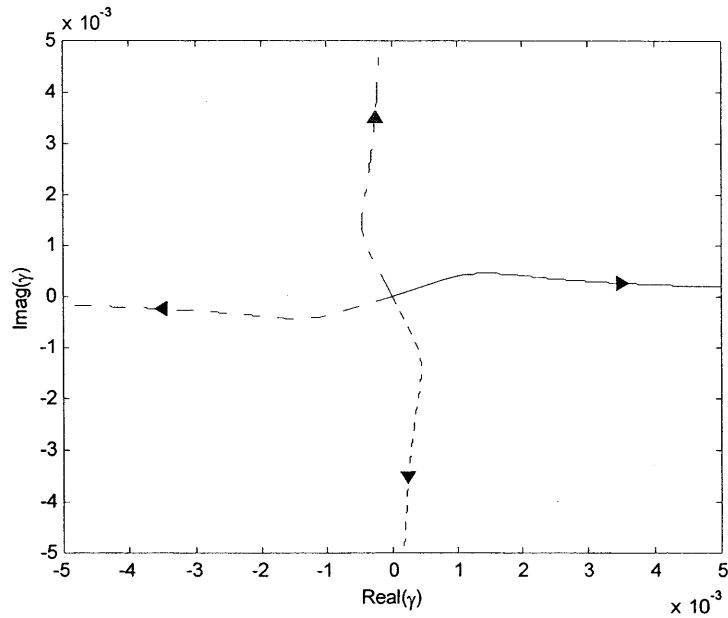


Figure 3.10. The root locus for a beam with damping in the complex $\gamma$-plane.

34
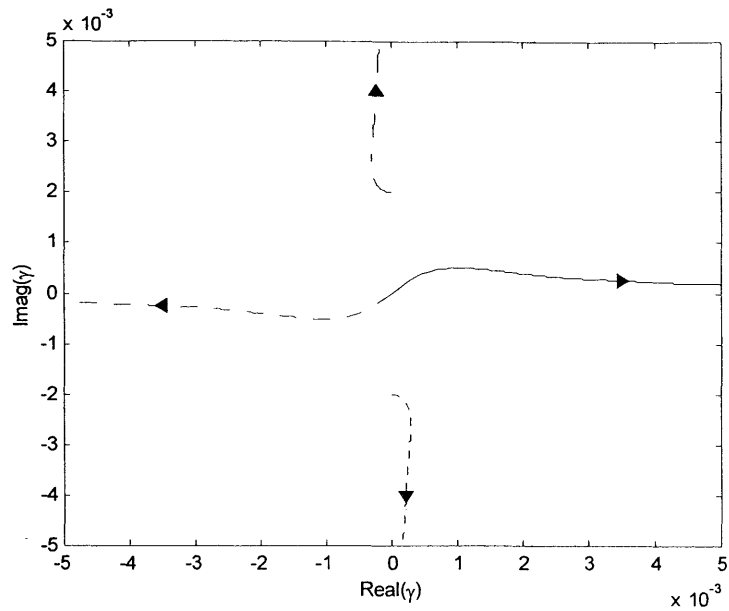
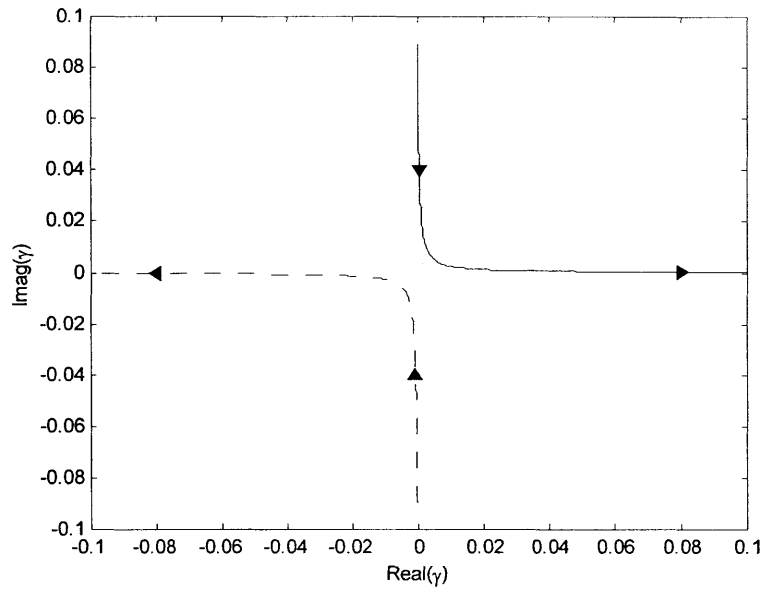Figure 3.11. The root locus for a tensioned beam with damping in the complex $\gamma$-plane.



Figure 3.12. The root locus for a damped string on an elastic foundation in the complex $\gamma$-plane.
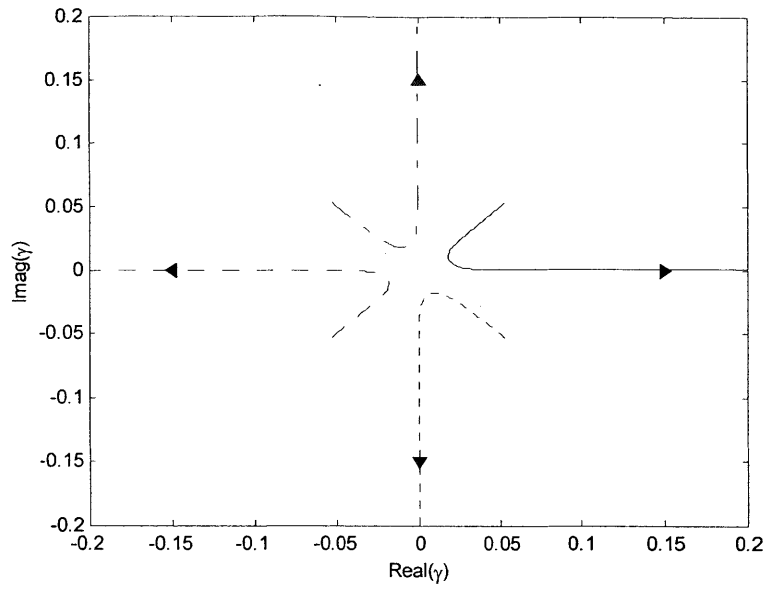
35

Figure 3.13. The root locus for a damped beam on an elastic foundation in the complex $\gamma$-plane.
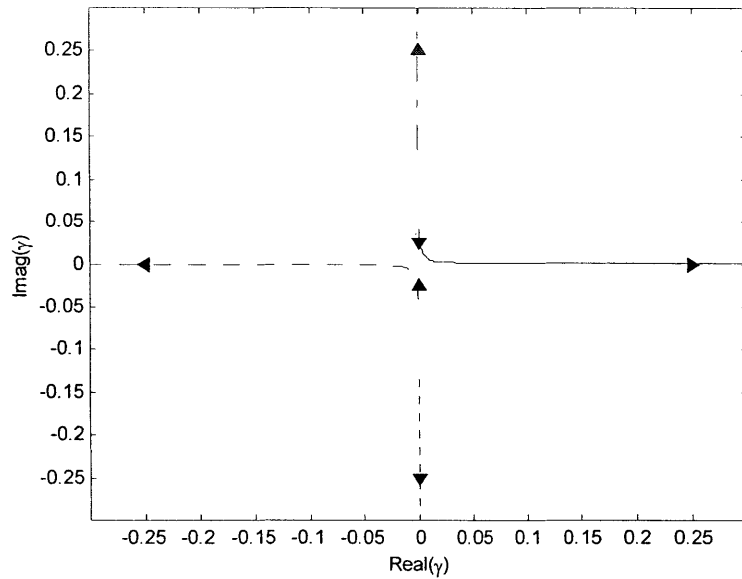


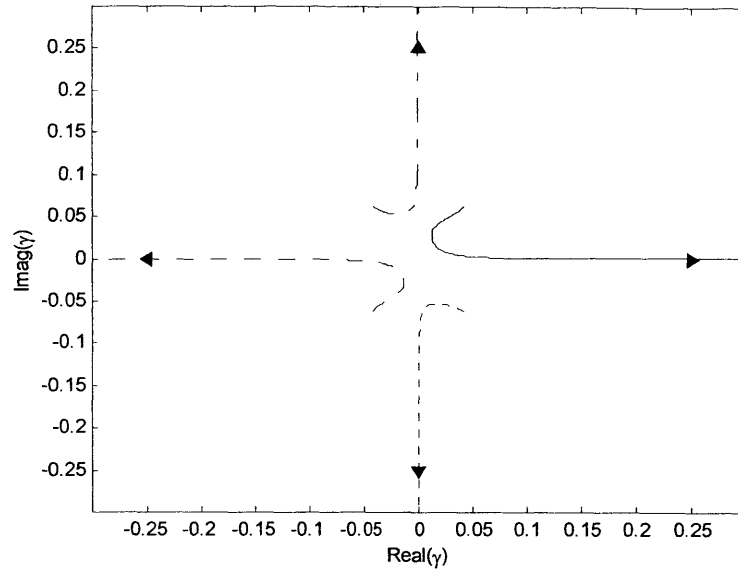Figure 3.14. The root locus for a damped tensioned beam ($T^2 > 4EIk$) on an elastic foundation in the complex $\gamma$-plane.

Figure 3.15. The root locus for a damped tensioned beam ($T^2 < 4EIk$) on an elastic foundation in the complex $\gamma$-plane.

## 3.3 Verification of the Dispersion Relation

A typical whack test result on the SCR model is shown in Figure 3.16. Pup 1 is close to the top end where the riser was hit, while pups 2, 3 and 4 are near the TDP and 4 may have been on the bottom. The data in pup 1 shows an impulse without much dispersion. This impulse travels along the riser. Due to the dispersive characteristics of the riser, the high frequency components of the impulse move faster than the lower frequency ones, as shown in the times series of pups 2, 3 and 4. The dispersion relation thus can be estimated from the data. Due to the resolution limitation, we use the traveling time between pups 1 and 2, between pups 1 and 3, and between pups 1 and 4. Assuming all the frequency components are in the impulse shown in pup 1, we are able to identify how long it takes for a wave with a certain frequency to move from pup 1 to pups 2, 3 and 4. Because we know the distance between every two pups, as demonstrated in Table 2.2, we are able to calculate the average velocity from the distance and the wave traveling time. Thus, the 'average wave number' can be estimated from the velocity and the wave frequency, and we obtain the dispersion relation curve (in SI unit) shown in Figure 3.17.

37
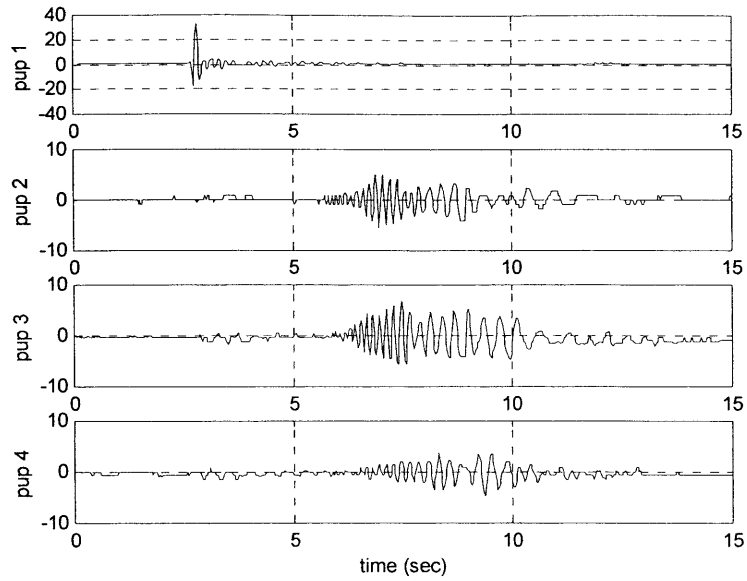
Figure 3.16. In-plane bending moment (ft-lbs) time series of a whack test for SCR with a hard bottom.
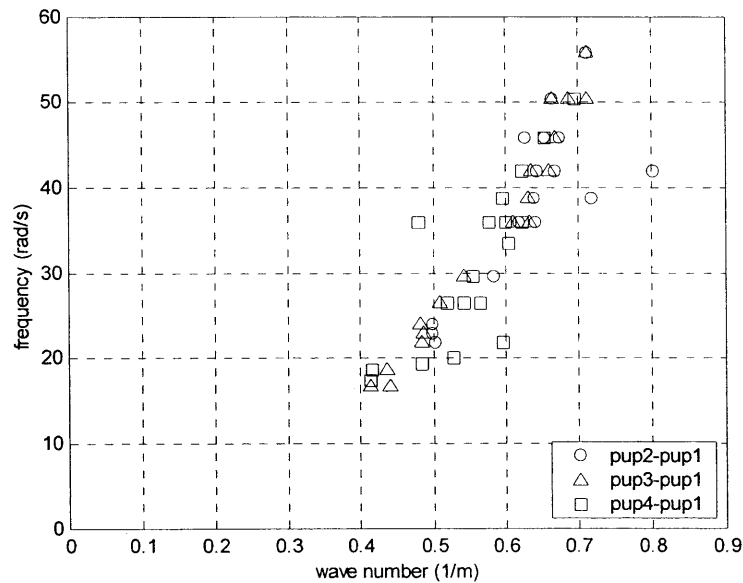


Figure 3.17. Dispersion relation (SI) for SCR from the whack test results.

The dispersion relation can also be obtained theoretically from the material properties of the riser. The riser can be modeled approximately as a straight tensioned beam with constant bending stiffness and slowly varying tension. The damping term can be

38

neglected due to its minor effect on the dispersion relation. Therefore, the governing equation can be written as:

$$EI\frac{\partial^4 y}{\partial x^4} - \frac{\partial}{\partial x}\left(T(x)\frac{\partial y}{\partial x}\right) + m\frac{\partial^2 y}{\partial t^2} = 0,$$  (3.6)

and the dispersion relation is

$$EI\gamma(x)^4 + T(x)\gamma(x)^2 - m\omega^2 = 0,$$  (3.7)

where the derivative term of tension is dropped because it is small for slowing varying tension. This is a local dispersion relation. For the propagating wave to the positive x direction, the local wave number is written as

$$\gamma(x) = \sqrt{\frac{-T(x) + \sqrt{T(x)^2 + 4mEI\omega^2}}{2EI}}.$$  (3.8)

That is, the wavelength and the wave velocity change along the riser. The experimental dispersion relation shown in Figure 3.17 is actually an average result from a long distance of wave traveling. To make the theoretical result comparable with the experimental relation, we have to estimate the 'average wave number' for a certain distance.

The practical method for calculating this wave number is first to write down the time for a wave with frequency $\omega$ to travel a distance $L$. The local wave velocity is

$$v(x) = \frac{dx}{dt},$$  (3.9)

or

$$dt = \frac{dx}{v(x)}.$$  (3.10)

Over a finite distance, we integrate Equation 3.10 and get

$$\int_0^\tau dt = \int_0^L \frac{dx}{v(x)},$$  (3.11)

where $L$ is the distance traveled and $\tau$ is the time spent to travel the distance $L$. The wave velocity can be represented by the wave frequency and the wave number:

$$v(x) = \frac{\omega}{\gamma(x)},$$  (3.12)

so we are able to write the time as

$$\tau = \frac{1}{\omega} \int_0^L \gamma(x)dx$$

$$= \frac{1}{\omega} \int_0^L \sqrt{\frac{-T(x) + \sqrt{T(x)^2 + 4mEI\omega^2}}{2EI}} dx. \qquad (3.13)$$

The average velocity calculated in the experimental dispersion relation is defined as $\bar{v} = L/\tau$. The corresponding 'average wave number' as in Figure 3.17 is then estimated based on the average velocity and the wave frequency

$$\bar{\gamma} = \frac{\omega}{\bar{v}} = \frac{\omega}{L/\tau} = \frac{\omega\tau}{L} = \frac{\int_0^L \sqrt{\frac{-T(x) + \sqrt{T(x)^2 + 4mEI\omega^2}}{2EI}} dx}{L}. \qquad (3.14)$$

That is, the 'average wave number' is a spatial average over the region that the wave travels.

The risers for all configurations in this test are made of 1.25'' ID X 0.125'' wall 6061-T6511 extruded aluminum tube. The material specifications in SI are as follows:

Young's modulus: 7E10 Pa

Outer diameter: 0.0381 m

Inner diameter: 0.0318 m

Moment of Inertia: 5.37E-8 m^4

Mass per unit length: 2.63 kg/m

The added mass per unit length is estimated as

$$m_a = C_m \rho_f \pi \frac{OD^2}{4}, \qquad (3.15)$$

where $C_m$ is the added mass coefficient, $\rho_f$ is the fluid density, and $OD$ is the outer diameter. Here we assume negligible added mass for the whack test, i.e., $C_m$ is set to zero, and the total mass per unit length is still 2.63 kg/m. If in the general case when $C_m = 1$, the added mass per unit length is 1.14 kg/m, and the total mass per unit length is 3.77 kg/m. This total mass will be used in the discussion in Chapter 4. A tension prediction from a commercial finite element program is available and shown in Figure 3.18. Using numerical integration with all these estimated properties, we are able to predict the 'average wave number'. The comparison between the predicted and the

40

experimental dispersion relations is shown in Figure 3.19. Though the high frequency components of the experimental results tend to have lower wave numbers than the predicted ones, they agree reasonably well and may only need some fine-tuning for the numbers of material properties. One likely source of the difference is that the actual added mass was not known.
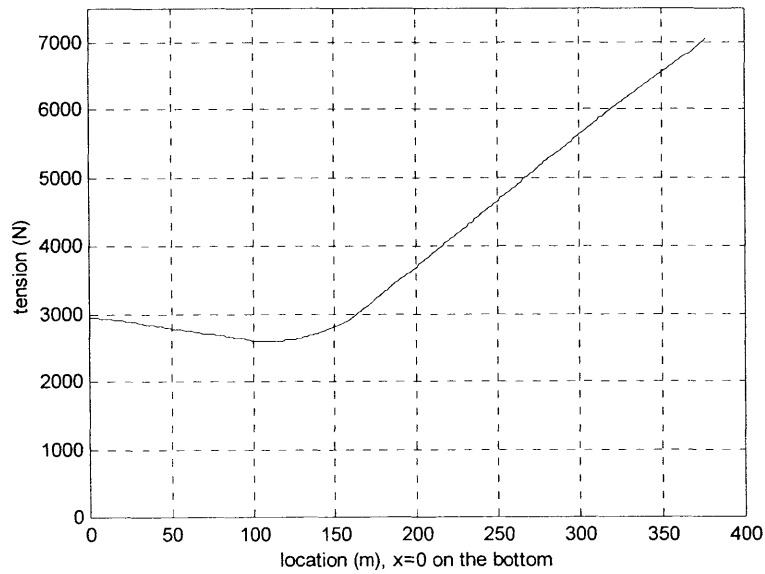


Figure 3.18. Prediction of tension variation by an industrial finite element program.
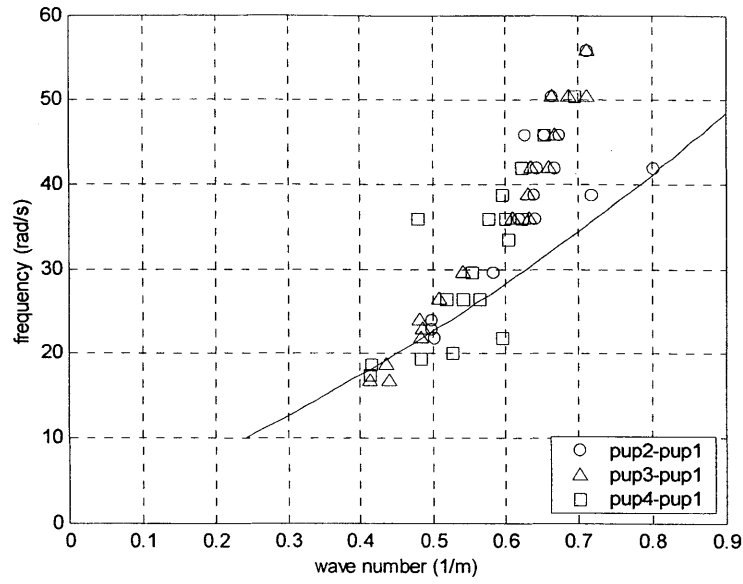
Figure 3.19. Comparison of the theoretical and the experimental dispersion relations. The solid line represents the theoretical prediction while circles, triangles, and squares represent the experimental results.

# Chapter 4 Wave Propagation on Material with Varying Properties

## 4.1 Discontinuity and Cutoff Frequency

An oil riser is built up by assembling several sections to form a long slender structure. It may have discontinuities across adjacent sections, for example, between the buoyant pipe and the bare pipe. Also, another type of discontinuity comes from the touch-down point (TDP). When the bottom part of a riser lies on the underwater soil, it is possibly modeled as an elastic foundation to account for the soil-structure interaction. Thus, the TDP becomes a discontinuity connecting two parts with and without an elastic spring term. These types of discontinuities are discussed as follows.

At the point of discontinuity, the kinematic and dynamic conditions must be continuous. For a string, the displacement and the force have to be the same for both sides at the interface. For a beam or a tensioned beam, two additional terms, the slope and the bending moment, must be continuous. Thus, the sums of these quantities for the incident wave and the reflective wave have to equal the quantities for the transmitted wave.

A simple case demonstrates the calculations for the discontinuity problem. Figure 4.1 shows a string with different material properties on both sides of $x = x_0$. From the previous section, we know the wave numbers are $\gamma_1 = \pm \left( \dfrac{m_1 \omega^2 - k_1}{T_1} \right)^{1/2}$ and

$\gamma_2 = \pm \left( \dfrac{m_2 \omega^2 - k_2}{T_2} \right)^{1/2}$. Let us make $\gamma_{1a}$ and $\gamma_{2a}$ as the positive ones, and $\gamma_{1b}$ and $\gamma_{2b}$ as the negative ones. Assuming the incident wave comes from the left where $x < x_0$, we have

Incident wave:

displacement $y_i = A_i e^{i(\gamma_{1a}x - \omega t)}$

force $f_i = T_1 \dfrac{\partial y_i}{\partial x} = i\gamma_{1a}T_1 A_i e^{i(\gamma_{1a}x - \omega t)}$


Reflective wave:

displacement $y_r = A_r e^{i(\gamma_{1b}x - \omega t)}$

force $f_r = T_1 \dfrac{\partial y_r}{\partial x} = i\gamma_{1b}T_1 A_r e^{i(\gamma_{1b}x - \omega t)}$


Transmitted wave:

displacement $y_t = A_t e^{i(\gamma_{2a}x - \omega t)}$

force $f_t = T_2 \dfrac{\partial y_t}{\partial x} = i\gamma_{2a}T_2 A_t e^{i(\gamma_{2a}x - \omega t)}$.


These equations are valid whether the frequency is above or below cutoff. To match the displacement and the force at $x = x_0$, we obtain

$$A_i e^{i\gamma_{1a}x_0} + A_r e^{i\gamma_{1b}x_0} = A_t e^{i\gamma_{2a}x_0} \tag{4.1}$$

$$i\gamma_{1a}T_1 A_i e^{i\gamma_{1a}x_0} + i\gamma_{1b}T_1 A_r e^{i\gamma_{1b}x_0} = i\gamma_{2a}T_2 A_t e^{i\gamma_{2a}x_0}. \tag{4.2}$$

Assuming $A_i$ is known, we can solve $A_r$ and $A_t$ by these two equations, or we can write it in a matrix form:

$$\begin{bmatrix} e^{i\gamma_{1b}x_0} & -e^{i\gamma_{2a}x_0} \\ i\gamma_{1b}T_1 e^{i\gamma_{1b}x_0} & -i\gamma_{2a}T_2 e^{i\gamma_{2a}x_0} \end{bmatrix} \begin{bmatrix} A_r \\ A_t \end{bmatrix} = \begin{bmatrix} -e^{i\gamma_{1a}x_0} \\ -i\gamma_{1a}T_1 e^{i\gamma_{1a}x_0} \end{bmatrix} A_i. \tag{4.3}$$

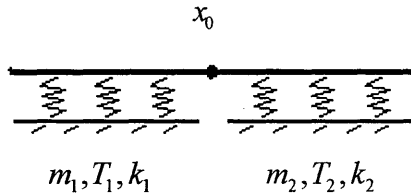Thus, we can add up the different components of waves and obtain the solution.



Figure 4.1. A string with different material properties on both sides of $x = x_0$.

Although the equations are applicable to cases above or below cutoff frequency, the wave behavior is quite different for both cases. The cutoff frequency for the left part is

$\omega_{c1} = \sqrt{\dfrac{k_1}{m_1}}$ , and the cutoff frequency for the right part is $\omega_{c2} = \sqrt{\dfrac{k_2}{m_2}}$ . Assume $k_2 > k_1$,

and an incident wave from the left has the frequency $\omega > \omega_{c1}$. When an incident wave comes to the interface point $x_0$, the cutoff frequency in the right part is critical to determine the wave behavior. If $\omega > \omega_{c2}$, the transmitted wave propagates and a certain amount of energy moves toward the right. If $\omega < \omega_{c2}$, the right side can only have evanescent waves, and the energy is reflected to the left part. Figure 4.2 shows a snapshot of a wave above the cutoff frequency and Figure 4.3 shows a snapshot when below cutoff. Notice that the wavelength is longer on the right side in Figure 4.2. This is

because $\gamma = \left( \dfrac{m\omega^2 - k}{T} \right)^{1\!/\!2}$ and $k_2 > k_1$, so that the right side has a smaller wave number

and thus has longer wavelength.
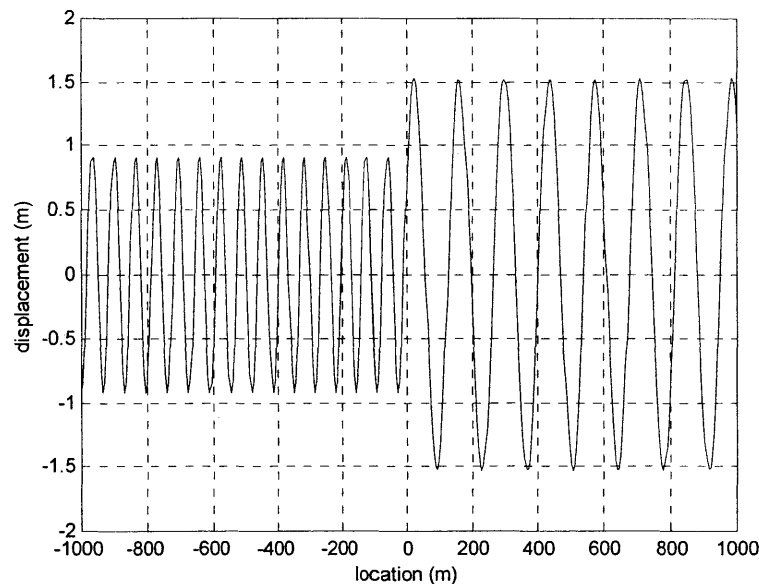


Figure 4.2. A snapshot of a wave with frequency above the cutoff frequency on the right side. Discontinuity is at $x$=0.

45
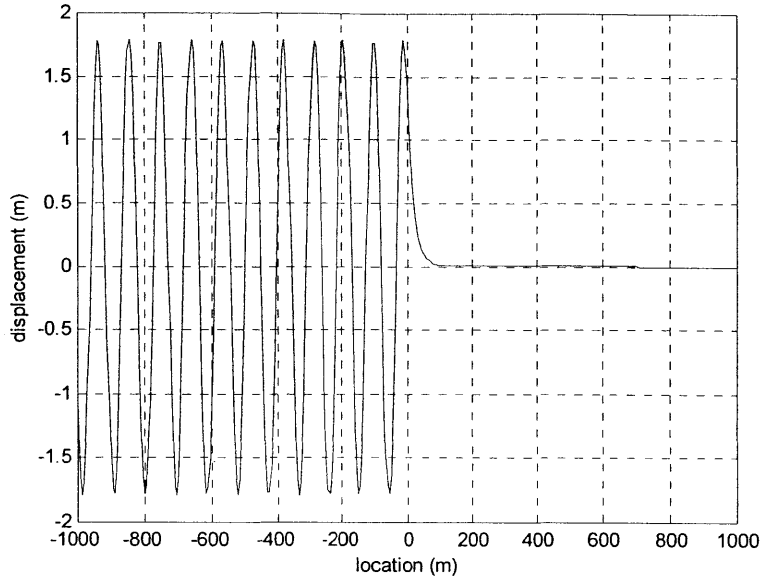
Figure 4.3. A snapshot of a wave with frequency below the cutoff frequency on the right side. Discontinuity is at $x=0$.



$x_0$

$E_1, I_1, T_1, m_1, c_1, k_1 \qquad E_2, I_2, T_2, m_2, c_2, k_2$
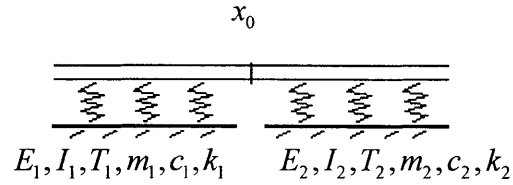
Figure 4.4. A tensioned beam with different material properties on both sides of $x = x_0$.

The discontinuity problem for a tensioned beam (Figure 4.4) on an elastic foundation with damping is more involved. The wave numbers are

$$\gamma = \pm \left( \frac{-T \pm \left( T^2 - 4EI \left( -m\omega^2 - ic\omega + k \right) \right)^{1/2}}{2EI} \right)^{1/2}$$

. As shown in the previous section, these

four wave numbers are in four different quadrants. They represent four types of waves: 1. decaying to the right and traveling to the right; 4. decaying to the right and traveling to the left; 3. decaying to the left and traveling to the right; 3. decaying to the left and traveling to the left (here traveling direction means the moving direction of the phase velocity). These are shown schematically in Figure 4.5. We assign the wave numbers

$\gamma_{1a}, \gamma_{1b}, \gamma_{1c}, \gamma_{1d}$ for the left part respectively, and $\gamma_{2a}, \gamma_{2b}, \gamma_{2c}, \gamma_{2d}$ for the right part, respectively.
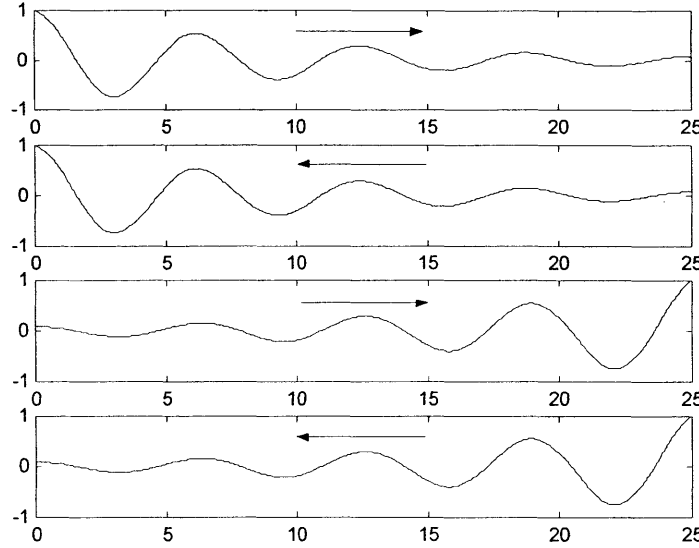


Figure 4.5. Four types of waves for a beam or a tensioned beam.

Assuming the incident wave comes from the left, we can write its two possible components of the displacement as $y_{ia} = A_{ia} e^{i(\gamma_{1a} x - \omega t)}$ and $y_{ib} = A_{ib} e^{i(\gamma_{1b} x - \omega t)}$. The two wave numbers are selected due to the energy radiation condition. These components have smaller amplitudes at the right and thus satisfy the energy decaying behavior in the propagating direction. Also, we have to determine the displacements for the reflective wave: $y_{rc} = A_{rc} e^{i(\gamma_{1c} x - \omega t)}$ and $y_{rd} = A_{rd} e^{i(\gamma_{1d} x - \omega t)}$, as well as the displacements for the transmitted wave: $y_{ta} = A_{ta} e^{i(\gamma_{2a} x - \omega t)}$ and $y_{tb} = A_{tb} e^{i(\gamma_{2b} x - \omega t)}$. The amplitudes of the wave components have to satisfy the kinematic and dynamic conditions, i.e., the continuities of displacement $y$, slope $\dfrac{\partial y}{\partial x}$, moment $EI \dfrac{\partial^2 y}{\partial x^2}$, and force $-EI \dfrac{\partial^3 y}{\partial x^3} + T \dfrac{\partial y}{\partial x}$ (for a constant $EI$ for both left and right portions). After some arrangements, the equation can be written as a matrix form:

47

$$
\begin{bmatrix}
e^{i\gamma_{1c}x_0} & e^{i\gamma_{1d}x_0} & -e^{i\gamma_{2a}x_0} & -e^{i\gamma_{2b}x_0} \\
i\gamma_{1c}e^{i\gamma_{1c}x_0} & i\gamma_{1d}e^{i\gamma_{1d}x_0} & -i\gamma_{2a}e^{i\gamma_{2a}x_0} & -i\gamma_{2b}e^{i\gamma_{2b}x_0} \\
-E_1 I_1 \gamma_{1c}^2 e^{i\gamma_{1c}x_0} & -E_1 I_1 \gamma_{1d}^2 e^{i\gamma_{1d}x_0} & E_2 I_2 \gamma_{2a}^2 e^{i\gamma_{2a}x_0} & E_2 I_2 \gamma_{2b}^2 e^{i\gamma_{2b}x_0} \\
i\left(E_1 I_1 \gamma_{1c}^3 + T_1\gamma_{1c}\right)e^{i\gamma_{1c}x_0} & i\left(E_1 I_1 \gamma_{1d}^3 + T_1\gamma_{1d}\right)e^{i\gamma_{1d}x_0} & -i\left(E_2 I_2 \gamma_{2a}^3 + T_2\gamma_{2a}\right)e^{i\gamma_{2a}x_0} & -i\left(E_2 I_2 \gamma_{2b}^3 + T_2\gamma_{2b}\right)e^{i\gamma_{2b}x_0}
\end{bmatrix}
\begin{bmatrix} A_{rc} \\ A_{rd} \\ A_{ta} \\ A_{tb} \end{bmatrix}
\quad (4.4)
$$

$$
=
\begin{bmatrix}
-e^{i\gamma_{1a}x_0} & -e^{i\gamma_{1b}x_0} \\
-i\gamma_{1a}e^{i\gamma_{1a}x_0} & -i\gamma_{1b}e^{i\gamma_{1b}x_0} \\
-E_1 I_1 \gamma_{1a}^2 e^{i\gamma_{1a}x_0} & -E_1 I_1 \gamma_{1b}^2 e^{i\gamma_{1b}x_0} \\
-i\left(E_1 I_1 \gamma_{1a}^3 + T_1\gamma_{1a}\right)e^{i\gamma_{1a}x_0} & -i\left(E_1 I_1 \gamma_{1b}^3 + T_1\gamma_{1b}\right)e^{i\gamma_{1b}x_0}
\end{bmatrix}
\begin{bmatrix} A_{ia} \\ A_{ib} \end{bmatrix}.
$$

The amplitudes of different wave components can be determined from this matrix equation. We use a tensioned beam with mass per unit length 1347 kg/m and stiffness per unit length 86000 $N/m^2$ as an example. The simulated results are shown as two snapshots in Figures 4.6 and 4.7. This system has a cutoff frequency 1.27 Hz. With incident wave frequency 1.5 Hz for Figure 4.6 and 1 Hz for Figure 4.7, the behaviors tend to be similar as those for the cases above or below the cutoff frequency, though there is no generally defined cutoff frequency for a damped system.
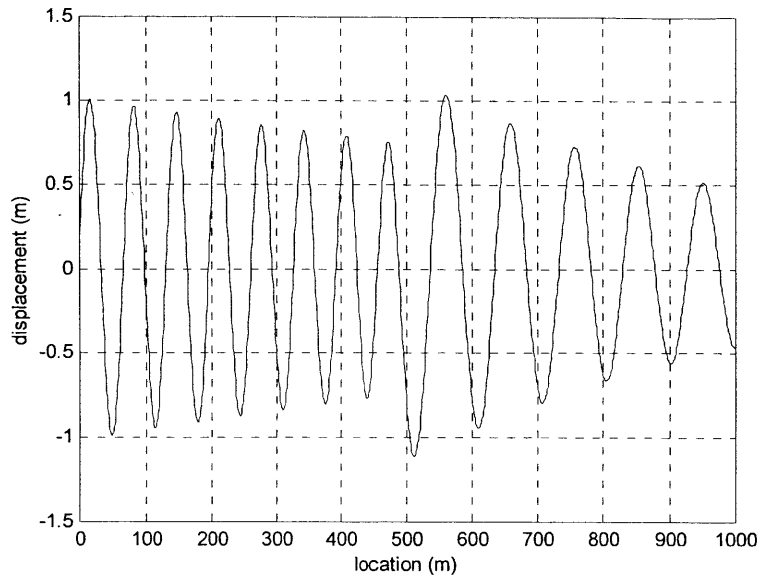
Figure 4.6. A snapshot of a wave with frequency above the undamped cutoff frequency on the right side for a damped riser. Discontinuity is at $x$=500.
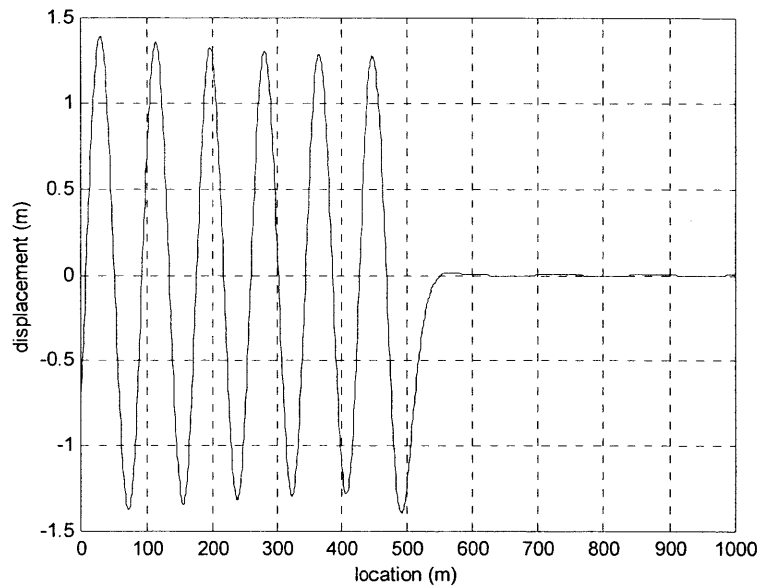


Figure 4.7. A snapshot of a wave with frequency below the undamped cutoff frequency on the right side for a damped riser. Discontinuity is at $x$=500.

**4.2 Spatial Variation of Properties: the WKB Method**

49

In addition to the discontinuities at certain locations along a riser, it may also have spatially varying properties. For example, the tension along the riser varies due to different water depths. Here we assume the slowly varying properties, and the WKB method is suitable for solving this type of problem.

The governing equation for a damped tensioned beam on an elastic foundation with slowing varying properties is written as:

$$\frac{\partial^2}{\partial x^2}\left(EI(x)\frac{\partial^2 y}{\partial x^2}\right) - \frac{\partial}{\partial x}\left(T(x)\frac{\partial y}{\partial x}\right) + m(x)\frac{\partial^2 y}{\partial t^2} + c(x)\frac{\partial y}{\partial t} + k(x)y = 0, \qquad (4.5)$$

Assuming a harmonic solution with the form

$$y = \bar{y}(x)e^{-i\omega t},$$

it becomes

$$EI\frac{d^4\bar{y}}{dx^4} + 2\frac{d(EI)}{dx}\frac{d^3\bar{y}}{dx^3} + \frac{d^2(EI)}{dx^2}\frac{d^2\bar{y}}{dx^2} - T\frac{d^2\bar{y}}{dx^2} - \frac{dT}{dx}\frac{d\bar{y}}{dx} - m\omega^2\bar{y} - ic\omega\bar{y} + k\bar{y} = 0. \quad (4.6)$$

To take care of the spatial variation in this problem, we use the WKB method and let

$$\bar{y}(x) = e^{i\theta(x)}\{a_0(x) + a_1(x) + a_2(x) + ...\}, \qquad (4.7)$$

where $a_1$ and $a_2$ are higher order corrections. We also assign

$$\frac{d\theta(x)}{dx} \equiv \gamma(x), \qquad (4.8)$$

which is the local wave number along the system. The derivatives of $\bar{y}(x)$ are

$$\frac{d\bar{y}}{dx} = i\gamma e^{i\theta}\left\{a_0 + a_1 + a_2 + ...\right\} + e^{i\theta}\left\{a_0' + a_1' + a_2' + ...\right\},$$

$$\frac{d^2\bar{y}}{dx^2} = (i\gamma' - \gamma^2)e^{i\theta}\left\{a_0 + a_1 + a_2 + ...\right\} + 2i\gamma e^{i\theta}\left\{a_0' + a_1' + a_2' + ...\right\} + e^{i\theta}\left\{a_0'' + a_1'' + a_2'' + ...\right\},$$

$$\frac{d^3\bar{y}}{dx^3} = (i\gamma'' - 3\gamma'\gamma - i\gamma^3)e^{i\theta}\left\{a_0 + a_1 + a_2 + ...\right\} + (3i\gamma' - 3\gamma^2)e^{i\theta}\left\{a_0' + a_1' + a_2' + ...\right\} +$$

$$+ 3i\gamma e^{i\theta}\left\{a_0'' + a_1'' + a_2'' + ...\right\} + e^{i\theta}\left\{a_0''' + a_1''' + a_2''' + ...\right\},$$

$$\frac{d^4\bar{y}}{dx^4} = (i\gamma''' - 4\gamma''\gamma - 3\gamma'^2 - 6i\gamma'\gamma^2 + \gamma^4)e^{i\theta}\left\{a_0 + a_1 + a_2 + ...\right\} +$$

$$+ (4i\gamma'' - 12\gamma\gamma' - 4i\gamma^3)e^{i\theta}\left\{a_0' + a_1' + a_2' + ...\right\} + (6i\gamma' - 6\gamma^2)e^{i\theta}\left\{a_0'' + a_1'' + a_2'' + ...\right\} +$$

$$+ 4i\gamma e^{i\theta}\left\{a_0''' + a_1''' + a_2''' + ...\right\} + e^{i\theta}\left\{a_0^{(4)} + a_1^{(4)} + a_2^{(4)} + ...\right\}.$$

Inserting the corresponding terms into Equation 4.6, we obtain the equation for the leading order:

$$EI(x)\gamma^4(x) + T(x)\gamma^2(x) - m(x)\omega^2 - ic(x)\omega + k(x) = 0. \tag{4.9}$$

This is the same as the dispersion equation for a damped tensioned beam on an elastic foundation. Therefore, the local wave number has to satisfy the local dispersion relations. The next order terms give

$$EI(-6i\gamma'\gamma^2 a_0 + \gamma^4 a_1 - 4i\gamma^3 a_0') + 2(EI)'(-i\gamma^3 a_0) - T(i\gamma'a_0 - \gamma^2 a_1 + 2i\gamma a_0') -$$

$$- T'(i\gamma a_0) - m\omega^2 a_1 - ic\omega a_1 + k a_1 = 0.$$

All the terms with $a_1$ can be eliminated due to the dispersion relation Equation 4.9. After rearrangement, we get

$$a_0[6EI\gamma'\gamma^2 + 2(EI)'\gamma^3 + T\gamma' + T'\gamma] + 2a_0'[2EI\gamma^3 + T\gamma] = 0,$$

or

$$\frac{d}{dx}\left\{a_0^2(x)[2EI(x)\gamma^3(x) + T(x)\gamma(x)]\right\} = 0. \tag{4.10}$$

Equation 4.10 gives the amplitude variation along $x$. To this order, we can write the harmonic solution as

$$y(x,t) \sim a_0(x)e^{i[\theta(x) - \omega t]}, \tag{4.11}$$

where

$$\theta(x) = \int_x \gamma(x)dx.$$

Notice that due to the complex wave number obtained from Equation 4.9, $\theta(x)$ and the amplitude $a_0$ are also complex. The complex $\theta(x)$ contributes to the decay of the amplitude from damping, and the complex $a_0$ gives phase shift in the response. Equation 4.10 is actually closely related to the power balance along $x$, except the attenuation due to damping. For an undamped system, we will have an average power

$$\langle P \rangle = a_0^2 (EI\gamma^3\omega + \frac{1}{2}T\gamma\omega). \tag{4.12}$$

The power equality (known as Green's law) states

$$\langle P \rangle |_{x=x_1} = \langle P \rangle |_{x=x_2}$$

and thus

$$a_0^2(x)[EI(x)\gamma^3(x)\omega + \frac{1}{2}T(x)\gamma(x)\omega] = \text{constant},$$

the same as Equation 4.10. Figure (4.8) shows snapshots for an example case with varying properties.
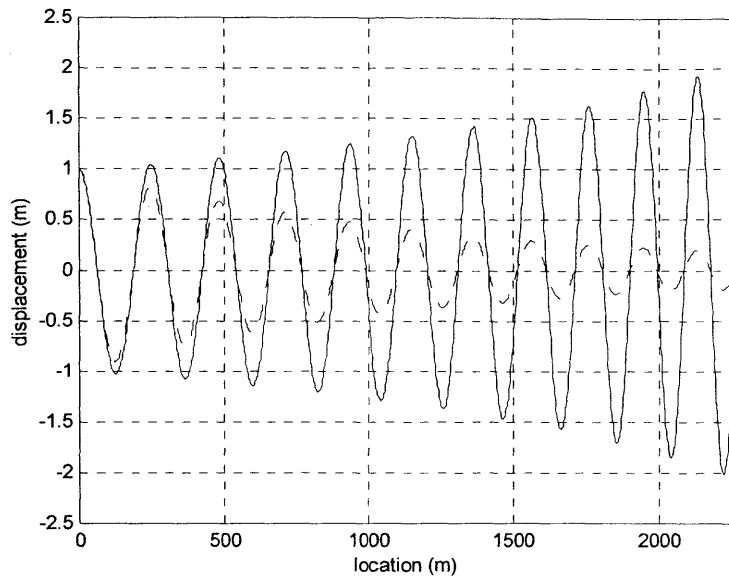
Figure 4.8. Snapshots for a tensioned beam with linearly decreasing tension on an elastic foundation (solid line: no damping; dashed line: 2% damping). On the right side, the wavelength is shorter and the amplitude is larger for the solid line due to the smaller tension there.

## 4.3 Varying Foundation Stiffness: Turning Point Problem

Although the WKB method is powerful for solving spatially varying problems, it fails around a turning point. For a spatially varying foundation stiffness problem (the cutoff frequency also varies in space with the stiffness constant), the turning point refers to the location where the wave frequency is equal to the cutoff frequency. At this location, the wavelength becomes singular, and the wave changes from above cutoff frequency on one side to below cutoff frequency on the other side. In this section, we will solve the problems with linearly varying spring constants. Extending the solution from the linearly varying stiffness case with patched solutions in different regions can solve problems for more complicated variations of the spring constant.

The governing equation of a string with a linearly varying spring constant can be written as:

$$-T\frac{\partial^2 y}{\partial x^2} + m\frac{\partial^2 y}{\partial t^2} + k(x)y = 0,$$

where we assume constant tension and constant mass. Inserting a harmonic solution $y = Y(x)e^{-i\omega t}$ to this equation, we get

$$-T\frac{d^2 Y}{dx^2} - m\omega^2 Y + k(x)Y = 0. \qquad (4.13)$$

Assume the linearly varying $k(x)$ has the spring constant as shown in Figure 4.9, and also it satisfies $k(0) = m\omega^2$. This choice of $k(0)$ is just for the convenience of calculation and does not influence the generality because we can shift the solution to a proper $x$ location later on. With this setup, we can write the spring constant as:

$$k(x) = ax + m\omega^2, \qquad (4.14)$$

where $a$ is the slope of the linear variation. Inserting Equation 4.14 into Equation 4.13, we get

$$-T\frac{d^2 Y}{dx^2} + axY = 0,$$

or

$$\frac{d^2 Y}{dx^2} - \frac{a}{T}xY = 0. \qquad (4.15)$$

Equation 4.15 is an Airy equation and we can simplify it by introducing

$$\bar{x} = \left(\frac{a}{T}\right)^{1/3} x,$$

and therefore

$$\frac{d}{dx} = \left(\frac{a}{T}\right)^{1/3} \frac{d}{d\bar{x}}.$$

Substituting these two terms for the terms in Equation 4.15, it becomes

$$\frac{d^2 Y}{d\bar{x}^2} - \bar{x}Y = 0. \qquad (4.16)$$

Solutions for Equation 4.16 can be written as

$$Y(x) = D_A Ai(\bar{x}) + D_B Bi(\bar{x}),$$

where $Ai$ and $Bi$ are Airy functions. For an infinitely long string, because $Bi$ is divergent for positive $x$ and thus it is not physically meaningful, the second term is eliminated. The solution will be

$$y(x,t) = D_A Ai\left(\left(\frac{a}{T}\right)^{\frac{1}{3}} x\right) e^{-i\omega t}. \qquad (4.17)$$

A typical Airy function $Ai$ is shown in Figure 4.10. The decay on the right side is expected because the wave frequency is smaller than the cutoff frequencies there. On the left side, the wavelength gets longer and the amplitude gets larger as $x$ gets close to 0. These behaviors can be explained by the power balance as in Equation 4.12.
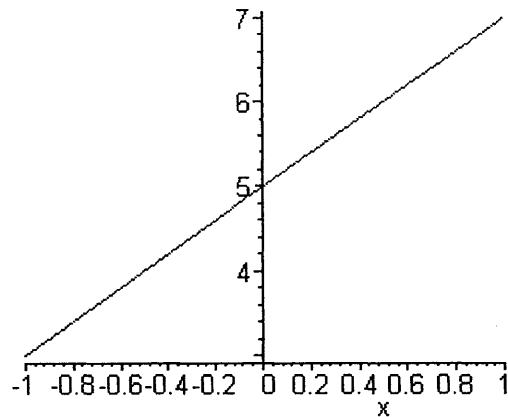


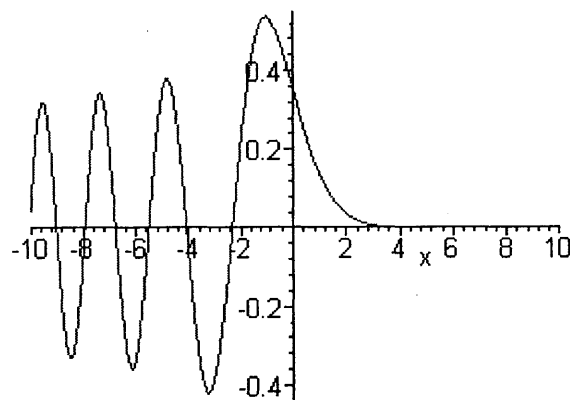Figure 4.9. A schematic plot for the spring constant variations in space.



Figure 4.10. The Airy function $Ai$.

The beam and the tensioned-beam cases are more involved due to the lack of a special function in the high order problem such as the Airy function just shown. Here a

55

tensioned-beam problem is elaborated to demonstrate the procedure for solving this problem. Basically we have to use the integral representation for the equation, and then solve the approximate solutions in three different regions: 1. close to the turning point, 2. left of the turning point, and 3. right of the turning point. The solution close to the turning point is approximated using Taylor's series expansions. The solutions on the left and the right sides are obtained by the steepest descent method. These three solutions match in the overlapping regions and we obtain results similar to the Airy function.

The detailed derivations of the solutions for the turning point problem are shown in Appendix 1. Here we only demonstrate the final results of the sophisticated calculations. Figure 4.11 shows four solutions for a typical tensioned beam with linearly varying stiffness. Solution B has the behavior similar to Airy function $Ai$. To obtain a physically meaningful solution for a specific problem, boundary conditions have to be imposed to decide the weighting of each of these four solutions. For example, an incident wave from the left side for an infinitely long tensioned beam cannot have infinitely large response a the right side. Thus, only solutions B and D in the figure, both of which have small values for large $x$, can satisfy this radiation condition requirement.
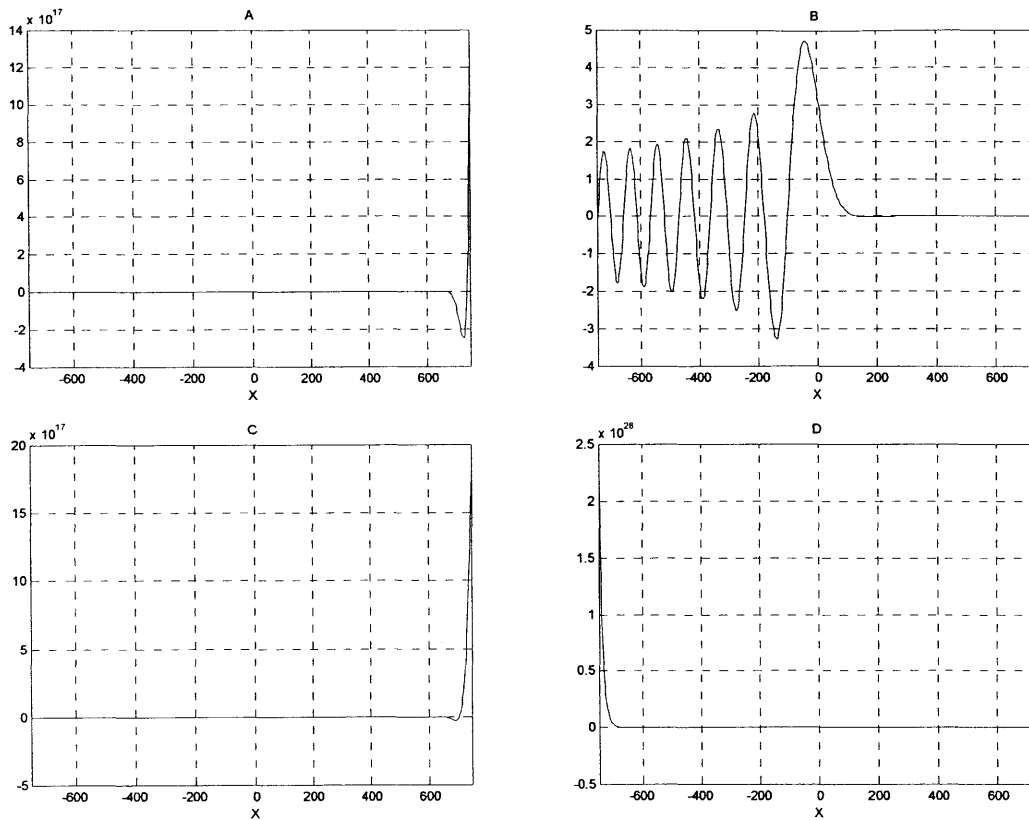
Figure 4.11. Four solutions for a typical tensioned beam with linearly varying spring constant.

## 4.4 Data Analysis for the Effects of Boundary Conditions

With the understanding of the theoretical background from previous sections, we would like to report the experimental results for two kinds of boundary conditions: the material discontinuity between the bare pipe and the buoyant pipe and the soil boundary conditions at the touch-down point (TDP). We will use the theoretical outcome to interpret the experimental results.

In the CVAR test, pups 1 to 5 were mounted on the side of the bare pipes, while pups 6 to 8 were mounted on the side of the buoyant pipes. Thus, the data are useful for investigating the bare-buoyant discontinuity boundary conditions. The total mass per unit length of the buoyant pipe is larger than that of the bare pipe. According to the wave number formula as in Equation 3.3, when the mass per unit length increases, the wave number also increases. Equation 4.12 for the power balance shows that when wave

57

number increases, the displacement amplitude decreases. Therefore, we anticipate that the displacement amplitudes are smaller in the buoyant pipe portion than in the bare pipe portion. Because the wave number is also a function of the wave frequency, it is more useful to look at the spatial variations of the response one frequency at a time. Figure 4.12 illustrates the RMS displacements of a CVAR test with top-end period 3 sec and top-end amplitude 3 ft. Each of these curves represents the RMS displacements for a frequency interval. The frequency interval for each curve is equal to the top-end excitation frequency of the corresponding case. That is, we use the frequency partitioning technique to distinguish different frequency contents. In order to demonstrate the decreasing ratio between the two sides, we re-scale all the curves so that the mean of each curve is 1. It can be clearly seen that there is an amplitude jump between pup 5 and pup 6. The left side with buoyant modules has smaller amplitudes as expected.
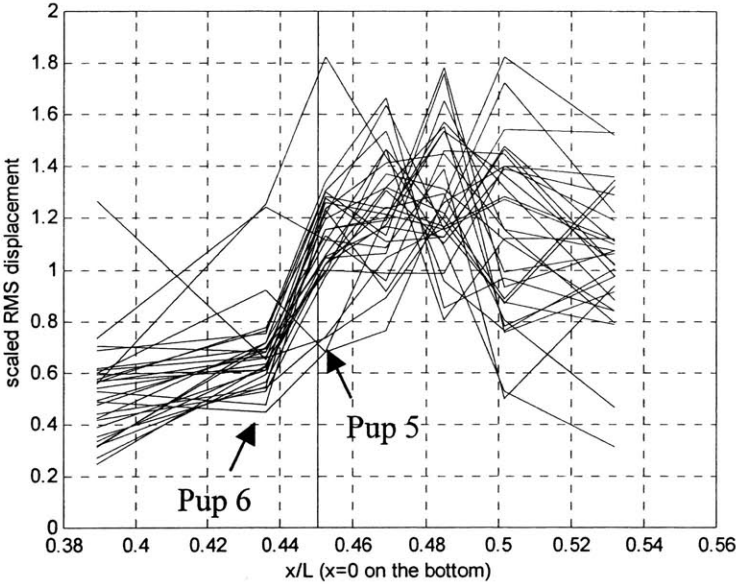


Figure 4.12. The spatial variations of the RMS displacements for CVAR, top-end amplitude 3 ft, top-end period 3 sec. The vertical line is the location of the material discontinuity. RMS displacements are scaled to make the mean of each curve equal 1.

To obtain the theoretical predictions of the response, the specifications of the riser and the buoyant modules are needed. For the bare pipe, we use the same material properties as in Section 3.3, except that the added mass is included now. Including the added mass,

the mass per unit length for the bare pipe is 3.77 kg/m. The buoyant modules have comparatively small bending stiffness, and the mass per unit length is different from that for the bare pipe. The bare pipe in the buoyant part has mass per unit length 2.66 kg/m (not including the added mass). The buoyant module has density 40 lb/ft$^3$, and it has OD=4.8025 in and ID=1.75 in. Therefore, the mass per unit length for the module is 6.50 kg/m and the added mass per unit length is 11.7 kg/m. The total mass per unit length for the buoyant pipe is then 20.9 kg/m. The tension variation for the CVAR is shown in Figure 4.13. With this information, we can calculate the RMS displacements for different frequencies. The comparisons between the experimental and the theoretical results are shown in Figure 4.14. Notice that the amplitude jump around the material discontinuity agrees well between the measurements and the theoretical predictions. Thus, the model for the discontinuity in a previous section is verified by the data.
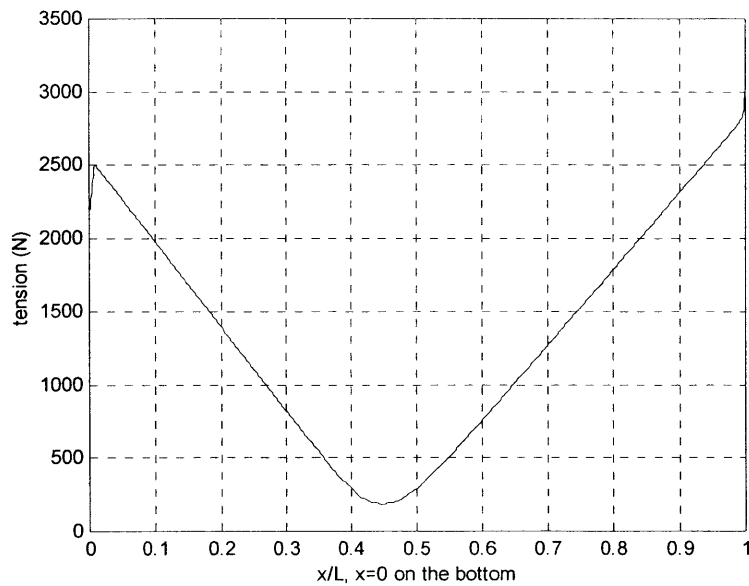


Figure 4.13. The tension variation for the CVAR test. This is estimated from finite element analysis.

59
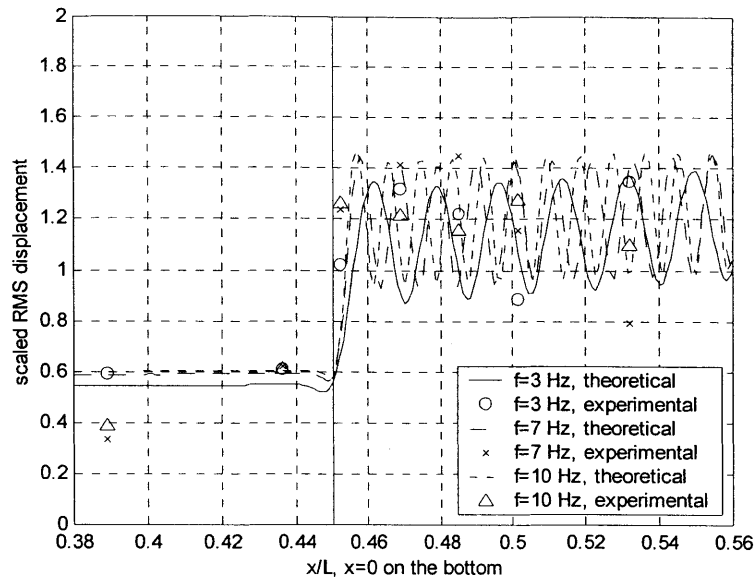
Figure 4.14. The comparisons between the experimental and the theoretical results of the RMS displacements for the top-end excitation amplitude 3 ft, the period 3sec. The RMS displacements shown here are rescaled so that the mean value along the whole length for each set of data is 1.

The problem for soil interactions is more complicated. The SCR test is suitable for testing the soil interaction model. In this test, the pups are around the TDP, so we are able to observe the response above and below the TDP. There are two directions of the top-end excitations for the SCR. The vertical excitation drives the riser in the in-plane direction and the VIV is mainly in the out-of-plane direction. In contrast, the horizontal excitation drives the riser in the out-of-plane direction and the VIV is in the in-plane direction. At the part of the riser sitting upon the soil, the in-plane motion will hit the soil while the out-of-plane motion will sweep the soil. Thus, the wave behavior may be different in the two different directions. It is also expected that the spatial variations of the response will be frequency dependent. That is, the waves with the same frequency will have the same wavelength, and the wave behavior will be similar. Therefore, we use the frequency partitioning technique to separate the frequency components in the response. The RMS displacements of different pups for different frequencies are demonstrated in Figures 4.15. The response is in the in-plane direction, while the excitation is horizontal and in

60

the out-of-plane direction. Each single curve in any figure represents the measurements of one excitation test for a specific frequency range. All the RMS displacements are normalized so that the average value of the measurements in one test is 1. Normalizing is a necessary step because it enables the comparisons among different excitation tests. With the aid of the normalization, it clearly shows that the trends of the spatial variation in each subplot (one frequency partition) are very similar. This figure facilitates the analysis of the soil effects to the riser motions.
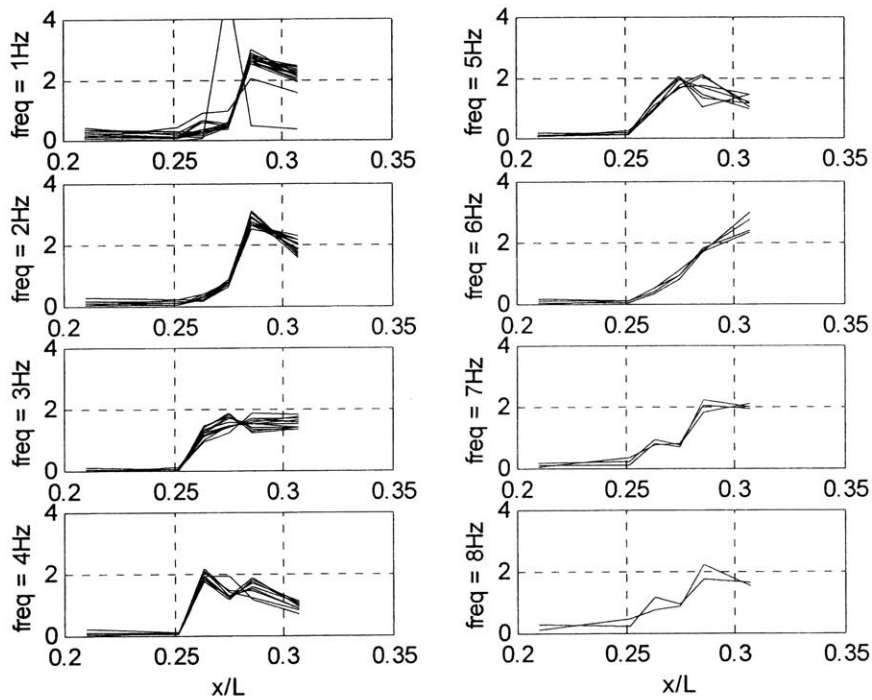


Figure 4.15. The spatial variations of RMS displacements for SCR, horizontal excitation, in-plane response. Each curve corresponds to one combination of the top-end excitation at a frequency interval.

From this figure, we see that the positions with negligible response are different for different frequencies. For frequency = 1 Hz, the location with small RMS displacement is at around x/L = 0.26-0.27. For frequency = 2 Hz, this location starts to move toward left, and for the rest of the frequencies the location is at about x/L = 0.25. Only when frequency = 8 Hz, small response is observed at the left side. A possible explanation for this feature is the spatially varying soil stiffness. As in Section 4.3, where we introduced

a linearly varying foundation stiffness, the cutoff frequencies along the riser are spatially varying. From frequency 1 Hz to 3 Hz, the waves coming from the right penetrate more and more toward the left as the wave frequency increases. As the frequencies are above 3 Hz, the waves hit a relatively hard foundation around x/L = 0.25, where the foundation stiffness is much larger than the right side of the riser. This behavior is reasonable because the catenary riser lies deeper and deeper toward the anchor end. We assume the TDP of the riser is at about x/L = 0.28, and thus, as x/L gets smaller, the stiffness of the soil effect gets larger. When frequency goes up to 8 Hz, the waves start to penetrate more because the frequency is above the cutoff frequency of this harder part of the soil. Theoretically, the wavelength can be calculated from the material properties EI, tension, mass per unit length, and the foundation stiffness. Due to the low spatial resolution, we are not able to obtain a good foundation stiffness model, and thus it is not easy to calibrate the results. One more observation is that the spatial decay for high frequencies is large. As seen in the plots for frequencies 6 and 7 Hz in Figure 4.15, the RMS displacements drop at least 90% in about 20 m (approximately 2 wavelengths). Using the logarithmic decrement, we get an approximated damping ratio of about 0.18. From all the observations above, we suggest that the soil interactions can be modeled as a spatially varying elastic foundation with strong damping. A detailed model of the soil effects requires more sensors close to the touch-down point region. Though the boundary conditions caused by the soil may be complicated, we will show in the next section that simple kinds of boundary conditions are sufficient to conservatively predict the fatigue damage rate.

## 4.5 Soil Interaction Model

In this section, we will compare the effects of different soil models in terms of various boundary conditions and ascertain a conservative and simple model for the soil interactions.

First, let us consider a pinned end model for the TDP. For a tensioned beam without damping, we can express the wave propagation solution as

$$y = Ae^{-i(\gamma x + \omega t)} + Be^{i(\gamma x - \omega t)} + Ce^{-\gamma x}e^{-i\omega t} + De^{\gamma x}e^{-i\omega t}. \qquad (4.18)$$

Assuming the TDP is at $x = 0$ and the incident wave comes from the side $x < 0$, we immediately get $C = 0$ due to the limit amplitude at $x \to -\infty$. Imposing the boundary conditions $y(0,t) = y''(0,t) = 0$ for the pinned end, we obtain

$$
\begin{aligned}
A + B + D &= 0, \\
-A - B + D &= 0,
\end{aligned}
\qquad (4.19)
$$

or

$$
\begin{aligned}
D &= 0, \\
B &= -A.
\end{aligned}
\qquad (4.20)
$$

The solution thus is written as

$$
\begin{aligned}
y &= A(e^{-i(\gamma x + \omega t)} - e^{i(\gamma x + \omega t)}) \\
&= -2iA \sin \gamma x \cdot e^{-i\omega t}.
\end{aligned}
\qquad (4.21)
$$

This is a normal mode solution for the displacement, and the corresponding curvature solution is

$$y'' = 2iA\gamma^2 \sin \gamma x \cdot e^{-i\omega t}. \qquad (4.22)$$

As an example, we assume an incident wave with the amplitude $A = 1$ m and the frequency $\omega = 4$ rad/s, and the system is a tensioned beam with the tension $2 \times 10^6$ N, Young's modulus $2 \times 10^{11}$ N/m$^2$, the moment of inertia 0.0025 m$^4$, and the mass per unit length 1000 kg/m. The RMS displacement and the RMS curvature for the pinned end boundary conditions are shown in Figure 4.16. The left side is the part without touching the soil, while the right side is the part of the riser laying on the soil. The maximum amplitude for the RMS displacement is about $\sqrt{2}$, which is correct for a standing wave amplitude of 2.0, which results from a complete reflection of the pinned boundary conditions. The maximum RMS curvature is about 0.0057 1/m, which is actually $\sqrt{2}\gamma^2$, as can be inferred from Equation 4.22.

Figure 4.16. The RMS displacement and the RMS curvature for a tensioned beam with pinned end at $x = 0$ as the model of the TDP.

For a tensioned beam with a clamped end, we impose the boundary conditions

$$y(0,t) = 0,$$
$$y'(0,t) = 0,$$

(4.23)

into the solution Equation 4.18 and get

$$A + B + D = 0,$$
$$-iA + iB + D = 0,$$

(4.24)

or

$$B = -iA,$$
$$D = (i-1)A.$$

(4.25)

The solution for the displacement becomes

$$y = A[e^{-i(\gamma x + \omega t)} - ie^{i(\gamma x - \omega t)} + (i-1)e^{\gamma x}e^{-i\omega t}].$$

(4.26)

The corresponding solution for the curvature is

$$y'' = A[-\gamma^2 e^{-i(\gamma x + \omega t)} + i\gamma^2 e^{i(\gamma x - \omega t)} + (i-1)\gamma^2 e^{\gamma x}e^{-i\omega t}].$$

(4.27)

For the same material properties and the same unit incident wave as in the pinned end case, the RMS displacement and the RMS curvature for the clamped end boundary

64

conditions are demonstrated in Figure 4.17. The RMS displacement is slightly larger near
the TDP, while the maximum value of the RMS curvature is about 0.008 at $x = 0$. This
maximum RMS curvature can be calculated by setting $x = 0$ for Equation 4.27, and the
curvature (for a unit incident wave) becomes

$$y''(x = 0) = (-2 + 2i)\gamma^2 e^{-i\omega t}. \tag{4.28}$$

The magnitude is $2\sqrt{2}\gamma^2$, and the RMS value is $2\gamma^2$, which is $\sqrt{2}$ times of the
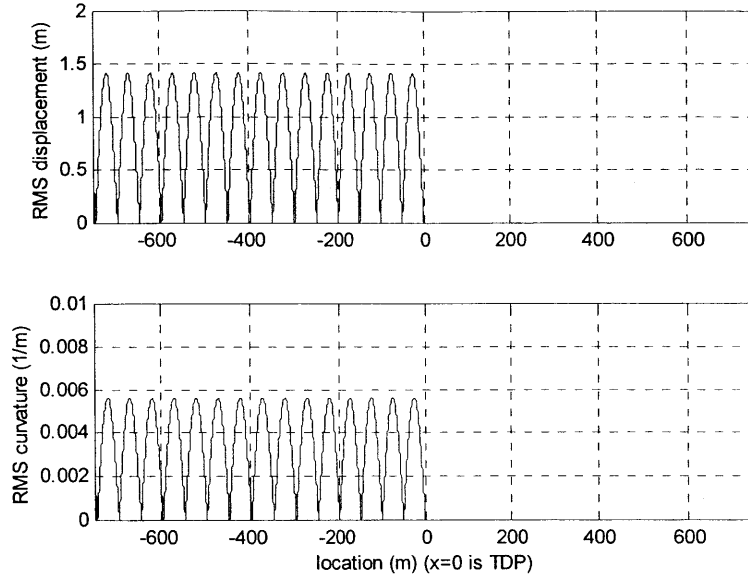maximum curvature for a pinned end case.
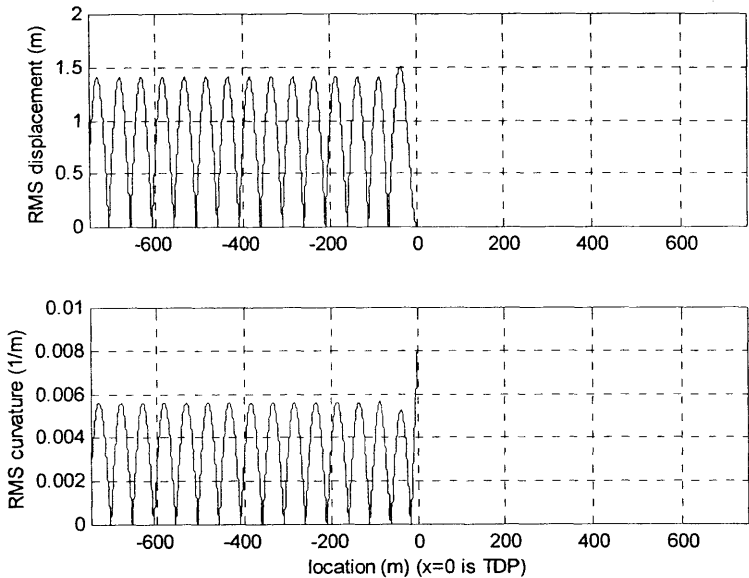


Figure 4.17. The RMS displacement and the RMS curvature for a tensioned beam with
clamped end at $x = 0$ as the model of the TDP.

The solutions for more complicated boundary conditions have been developed in
previous sections. If we model the soil as an elastic foundation with a constant stiffness,
the results in Section 4.1 can be used and the response depends on whether the wave
frequency is above or below the cutoff frequency of the soil foundation. Figure 4.18
shows the RMS displacement for a tensioned beam with an elastic foundation as the soil
model. The soil stiffness is 32000 N/m$^2$ and the wave is below the cutoff frequency. The
corresponding RMS curvature is shown in Figure 4.19, with comparison to the maximum
RMS curvatures of both the pinned end and the clamped end models. Notice that

65

although the RMS displacement close to the TDP is larger for the elastic foundation model, the maximum RMS curvature for the elastic foundation model is not greater than the RMS curvatures of the pinned end and the clamped end cases. In terms of the fatigue damage rate, which is relevant to the curvature rather than the displacement, the pinned end model is a conservative model compared to the elastic foundation model, and the clamped end model is even more conservative. Furthermore, the calculations with pinned-end or clamped-end boundary conditions are much simpler. For a wave above the cutoff frequency, the RMS displacement and the RMS curvature are shown in Figures 4.20 and 4.21. Because part of the energy of the wave transmits to the soil, the maximum RMS displacement and curvature are both smaller than those for the elastic foundation model, so the pinned end model and the clamped end model still serve as simple and conservative models.



Figure 4.18. The RMS displacement and the corresponding soil stiffness for a tensioned beam with the elastic foundation as the model of the soil. The wave frequency is below the cutoff frequency.

66

Figure 4.19. The RMS curvature for a tensioned beam with the elastic foundation as the model of the soil, as in Figure 4.18. The dashed line is the maximum RMS curvature for the clamped end model and the dashdot line is the maximum RMS curvature for the pinned end model. The wave frequency is below the cutoff frequency.
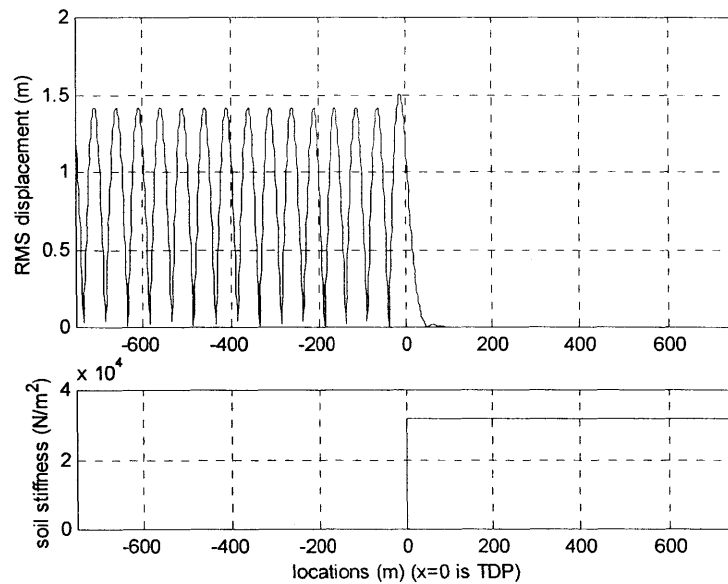


Figure 4.20. The RMS displacement and the corresponding soil stiffness for a tensioned beam with the elastic foundation as the model of the soil. The wave frequency is above the cutoff frequency.
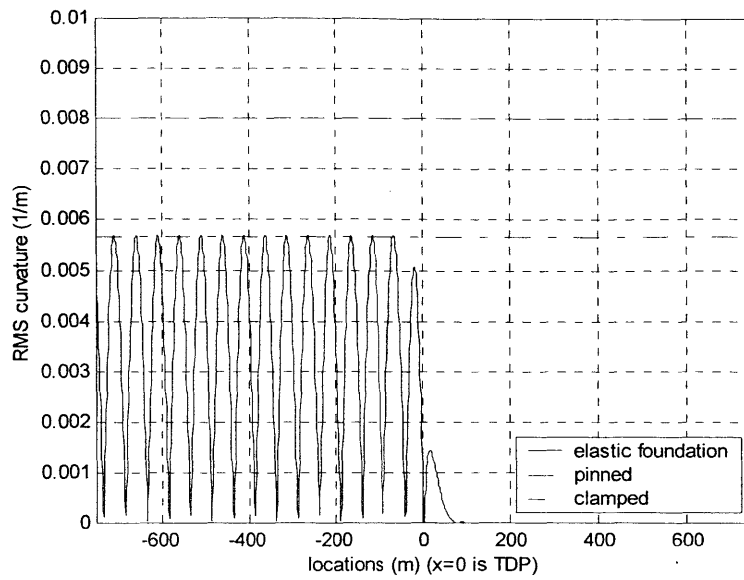
Figure 4.21. The RMS curvature for a tensioned beam with the elastic foundation as the model of the soil, as in Figure 4.20. The dashed line is the maximum RMS curvature for the clamped end model and the dashdot line is the maximum RMS curvature for the pinned end model. The wave frequency is above the cutoff frequency.

For an elastic foundation with linearly varying stiffness in space as the soil model, the solutions are available in Section 4.3 by applying the steepest descend method. This is a reasonable model because the contact between the riser and the soil tends to get deeper going from the TDP toward the anchoring point. Figure 4.22 shows the RMS displacement of a tensioned beam and the corresponding foundation stiffness. The location $x = 0$ is the TDP, from where the soil stiffness increases linearly in space. As can be seen in the figure, the displacements also increase in the positive $x$ direction, as well as the wavelengths. The turning point is at the location where the cutoff frequency equals the wave frequency. For a 4 Hz wave on the riser with the mass per unit length 1000 kg/m, the stiffness at the turning point should be 16000 $N/m^2$. From the subplot for the stiffness, we know that the turning point is at $x = 500$ m. Around $x = 500$ m the displacements drop suddenly due to the cutoff frequency barrier at $x > 500$ m. Figure 4.23 shows the RMS curvature for the same foundation model. Interestingly, although the displacements increase as $x$ gets larger, the corresponding curvatures decrease for larger

$x$. This decrease is due to the increase of the wavelength. The curvature is proportional to the square of the wave number, and thus it is inversely proportional to the wavelength square. As can be seen in Figure 4.23, the maximum RMS curvature is not larger than the maximum RMS curvatures for both the pinned end and the clamped end models. Therefore, we can safely use the pinned end model for the TDP in terms of conservative estimation of the fatigue damage rate.
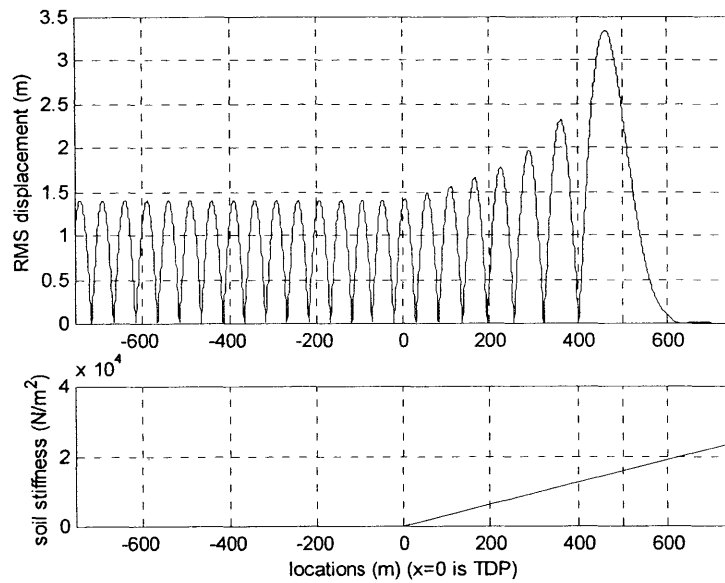
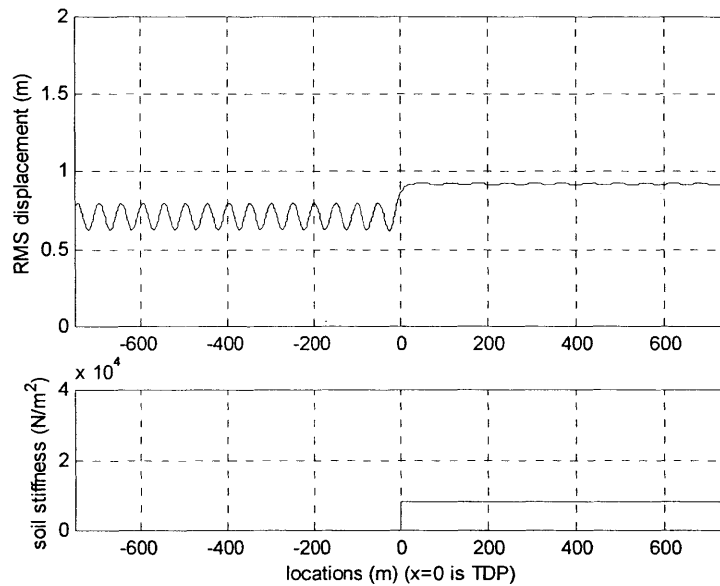

Figure 4.22. The RMS displacement and the corresponding soil stiffness for a tensioned beam with the elastic foundation linearly varying in space as the model of the soil. At $x = 500$ m the wave frequency equals the cutoff frequency.
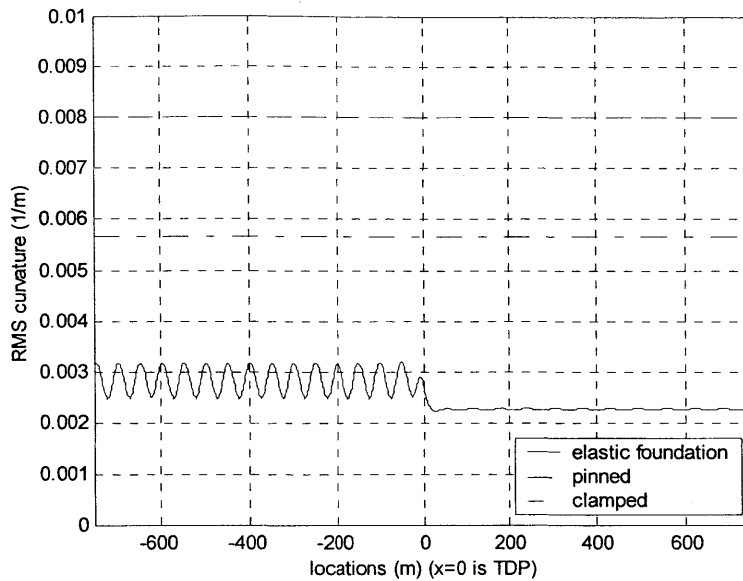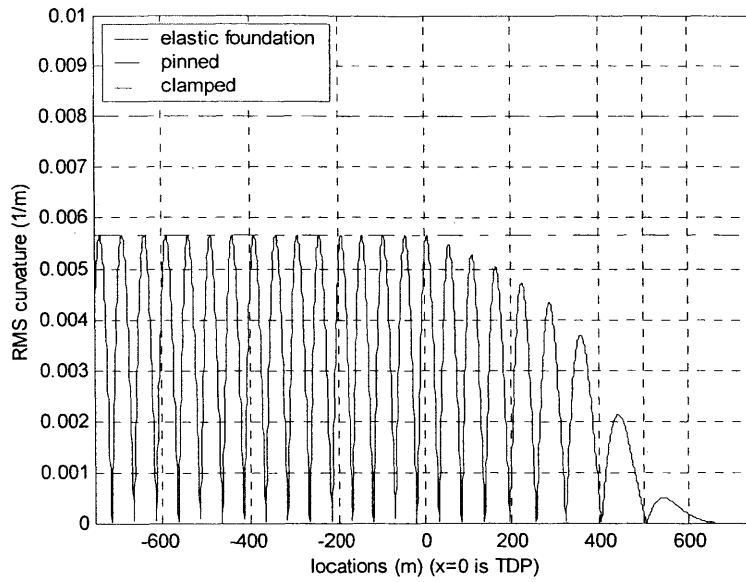
Figure 4.23. The RMS curvature for a tensioned beam with the linearly varying elastic foundation as the model of the soil, as in Figure 4.22. The dashed line is the maximum RMS curvature for the clamped end model and the dashdot line is the maximum RMS curvature for the pinned end model. At $x = 500$ m the wave frequency equals the cutoff frequency.

Above all, we know it is conservative to use the simple pinned end model at the TDP for the complicated soil interactions in terms of the fatigue damage rate, and a simple clamped end model is even more conservative.

# Chapter 5 Unsteady VIV Model

## 5.1 The Approach to the Unsteady VIV Problem

VIV due to top-end periodic motion consists of two kinds of complexity: non-uniformity and unsteadiness. To develop the prediction tools for this complicated problem, we have to understand and quantitatively evaluate the dimensionless parameters that characterize the VIV behavior of risers under unsteady flow conditions. In this chapter we will develop an approach to model the unsteady VIV from the available data.

We first show the final results of the model in this section, so that the direction of the approach will be clearer.

The principal concept of the method we develop is to use the important dimensionless parameter, the reduced damping $S_g$, to explain the relationship between the excitation and the response. The reduced damping $S_g$ for steady flow is defined as

$$S_g = \frac{R\omega}{\rho_f V^2},$$ (5.1)

as described in Chapter 2. Some experimental results for the $S_g$-RMS A/D relationship for a flexible cylinder under uniform steady current were compiled by Griffin (1980). A curve fit to the published experimental data is shown as a thick line in Figure 5.1. With the additional lines for constant lift coefficients, we understand that when the reduced damping is large, the lift coefficient tends to be a constant, but when the reduced damping gets smaller, the lift coefficient also gets smaller due to limit cycle effects above 1 diameter amplitude. This relationship is a convenient way to link the damping, the lift, and the response into graphical representation without solving the complicated partial differential equations. Later in this chapter, we will develop an equivalent $S_g$ for the top-end periodic motion induced unsteady vibration. In order to get an impression of the outcome first, we demonstrate the relationship between the equivalent $S_g$ and the response in Figure 5.2. The equivalent $S_g$ will be defined carefully later in this chapter. This plot shows exceptional agreement with the curve for steady uniform flow. This good

agreement shows that by properly choosing the equivalent reduced damping, we will be able to use the same curve as in the uniform flow to predict the response.
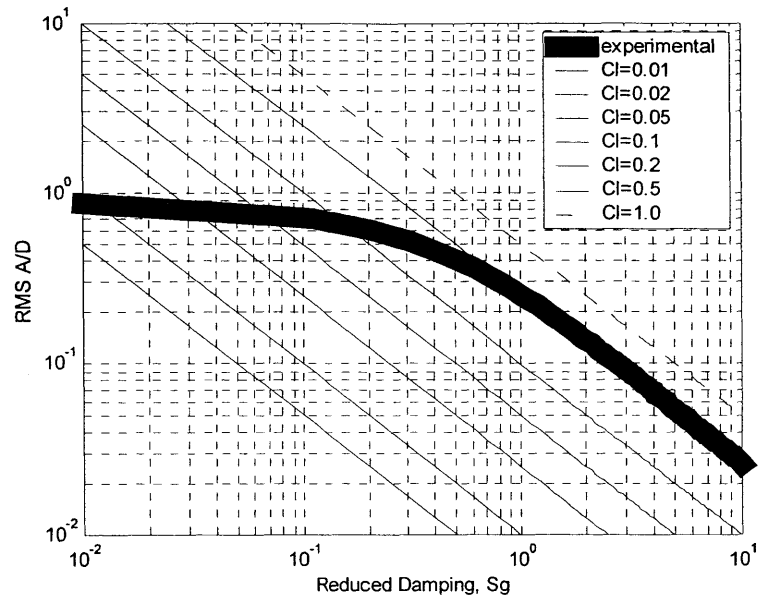


Figure 5.1. The relationship between the reduced damping and RMS A/D for a steady current VIV. A curve (the thick curve) fit to the published experimental data is shown, and each diagonal line is the $S_g$-RMS A/D relationship for a constant lift coefficient.
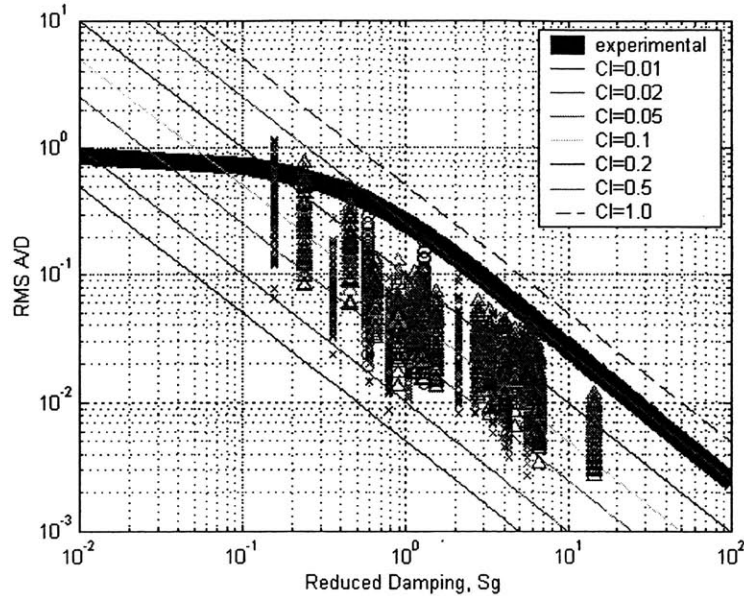
Figure 5.2. The relationship between the equivalent reduced damping $S_{ge}$ and RMS A/D. The reduced damping is obtained from the CVAR unsteady flow profile, and the RMS displacements are from measurements with frequency partitioning. The data include all different combinations (period and amplitude) of top-end excitation, and measurements from all pups.

The essential task is to define the equivalent $S_g$ for the unsteady VIV problem. As shown in Equation 5.1, $S_g$ is a function of frequency. Therefore, we will develop a method to consider different frequencies separately. A frequency partitioning technique will be introduced to achieve this goal. In addition, the effects of the non-uniformity and the unsteadiness should be considered. We will establish the procedure to obtain the equivalent $S_g$ in this chapter.

## 5.2 Top-end Motion: Response Amplification

Before proceeding to the reduced damping model, we first investigate the effects of the top-end periodic motion on the inline velocities along the riser. Though the velocity profile for HCR has been calculated by the finite element method and the results have been shown, we would like to know analytically how the moving boundary conditions

influence the motions along the riser. At the end of this section, we will find that the wave propagation parameter $n\varsigma$, the product of the mode number and the damping ratio, is the key dimensionless parameter governing the maximum inline amplitude along the riser under a top-end periodic motion.

To demonstrate the effects of the moving boundary conditions, we use a very simple model, a string with constant damping. The governing equation is

$$-T\frac{\partial^2 y}{\partial x^2} + m\frac{\partial^2 y}{\partial t^2} + c\frac{\partial y}{\partial x} = 0, \tag{5.2}$$

and the boundary conditions are

$$y(0,t) = 0,$$
$$y(L,t) = Ae^{-i\omega_0 t}. \tag{5.3}$$

That is, the total length of the riser is $L$, and the end at $x = 0$ is fixed, while the end at $x = L$ is the top end with a sinusoidal moving boundary with frequency $\omega_0$. Assuming a wave propagating solution $y = e^{i(\gamma x - \omega t)}$, we get the dispersion relation

$$T\gamma^2 - m\omega^2 - ic\omega = 0, \tag{5.4}$$

or

$$\gamma = \pm\left(\frac{m\omega^2 + ic\omega}{T}\right)^{\frac{1}{2}} \equiv \pm\gamma_1, \tag{5.5}$$

where $\gamma_1$ is a complex number. We introduce the damping ratio

$$\varsigma = \frac{c}{2m\omega}, \tag{5.6}$$

so the wave number can be written as

$$\gamma = \pm\gamma_1 = \pm\left(\frac{m\omega^2 + i2m\omega^2\varsigma}{T}\right)^{\frac{1}{2}}$$
$$= \pm\left(\frac{m\omega^2}{T}\right)^{\frac{1}{2}}(1 + i2\varsigma)^{\frac{1}{2}}. \tag{5.7}$$

The solution thus can be expressed as

$$y = \alpha e^{i(\gamma_1 x - \omega t)} + \beta e^{i(-\gamma_1 x - \omega t)}. \tag{5.8}$$

To determine the coefficients $\alpha$ and $\beta$, we impose the boundary conditions and get

$$\alpha + \beta = 0,$$
$$\alpha e^{i\gamma_1 L} + \beta e^{-i\gamma_1 L} = A. \tag{5.9}$$

From the second boundary condition we also know that the frequency follows

$$\omega = \omega_0. \tag{5.10}$$

Obtaining the coefficients and plugging them into Equation 5.8, we get the solution

$$y = A \frac{e^{i\gamma_1 x} - e^{-i\gamma_1 x}}{e^{i\gamma_1 L} - e^{-i\gamma_1 L}} e^{-i\omega_0 t}. \tag{5.11}$$

With this result, we are able to run the dynamic simulation for the response due to the moving boundary conditions. Figure 5.3 shows the traces of the response during a period of time for two different damping ratios. The left end is fixed while the right end moves sinusoidally with unit amplitude in both cases. Notice that the maximum amplitudes along both strings are larger than 1 at the anti-nodes. This behavior is the response amplification associated with moving boundary conditions. The amplification factor, defined as the ratio between the maximum response amplitude to the moving boundary amplitude, is larger for a smaller damping ratio, as can be seen in Figure 5.3. The response amplification is important for the VIV problem because the top-end vessel motion with small amplitude may end up generating a large inline motion somewhere in the riser. This may cause significant VIV, which may not be anticipated from the small amplitude vessel motion. Figure 5.4 demonstrates the influence of different top-end frequencies on the amplification factor. It can be seen that when the frequency is a multiple of the 1st natural frequency, that is, one of the undamped natural frequencies, the amplification factor is large, compared to the factor for frequencies off the natural frequencies. As mode numbers get higher, the peaks of amplification factors become lower, and finally the amplification factor becomes unimportant for very large mode number.

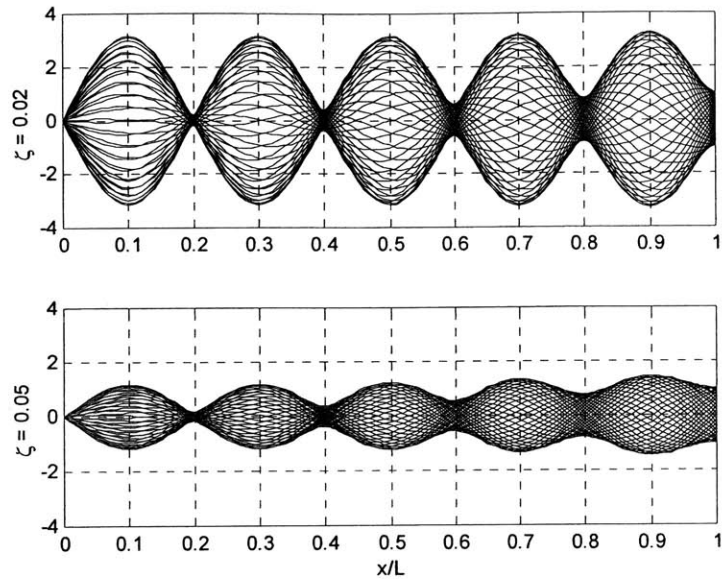Figure 5.3. The traces of the response to the sinusoidal moving boundary condition at $x/L = 1$. Two different damping ratios are shown with the same amplitude (unit amplitude) moving boundaries.
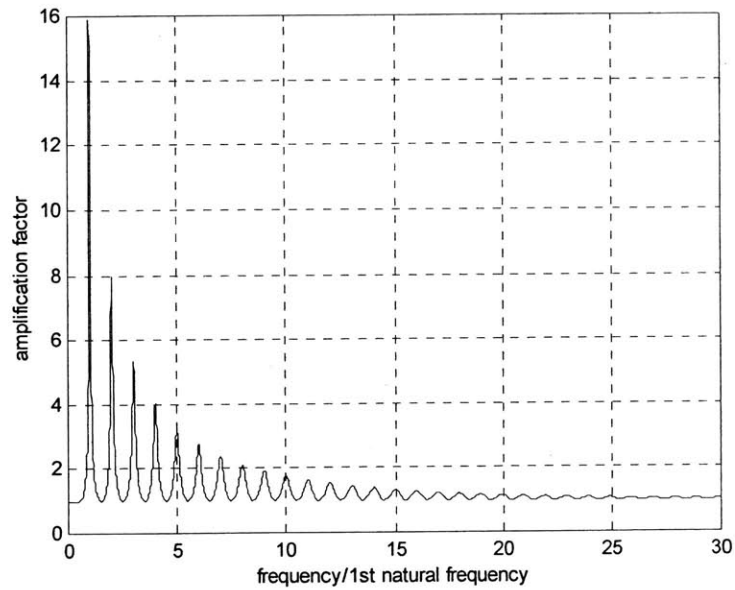


Figure 5.4. The amplification factor with respect to different moving boundary frequencies. The frequencies in the x-axis are normalized by the $1^{st}$ undamped natural frequency of the string. The damping ratio is 0.02.

To illustrate how the amplitudes of the amplification factors are affected by the moving boundary conditions, we have to establish the relationship between the response amplitude and the moving boundary frequency. Assuming a unit amplitude moving boundary, we have the response from Equation 5.11

$$Y = \frac{e^{i\gamma_1 x} - e^{-i\gamma_1 x}}{e^{i\gamma_1 L} - e^{-i\gamma_1 L}}. \tag{5.12}$$

If we assume small damping ratio, then the wave number in Equation 5.7 can be approximated to

$$\gamma_1 = \left(\frac{m\omega^2}{T}\right)^{1/2} (1 + i2\varsigma)^{1/2}$$

$$\sim \left(\frac{m\omega^2}{T}\right)^{1/2} (1 + i\varsigma). \tag{5.13}$$

The amplification factors we are most interested in are those at the natural frequencies, where the undamped natural frequencies are

$$\omega_n = \frac{n\pi}{L}\sqrt{\frac{T}{m}}. \tag{5.14}$$

Plugging the natural frequencies into Equation 5.13, we get the wave number

$$\gamma_1 \sim \frac{n\pi}{L}(1 + i\varsigma). \tag{5.15}$$

With this simplified $\gamma_1$, we can rewrite Equation 5.12 for the response as

$$Y = \frac{e^{i\frac{n\pi x}{L}}e^{-\varsigma\frac{n\pi x}{L}} - e^{-i\frac{n\pi x}{L}}e^{\varsigma\frac{n\pi x}{L}}}{e^{in\pi}e^{-\varsigma n\pi} - e^{-in\pi}e^{\varsigma n\pi}}$$

$$= (-1)^n \frac{e^{i\frac{n\pi x}{L}}e^{-\varsigma\frac{n\pi x}{L}} - e^{-i\frac{n\pi x}{L}}e^{\varsigma\frac{n\pi x}{L}}}{e^{-\varsigma n\pi} - e^{\varsigma n\pi}}. \tag{5.16}$$

Here we have to decide where the maximum response occurs along the riser, so that we can plug in a suitable value of $x$ to evaluate $Y$. Figure 5.3 shows that the maximum response for both damping ratios arise at around $x / L = 0.9$. This location is at the anti-node closest to the moving boundary. More generally, for the boundary frequency at the n-th mode, the far right anti-node will be at

77

$$x/L = \frac{2n-1}{2n}.$$ 

(5.17)

Inserting this term into Equation 5.16, we get

$$Y = (-1)^n \frac{e^{in\pi\frac{2n-1}{2n}}e^{-\varsigma n\pi\frac{2n-1}{2n}} - e^{-in\pi\frac{2n-1}{2n}}e^{\varsigma n\pi\frac{2n-1}{2n}}}{e^{-\varsigma n\pi} - e^{\varsigma n\pi}}$$

$$= i\frac{e^{\varsigma n\pi - \frac{\varsigma\pi}{2}} + e^{-\varsigma n\pi + \frac{\varsigma\pi}{2}}}{e^{\varsigma n\pi} - e^{-\varsigma n\pi}}.$$

(5.18)

Equation 5.18 is the maximum response amplitude for the boundary frequency at one of the natural frequencies. For small $\pi n\varsigma$, we can further simplify the response by introducing the series expansion of an exponent

$$e^x = 1 + x + \frac{x^2}{2!} + \frac{x^3}{3!} + \dots$$

(5.19)

and taking only the first two terms we get

$$Y = i\frac{(1 + \varsigma n\pi - \frac{\varsigma\pi}{2}) + (1 - \varsigma n\pi + \frac{\varsigma\pi}{2})}{(1 + \varsigma n\pi) - (1 - \varsigma n\pi)}$$

$$= \frac{i}{\pi n\varsigma}.$$

(5.20)

That is, when $\pi n\varsigma$ is small, the amplitude will be approximately $\frac{1}{\pi n\varsigma}$. In Figure 5.4, the damping ratio is 0.02, so the estimated amplification factors for the first three modes will be about 15.92, 7.96, 5.31, very close to the magnitudes of the peaks in Figure 5.4. For large $\pi n\varsigma$ (mostly due to very large $n$),

$$e^{\pi n\varsigma} \gg e^{-\pi n\varsigma},$$

(5.21)

and thus the response is approximately

$$Y = i\frac{e^{\varsigma n\pi}}{e^{\varsigma n\pi}} = i.$$

(5.22)

That is, the amplification factor for large $\pi n\varsigma$ is 1, the same as the simulation result. From these results, we know that $n\varsigma$ is a very important parameter. It not only determines whether the amplification factor is significant or not, but also quantitatively provides the solutions for small $n\varsigma$. For the HCR experiments we discuss in this thesis,

78

the top-end motions are at around the 50$^{th}$ to 100$^{th}$ modes, so the amplification factor is not a critical problem. However, for other risers excited at low modes, the effects of the amplification factor should definitely be considered.

The string model discussed above takes the simple form of the solution. We introduce how to proceed for a straight tensioned beam with damping, and the study for the effects of $n\varsigma$ may need further computer simulation. The governing equation is

$$EI\frac{\partial^4 y}{\partial x^4} - T\frac{\partial^2 y}{\partial x^2} + m\frac{\partial^2 y}{\partial t^2} + c\frac{\partial y}{\partial x} = 0, \tag{5.23}$$

and the boundary conditions for both ends are

$$\begin{aligned} y(0,t) &= 0, \\ y''(0,t) &= 0, \\ y(L,t) &= Ae^{-i\omega_0 t}, \\ y''(L,t) &= 0. \end{aligned} \tag{5.24}$$

That is, the total length of the riser is $L$, and the end at $x = 0$ is a pinned end while the end at $x = L$ is the top-end with a sinusoidal moving boundary with frequency $\omega_0$.

Assuming a propagating wave solution $y = e^{i(\gamma x - \omega t)}$, we get the dispersion relation

$$EI\gamma^4 + T\gamma^2 - m\omega^2 - ic\omega = 0. \tag{5.25}$$

The four roots can be obtained and we can write them as

$$\gamma = \pm\gamma_1, \pm\gamma_2, \tag{5.26}$$

where $\gamma_1, \gamma_2$ are complex numbers. The solution thus can be represented as

$$y = \alpha_1 e^{i(\gamma_1 x - \omega t)} + \beta_1 e^{i(-\gamma_1 x - \omega t)} + \alpha_2 e^{i(\gamma_2 x - \omega t)} + \beta_2 e^{i(-\gamma_2 x - \omega t)}, \tag{5.27}$$

and its second derivative is

$$y'' = -\gamma_1^2 \alpha_1 e^{i(\gamma_1 x - \omega t)} - \gamma_1^2 \beta_1 e^{i(-\gamma_1 x - \omega t)} - \gamma_2^2 \alpha_2 e^{i(\gamma_2 x - \omega t)} - \gamma_2^2 \beta_2 e^{i(-\gamma_2 x - \omega t)}. \tag{5.28}$$

The coefficients $\alpha_1, \beta_1, \alpha_2, \beta_2$ are unknown and should be determined by the four boundary conditions. We impose the boundary conditions in Equation 5.24 and get four equations:

$$\alpha_1 + \beta_1 + \alpha_2 + \beta_2 = 0,$$

$$-\gamma_1^2 \alpha_1 - \gamma_1^2 \beta_1 - \gamma_2^2 \alpha_2 - \gamma_2^2 \beta_2 = 0,$$

$$\alpha_1 e^{i\gamma_1 L} + \beta_1 e^{-i\gamma_1 L} + \alpha_2 e^{i\gamma_2 L} + \beta_2 e^{-i\gamma_2 L} = A, \qquad (5.29)$$

$$-\gamma_1^2 \alpha_1 e^{i\gamma_1 L} - \gamma_1^2 \beta_1 e^{-i\gamma_1 L} - \gamma_2^2 \alpha_2 e^{i\gamma_2 L} - \gamma_2^2 \beta_2 e^{-i\gamma_2 L} = 0.$$

Notice that from the third boundary condition, we also obtain the frequency

$$\omega = \omega_0. \qquad (5.30)$$

Equation 5.29 can also be written in a matrix form

$$\begin{bmatrix} 1 & 1 & 1 & 1 \\ -\gamma_1^2 & -\gamma_1^2 & -\gamma_2^2 & -\gamma_2^2 \\ e^{i\gamma_1 L} & e^{-i\gamma_1 L} & e^{i\gamma_2 L} & e^{-i\gamma_2 L} \\ -\gamma_1^2 e^{i\gamma_1 L} & -\gamma_1^2 e^{-i\gamma_1 L} & -\gamma_2^2 e^{i\gamma_2 L} & -\gamma_2^2 e^{-i\gamma_2 L} \end{bmatrix} \begin{Bmatrix} \alpha_1 \\ \beta_1 \\ \alpha_2 \\ \beta_2 \end{Bmatrix} = \begin{Bmatrix} 0 \\ 0 \\ A \\ 0 \end{Bmatrix}. \qquad (5.31)$$

From the matrix form we can obtain the dynamic response of the moving boundary conditions by computer simulations. The results for the tensioned beam are qualitatively very similar to the result for the string, as in Figure 5.4, except that the space between adjacent peaks is different for high modes.

## 5.3 Reduced Damping $S_g$ for Steady Flow

The reduced damping, $S_g = \dfrac{R\omega}{\rho_f V^2}$, has been introduced as a parameter to account for the relative importance of the damping force and the fluid excitation force. A physical problem can show the appearance of $S_g$ in the solution. For a spring-mounted rigid cylinder with viscous damping under uniform flow, as shown in Figure 5.5, we can write the governing equation as

$$M \frac{\partial^2 y}{\partial t^2} + R \frac{\partial y}{\partial t} + Ky = \frac{1}{2} \rho_f V^2 DC_L \cos\omega t, \qquad (5.32)$$

where $M$ is the mass of the cylinder per unit length, $R$ is the damping coefficient per unit length, $K$ is the spring constant per unit length, and the term at the right hand side is the periodic lift force (per unit length) due to the shedding vortices. Under lock-in conditions, the excitation frequency equals the natural frequency, which is

$$\omega = \omega_n = \sqrt{\frac{K}{M}}. \tag{5.33}$$

At resonance, the solution can be written as

$$y = Y \sin \omega_n t. \tag{5.34}$$

Substituting this solution into the equation, we can cancel the mass term and the spring term. Equating the damping term with the excitation at the right hand side, we get

$$RY\omega = \frac{1}{2}\rho_f V^2 D C_L, \tag{5.35}$$

or

$$\frac{Y}{D} = \frac{1}{2}\frac{\rho_f V^2 C_L}{R\omega} = \frac{C_L}{2S_g}. \tag{5.36}$$

That is, the ratio of the lift coefficient to the reduced damping gives the response amplitude for a spring-mounted cylinder under steady uniform flow. The larger the reduced damping $S_g$, the smaller the response amplitude.
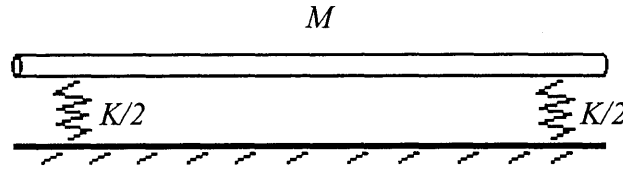


Figure 5.5. A spring-mounted cylinder.

The reduced damping is also important for a flexible cylinder. Consider a long cylinder modeled as a flexible beam with constant bending stiffness. The beam has a power-in region far from both ends. The wave propagation parameter $n_\varsigma$ is sufficiently large that waves travel away from the power-in region and do not return to create a standing wave pattern. An ideal excitation is applied over a finite region of length $L_{in}$. Within the power-in region the excitation force varies sinusoidally in time and also as a standing wave in space. The wavelength is identical to that of waves at the frequency of the excitation. The governing equation can be written as

$$EI\frac{\partial^4 y}{\partial x^4} + R\frac{\partial y}{\partial t} + m\frac{\partial^2 y}{\partial t^2} = f(x)e^{-i\omega t}, \qquad (5.37)$$

with

$$f(x) = \frac{1}{2}\rho_f V^2 DC_L \cos kx, \qquad -L_{in}/2 < x < L_{in}/2$$
$$0, \qquad\qquad\qquad x < -L_{in}/2, x > L_{in}/2, \qquad (5.38)$$

where $k = \left(\dfrac{m\omega^2}{EI}\right)^{1/4}$, the corresponding wave number for the excitation frequency. The

excitation is shown in the upper panel of Figure 5.6. The corresponding response amplitude is demonstrated in the lower panel, and we will describe how to obtain this solution by the procedure of deriving the Green's functions. The details of deriving Green's function solutions are shown in Appendix 2, where both the 'single' Green's function and double Green's function will be discussed.

We assume the system to be infinitely long to remove the reflective interference from the boundaries. Inserting the harmonic solution $y(x) = Y(x)e^{-i\omega t}$ and taking the Fourier transform, we get

$$Y(x) = \frac{\rho_f V^2 DC_L}{4\pi EI}\int_{-\infty}^{\infty}\frac{e^{-i\gamma x}}{\gamma^4 - i2k^4\varsigma - k^4}\left[\frac{\sin(\gamma-k)L_{in}}{2(\gamma-k)} + \frac{\sin(\gamma+k)L_{in}}{2(\gamma+k)}\right]d\gamma, \qquad (5.39)$$

where the damping ratio is defined as $\varsigma = \dfrac{R}{2m\omega}$. After the complicated employment of

the residue theory, we obtain the final result (Green's function solution) as

$$Y(x) = \frac{\rho_f V^2 DC_L}{4EI\gamma_1^3}(e^{i\gamma_1 L_{in}/2}\cos\gamma_1 x\,\frac{\gamma_1\cos\dfrac{kL_{in}}{2} - ik\sin\dfrac{kL_{in}}{2}}{\gamma_1^2 - k^2} +$$

$$+e^{-\gamma_1 L_{in}/2}\cosh\gamma_1 x\,\frac{\gamma_1\cos\dfrac{kL_{in}}{2} - k\sin\dfrac{kL_{in}}{2}}{\gamma_1^2 + k^2}) + \frac{i\rho_f V^2 DC_L\cos kx}{2\omega R}, \qquad (5.40)$$

where $\gamma_1$ is one of the roots of $\gamma^4 - i2k^4\varsigma - k^4 = 0$, and it is the root with positive real and positive imaginary parts. This is the solution valid only in the excitation region. A solution with corresponding excitation is shown in Figure 5.6. The width of the excitation band equals to 4.5 wavelengths. In order to see the trend of the response amplitude with

respect to the width of the excitation band $L_{in}$, we have to simplify Equation 5.40 if possible. We make a few assumptions to approach the simplified result. If we require that the width of the excitation band equals odd multiples of half wavelengths, $\cos\dfrac{kL_{in}}{2}$ and $\sin\dfrac{kL_{in}}{2}$ in Equation 5.40 become 0 and $\pm 1$, and the response at the midpoint is

$$Y(x=0) = \pm\frac{1}{2}\rho_f V^2 DC_L \left(\frac{k\gamma_1^2 (ie^{i\gamma_1 L_{in}/2} + e^{-\gamma_1 L_{in}/2}) + k^3 (ie^{i\gamma_1 L_{in}/2} - e^{-\gamma_1 L_{in}/2})}{2i\gamma_1^3 \omega R} + \frac{i}{\omega R}\right). \quad (5.41)$$

We further assume small damping for the problem, so that the root $\gamma_1$ can be written as

$$\gamma_1 \sim k + i\frac{k\varsigma}{2}. \quad (5.42)$$

Plugging this relation into Equation 5.41 and removing some small terms, we obtain a very simple form for the response at the midpoint:

$$Y(x=0) \sim \frac{i\rho_f V^2 DC_L}{2\omega R}(1 - e^{-\frac{k\varsigma}{4}L_{in}}). \quad (5.43)$$

Or, we can write the response amplitude in term of the reduced damping $S_g$, as:

$$\frac{Y_{max}(x=0)}{D} \sim \frac{C_L}{2S_g}(1 - e^{-\frac{k\varsigma}{4}L_{in}}). \quad (5.44)$$

This result is very important. The reduced damping $S_g$ again appears explicitly in the solution. It shows that the response amplitude at the midpoint will increase when the width of the excitation band $L_{in}$ increases, and it will finally reach a saturated amplitude $\dfrac{C_L}{2S_g}$ as $L_{in}$ approaches infinity. To verify this result, we employ Equation 5.40, the full analytical solution, for different $L_{in}$ and record the amplitude at the midpoint. The comparison between the results from Equation 5.40 and the curve from Equation 5.43 is shown in Figure 5.7. The simplified solution fits remarkably well with the exact solution. This agreement demonstrates the validity of the simple and useful solution of Equation 5.43. If $N_{in}$ is defined as the number of wavelengths that fit into the length $L_{in}$, then $N_{in} = L_{in}/\lambda$ and the above expression may be expressed in terms of $N_{in}$:

$$\frac{Y_{\max}(x=0)}{D} \sim \frac{C_L}{2S_g}(1-e^{-\frac{\pi N_{in}\varsigma}{2}}).$$ 

<div align="right">(5.45)</div>

Thus, the product $N_{in}\varsigma$ is an important parameter to describe the power-in length of the excitation. For an infinitely long beam (i.e., $n\varsigma$ is large enough so that we can ignore the boundary effects), the dimensionless parameters $N_{in}\varsigma$ and $\dfrac{C_L}{2S_g}$ govern the response amplitude for a finite length sinusoidal excitation.
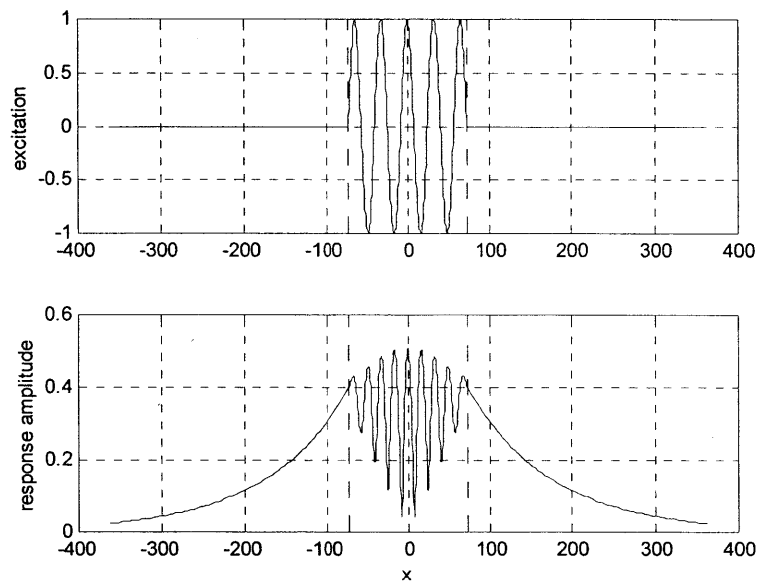


Figure 5.6. The finite length excitation with sinusoidal wave shape and the corresponding response amplitude. The system is modeled as an infinite beam with damping.
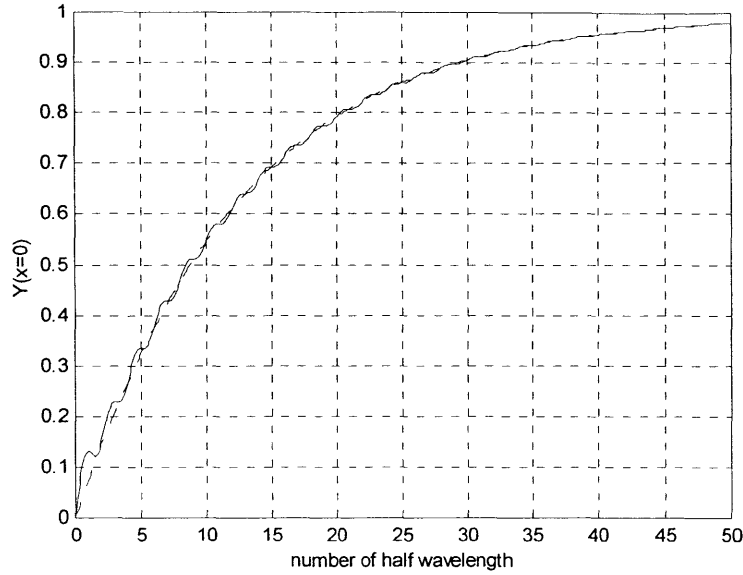
Figure 5.7. The comparison of response amplitude at x=0 between the simulated results (solid line) and the simplified form in Equation 5.43. The damping ratio is 0.1 and the frequency is 1 rad/s.

For a finite system under uniform flow, the experimental data fit has been shown in Figure 5.1. The data shown in Figure 5.1 is for the riser with uniform flow along its whole length. When the flow does not cover the whole length, some modifications are needed for the calculation of $S_g$. For example, a set of experiments was conducted with the lower part of the riser in still water. An example is shown in Figure 5.8. The left side is the actual problem with the partial coverage uniform flow, and the right side is the equivalent case with uniform flow. An equivalent reduced damping is found such that the equivalent uniform flow case has the same total power-in and the same total damping (Richardson, 2001). The total damping for the original problem and the equivalent problem can be written as

$$R_{total} = RL_{total} = R_{eff} L_{power-in} \rightarrow R_{eff} = R \cdot \frac{L_{total}}{L_{power-in}}$$

From this equation, we find that the effective damping per unit length for the equivalent case is modified by a length ratio. Thus, the equivalent reduced damping $S_{ge}$ can be written as

85

$$S_{ge} = S_g \cdot \frac{L_{total}}{L_{power-in}} = \frac{R\omega}{\rho_f V^2} \frac{L_{total}}{L_{power-in}} \qquad (5.46)$$

This method makes the results successfully fall into the curve of the $S_g$-RMS A/D

relationship as in Figure 5.1. That is, if a physically meaningful effective damping is

defined, the curve in Figure 5.1 will be still valid.
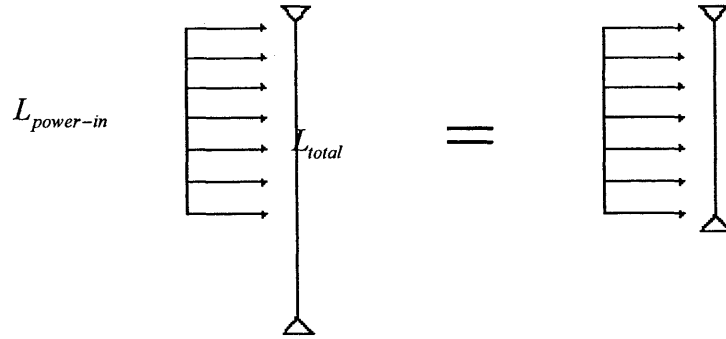


Figure 5.8. The partial coverage uniform flow and the equivalent uniform case with

equivalent reduced damping $S_{ge}$.

## 5.4 Time Evolution of Excitation Frequency and St Number

To determine the equivalent $S_g$ for the unsteady flow, we have to follow the outline

described in Section 5.1. The first point is to understand how the shedding frequency

changes with time under the top-end periodic motion. We can infer the shedding

frequency by the measured response frequency. Based on the data, we will propose a

constant Strouhal number model in this section regardless of the change of the inline

velocity.

The flow that causes VIV originates from the top-end periodic motion. For example, the

top-end vertical motion for the CVAR generates oscillations in the in-plane direction

everywhere along the riser. The flow due to the in-plane relative motion between the riser

and water has nearly sinusoidal flow velocities. The vortices are then shed and the VIV is

mainly in the transverse, or the out-of-plane, direction. The flow velocities are not only

time varying, but also spatially varying according to the configuration of the riser. Figure

5.9 shows a flow profile of the maximum flow velocities along the CVAR. For this plot, the top-end motion is sinusoidal with amplitude 3 ft and period 3 sec. This velocity profile was calculated by Passano of Marintek using the finite element program RIFLEX. The figure shows that a local minimum velocity close to the middle of the riser occurs around the junction between the buoyant pipe and the bare pipe. The flow oscillates everywhere along the riser with the same constant period as the top-end motion. The velocity amplitudes varies spatially according to the values in Figure 5.9. The phases of the velocities along the riser are not in general the same.
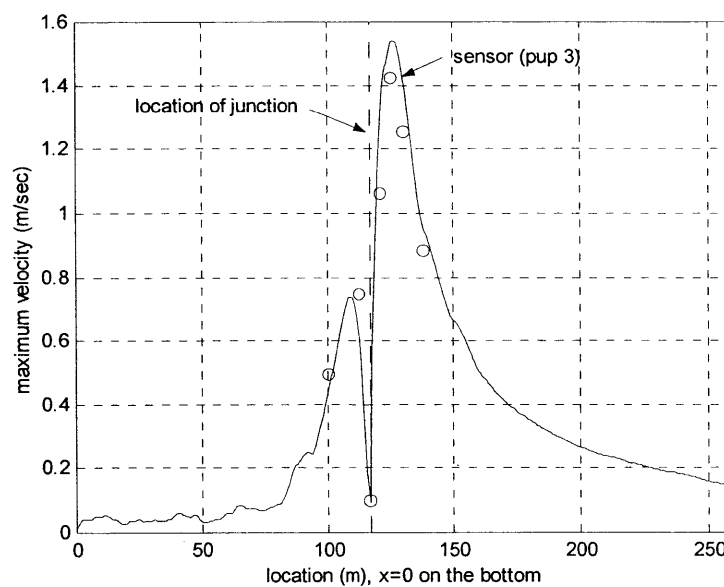


Figure 5.9. The comparison of the measurement (small circles) and the prediction of the inline maximum velocities along CVAR. Top-end motion: sinusoidal with A=3 ft and T=3 sec.

At any point of the riser, the sinusoidal flow velocities in the inline direction makes vortex patterns that are much more complex than in steady flow cases. A new parameter similar to the Strouhal number is needed to describe the relations between the shedding frequencies and the flow velocities. It is thus important to analyze the data in frequency domain for the transverse direction and link it to the inline direction velocity.

First the measured inline accelerations are used to infer the inline velocities. A typical time series of the inline acceleration is shown in Figure 5.10. A band-pass filter is applied to the data to obtain the sinusoidal component with the same period of the top-end motion. For a sinusoid with displacement amplitude $A$, the amplitude of the velocity is $A\omega$ and the amplitude of the acceleration is $A\omega^2$. Thus, from the filtered acceleration to get the inline velocity, we have to divide the acceleration amplitude by $\omega$. A set of 'measured' (inferred from the measured inline accelerations) inline velocities for one test is shown in Figure 5.10 by the small circles. Notice that it agrees very well with the prediction from the finite element method.
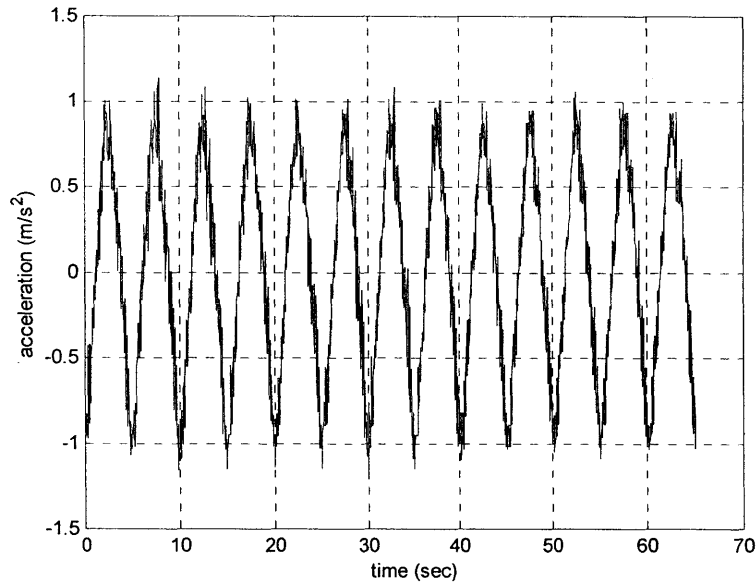


Figure 5.10. Acceleration time series in the in-plane direction for top-end amplitude 2 ft, top-end period 5 sec, at pup 3.

Spectral analysis is conducted for the transverse direction in order to know the VIV frequencies. A typical acceleration time series for the out-of-plane (transverse) direction is shown in Figure 5.11. The power spectral density of this acceleration time series is shown in Figure 5.12. The spectrum is calculated by Welch's averaged, modified periodogram method, with FFT length equal to 2048, and Hanning window length equal to 512. The total length of this set of data is 2601 and the sampling rate is 40 Hz. This figure shows the broadband frequency content found in the response, and the broadband

frequency content is due to the wide range of flow velocities for the sinusoidal inline motions.
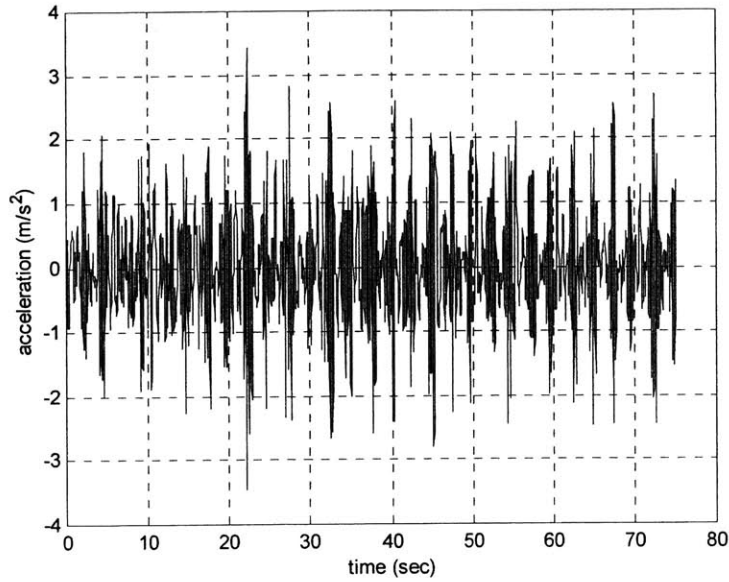


Figure 5.11. Acceleration time series in the out-of-plane direction for top-end amplitude 3 ft, top-end period 5 sec, at pup 3.
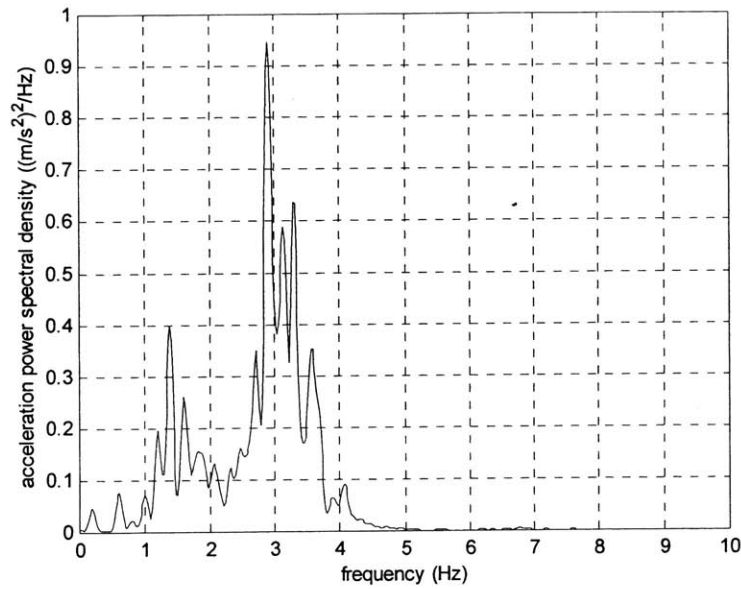


Figure 5.12. Acceleration power spectral density in the out-of-plane direction for top-end amplitude 3 ft, top-end period 5 sec, at pup 3.

To find the Strouhal number for this unsteady case, corresponding inline velocities and response frequencies have to be identified. One way to attack this problem is to watch the frequency variations in time. A zoom-in of Figure 5.11 is shown in Figure 5.13. Notice that at time around 22 sec, 24.5 sec, and 27 sec, the vibration frequencies are higher compared to those at other times. The time duration between any two peak frequencies is consistent with the top-end period 5 sec because in each period there are two maximum flow velocities. Time evolution of the frequency content is found by a short time spectral method, the Maximum Entropy Method. The data length to calculate the spectrum is 32, that is, 0.8 sec, the order of the autoregressive model is 10, the length for FFT is 2048, and we shift the window by 8 (0.2 sec) each time to calculate the next spectrum. Because the window length is 0.8 sec, it may average several cycles with different frequencies. The outcome for data in Figure 5.13 is shown in Figure 5.14, which clearly shows the periodic behavior of the frequency content. The period of the frequency evolution is about 2.5 seconds, or half of the top-end period.
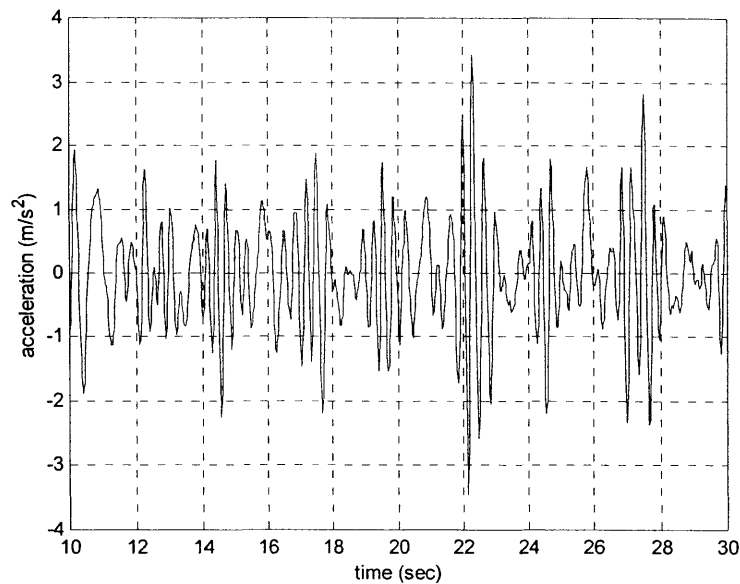


Figure 5.13. Zoom-in of acceleration time series in the out-of-plane direction for top-end amplitude 3 ft, top-end period 5 sec, at pup 3.

90

Figure 5.14. Time evolution of the frequency contents for the out-of-plane acceleration, top-end amplitude 3 ft, top-end period 5 sec, at pup 3.

We estimate the Strouhal number by considering the velocity amplitude in pup 3 and the maximum response frequency there. Pup 3 is the location closest to the maximum of the velocity profile along the CVAR riser (see Figure 5.10), so it is the major VIV power-in region. As an example, we examine the case when the top-end amplitude is 3 ft and the period is 5 sec. The inline velocity amplitude for pup 3 is 0.93 m/s (normal to the riser axis), and the maximum response frequency, as shown in Figure 5.14, is about 4 Hz. The outer diameter at this location is 0.0381 m. Thus, we get

$$St = \frac{fD}{V} = \frac{4 \times 0.0381}{0.93} = 0.164. \tag{5.47}$$

The same procedure can be used to obtain the Strouhal number for different patterns of top-end excitation. For all the CVAR cases, St is in the range from 0.16 to 0.17 using the above procedure, so we assign St=0.165 for all the tests. We also make the assumption that the Strouhal number is always constant while the inline velocity is varying with time. That is, the shedding frequency follows the constant Strouhal number relationship all the time, as

$$St = \frac{f_s(t)D}{V(t)}. \tag{5.48}$$

91

Therefore, the shedding frequency is varying as a sinusoid in the same way as the velocity. The periodic pattern can be seen in Figure 5.14, although sometimes the frequency content does not follow exactly the sinusoidal velocity at this pup location. Unexpected frequencies may come from the excitation of other locations.

Based on the assumption that the shedding frequency is proportional to the local velocity, an example of the inline velocity and the shedding frequency is plotted in Figure 5.15. The ratio between the values of the two curves is governed by the constant St number. Figure 5.16 shows the time evolution of the frequency content as in Figure 5.14, but with the addition of a predicted curve obtained from the constant Strouhal number relationship based on the same windowing and sampling as the real data. The good agreement supports the constant St assumption. The constant St number relationship implies that the distance between any two consecutive vortices is constant. In Figure 5.17, the distance $L$ for a steady current case can be written as

$$L = V \frac{T_s}{2} = \frac{V}{2f_s},$$
(5.49)

where $T_s$ is the shedding period of the vortices. A shed vortex travels downstream with the current velocity $V$, and the next vortex is shed on the opposite side after $\frac{T_s}{2}$. Notice that $St = \frac{f_s D}{V}$, so we have

$$L = \frac{D}{2St}.$$
(5.50)

This relationship is valid for any current velocity, so the constant St assumption does imply a constant distance between consecutive shedding vortices.

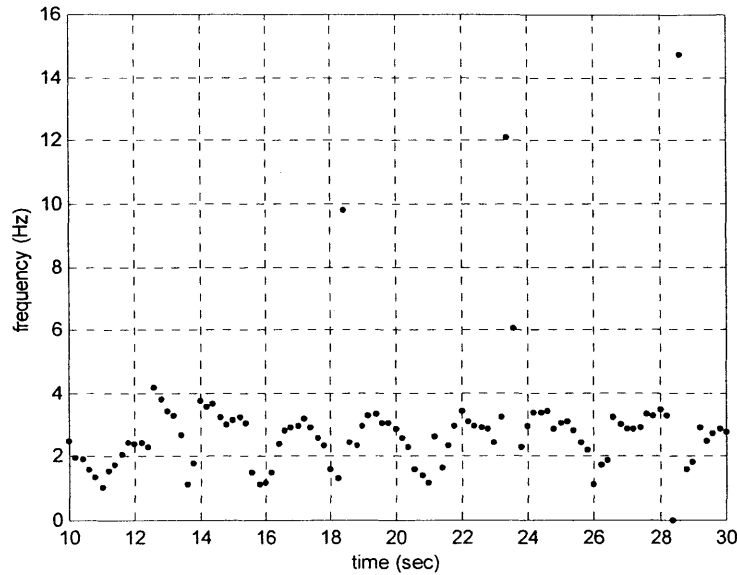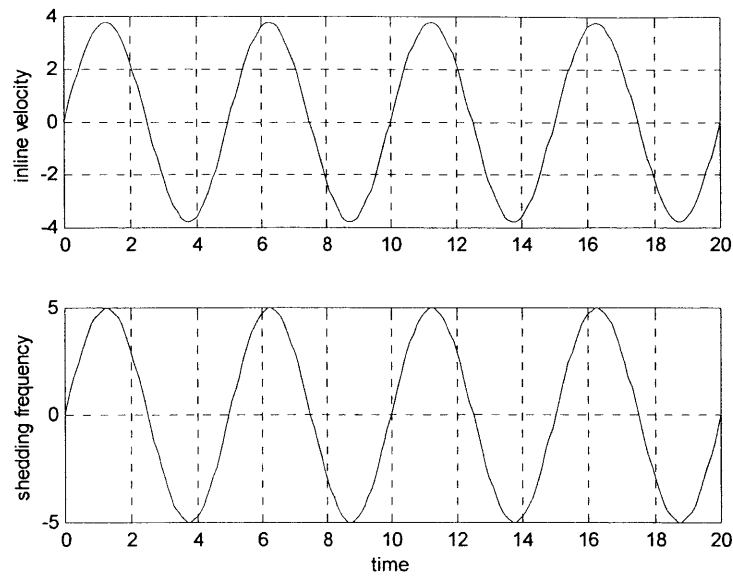Figure 5.15. The inline velocity and the shedding frequency for a constant St number.
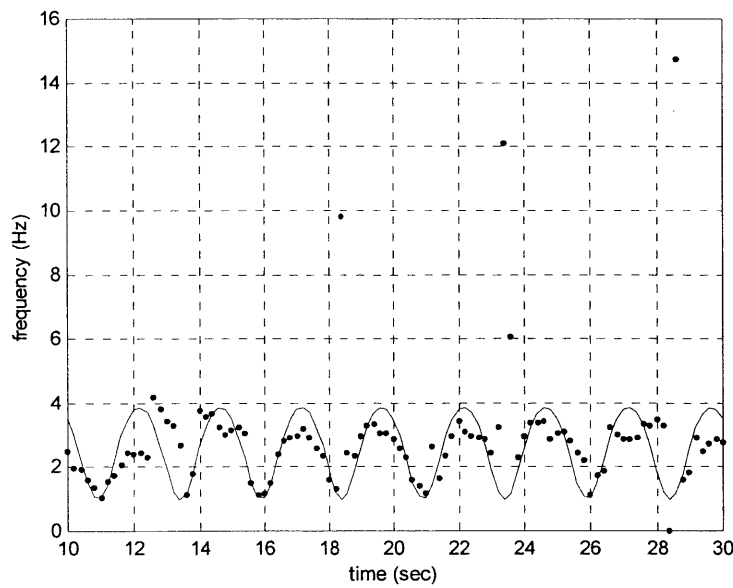


Figure 5.16. Time evolution of the frequency contents for the out-of-plane acceleration, top-end amplitude 3 ft, top-end period 5 sec, at pup 3. The solid line is obtained from the moving average of the constant St model with the same window length as the MEM calculations.
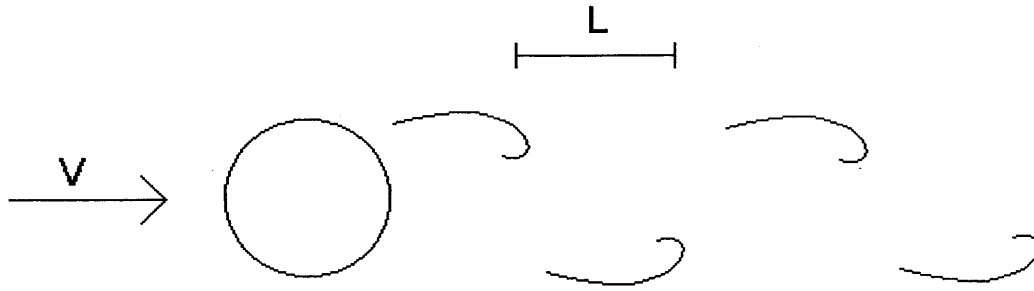
Figure 5.17. Vortex shedding under a steady current with velocity $V$. The distance between vortices is $L$.

## 5.5 Effect of KC Number on the Frequency Contents

The KC number is defined as $\dfrac{2\pi A}{D}$, where $A$ is the amplitude of a sinusoidal motion. In our case, this motion is that of the riser in the inline direction. When the KC number approaches infinity, the relative motion between the riser and water does not reverse direction, and it can be regarded as a steady current case with flow moving toward one direction only. The KC number is also a factor of how many vortex pairs are shed during one cycle of the inline riser motion. As described in the last section, the distance between two successive vortices is constant for a constant St. The larger the KC number, the longer the traveling distance per stroke, and the more vortices are shed during one stroke. We can calculate quantitatively how many shedding cycles there are in an inline stroke before reversing the inline velocity direction. Assuming the inline velocity is sinusoidal, it can be written as

$$V = V_0 \sin \Omega t,$$

where $V_0$ is the velocity amplitude, and $\Omega$ is the inline frequency, as the frequency for the sinusoidal velocity in Figure 5.15. $V_0$ is actually $A\Omega$ if we express it with the displacement amplitude. Thus, we can also write the KC number as

$$KC = \frac{2\pi V_0}{\Omega D}.$$

With the constant St number and the St number relationship

$$St = \frac{f_s D}{V} = \frac{\omega_s D}{2\pi V},$$

we can write the shedding frequency as

$$\omega_s = \frac{2\pi St V_0}{D} \sin \Omega t. \qquad (5.51)$$

One shedding cycle (2 vortices) takes time $t'$ such that

$$\int_0^{t'} \omega_s(\tau) d\tau = 2\pi. \qquad (5.52)$$

The time for an inline stroke is a half period, which is

$$t = \frac{\pi}{\Omega}.$$

To determine how many shedding cycles per stroke, we plug this time into the left side integral in Equation 5.51 and divide it by $2\pi$. Thus,

$$N = \frac{\int_0^{\frac{\pi}{\Omega}} \frac{2\pi St V_0}{D} \sin \Omega \tau d\tau}{2\pi} = \frac{St V_0}{D\Omega} \left(-\cos \Omega \tau\right)\Big|_0^{\pi/\Omega}$$

$$= \frac{2St V_0}{\Omega D} = \frac{KC \cdot St}{\pi}. \qquad (5.53)$$

This equation represents a compact and important relationship. The number of vortices shed per inline period is governed by the product of KC and St numbers. For example, the smallest top-end excitation amplitude for the CVAR test, 0.5 ft, corresponds to a KC number (with diameter 0.125 ft)

$$KC_{0.5} = \frac{2\pi \cdot 0.5}{0.125} = 8\pi \approx 25.$$

This is the KC number at the location where amplitude is 0.5 ft. In other locations along the riser the KC number is different due to different inline amplitudes. For the above KC number, and the average St number 0.165, we get

$$N = \frac{8\pi \cdot 0.165}{\pi} = 1.32.$$

That is, there are only fewer than 2 shedding cycles during one stroke. A larger KC number will tend to have more vortices shed during one stroke and more sustainable vortex patterns than a smaller KC number.

The spectral density functions for different KC numbers are shown in Figure 5.17. From Figure 5.10, we know the velocity amplitude at pup 3, around 1.53 m/s. The KC number can be estimated from this velocity amplitude, and similarly the KC numbers for other amplitudes can be estimated. The KC numbers for amplitudes 0.5, 2, and 3 ft are 20, 80, and 120, respectively. Notice that as the KC number gets larger, the response spectrum has higher frequency content. This relationship is consistent with what we described above: the larger the KC number, the more shed vortices per stroke. The spectrum spreads out and centers at higher frequency for the larger KC number, as shown in the panel for the larger top-end amplitude in Figure 5.17.
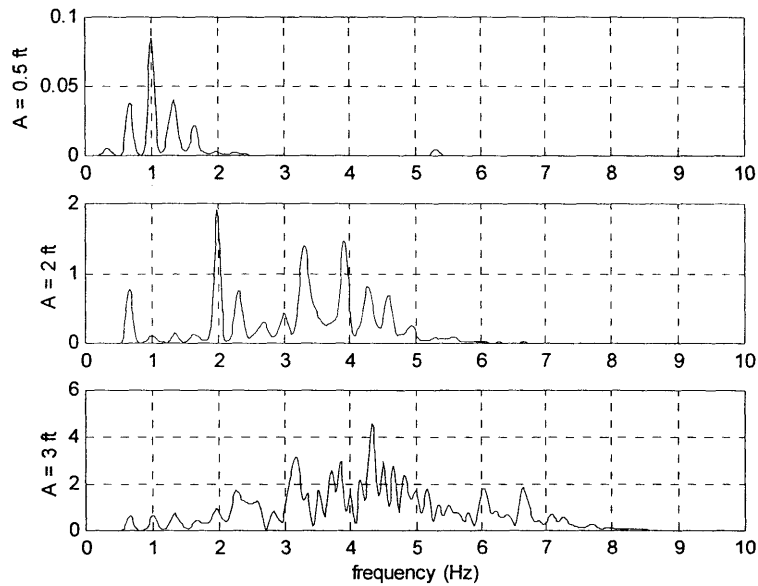


Figure 5.17. The spectral density functions for cross-flow acceleration at three different top-end amplitudes, i.e., different KC numbers. The excitation period is 3 sec. The measurements are at pup 3. The KC numbers at this location are around 20, 80, and 120 for the three different amplitudes.

Another feature notable in Figure 5.17 is that for a smaller KC number (the case of A=0.5 ft), the spectrum has spikes only at the multiples of the excitation frequency (1/3 Hz). In contrast, for a larger KC number (the case of A=3 ft), the spectrum covers a wide range of frequency without clear spikes at the multiples of the excitation frequency. An explanation for this is that when the KC number is small, for example, 20 to 30, the

vortices generated per stroke are so few that their number is discretely governed by the KC number. That is, the timing of vortex generation is shifted from the Strouhal relationship to the closest multiple of the excitation frequency. The KC number can be used as an indicator to distinguish between the behavior dominated by the excitation frequency and the behavior dominated by the Strouhal frequency. In this thesis we are concerned primarily with behavior associated with larger KC numbers in which the VIV frequency is governed by a Strouhal number.

## 5.6 Spring-mounted Cylinder in Unsteady Flow

With the proposed model of the shedding frequency, we will examine an introductory problem to prepare for a more complicated one. A spring-mounted rigid cylinder, as shown in Figure 5.5, is under unsteady flow with sinusoidally changing inline velocities. Likewise, the shedding frequencies also change sinusoidally. The governing equation, with the constant St assumption, can be written as

$$M\frac{\partial^2 y}{\partial t^2} + R\frac{\partial y}{\partial t} + Ky = \frac{1}{2}\rho_f V(t)^2 DC_L \cos(\int_0^t 2\pi f_s(\tau)d\tau), \qquad (5.54)$$

where

$$V(t) = A\Omega\sin\Omega t,$$
$$f_s(t) = \frac{StV}{D} = \frac{StA\Omega}{D}\sin\Omega t. \qquad (5.55)$$

The frequency $\Omega$ (in radians/sec) is the frequency of the inline motion, and $A$ is the amplitude of the inline displacement. The shedding frequencies vary with time, so we have to use integration to obtain the phase of the lift force excitation. The maximum possible shedding frequency is $f_{s0} = \frac{StA\Omega}{D}$. The natural frequency of the system is again

$\omega_n = \sqrt{\frac{K}{M}}$ (in radians/sec). In the case that $\omega_n < 2\pi f_{s0}$, the shedding frequency will be sometimes at the natural frequency, corresponding to a period of time at resonance. Also, due to the reduced velocity bandwidth, a shedding frequency close to a natural frequency may lock-in to the natural frequency. Thus, for a certain interval of time the system will be at resonance in a quasi-steady sense. The excitation at this duration of time contributes

most to the response at the resonant frequency. An effective way to simplify this unsteady vibration problem is to find an approximately equivalent steady problem.

In order to estimate how long the shedding frequency remains within a certain frequency interval, we have to obtain the probability density function for Equation 5.55. With the knowledge of the probability density function for a sine function, we can write the probability density function for Equation 5.55 as

$$p(f) = \frac{2}{\pi\sqrt{f_{s0}^2 - f^2}},$$
(5.56)

where $f$ is the frequency we are interested in. Figure 5.18 shows the probability density functions for inline amplitudes 1 ft and 3 ft, both with period 5 sec. The St number used is 0.165 and the diameter of the cylinder is 0.125 ft. Notice that for different inline amplitudes and periods, the term $f_{s0}$ will be different and thus the probability density function will be wider or narrower in frequency range. This probability density function provides the probability of time the shedding frequency spends within a frequency $\Delta f$. For example, in the case of amplitude 3 ft, the frequency spends more time around frequency 4 Hz than around 3 Hz. The longer the frequency stays at one frequency, the more the energy at that frequency is able to flow into the system, and the greater the response of the riser at that frequency.

Figure 5.18. The probability density function for sinusoidal frequencies, with amplitudes 1 and 3 ft, period 5 sec.

We now use the probability density function to solve the problem for the spring-mounted cylinder under unsteady flow. Suppose the inline amplitude is 3 ft and the period is 5 sec, and the natural frequency of the system is 4 Hz. Considering the lock-in bandwidth, we let the resonant frequency interval be ±10% of the natural frequency. That is, the frequency interval is from 3.6 Hz to 4.4 Hz. The probability density function and the interval are shown in Figure 5.19. The area below the curve and inside the frequency interval is the duty cycle the excitation spends on the resonant frequency interval. That is, only a portion of the total time can be regarded as contributing to the resonance. This area (probability) can be calculated as

$$\Pr(f_a < f < f_b) = \int_{f_a}^{f_b} p(f) df = \frac{1}{\pi} \tan^{-1}\left(\frac{f}{f_{s0}^2 - f^2}\right)\Big|_{f_a}^{f_b}, \qquad (5.57)$$

where $f_a$ and $f_b$ are the lower and the upper bounds of the frequency interval. This probability represents the ratio of the duty cycle to the total cycle, written as $\dfrac{T_{power-in}}{T_{total}}$. An effective way to treat this unsteady excitation is to pack all the excitation at the power-in time intervals into a smaller spatial region which has the excitation all the time. That is,

99

we approximately convert an unsteady excitation problem into a steady flow problem but with a smaller local excitation region. For the problem stated in Equation 5.54, the equivalent power-in length becomes the duty cycle ratio $\dfrac{T_{power-in}}{T_{total}}$ times the total length. The problem turns into the partial excitation problem stated at the end of Section 5.3, and we can write the equivalent reduced damping $S_{ge}$ as

$$S_{ge} = S_g \frac{T_{total}}{T_{power-in}}. \tag{5.58}$$

That is, we can obtain an equivalent reduced damping for a spring-mounted cylinder under unsteady flow. The concepts of using the probability as the duty cycle ratio in time and of obtaining an equivalent reduced damping will now be extended to the problem for a flexible cylinder under non-uniform, unsteady flow.
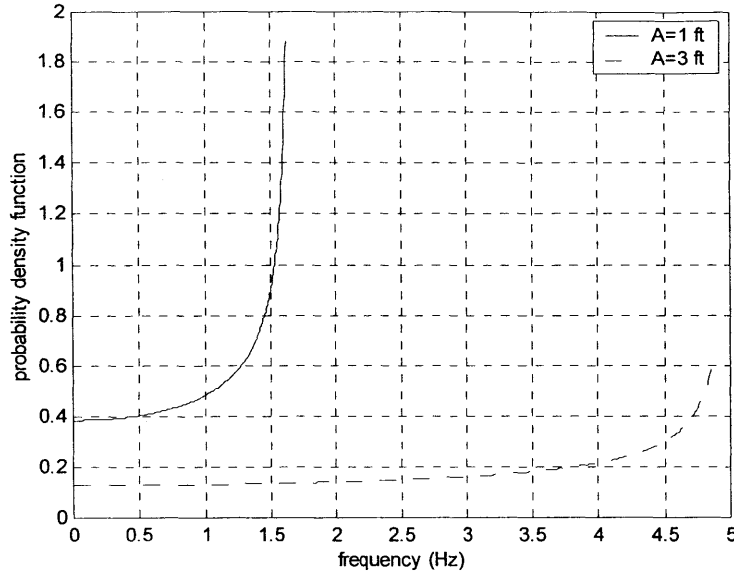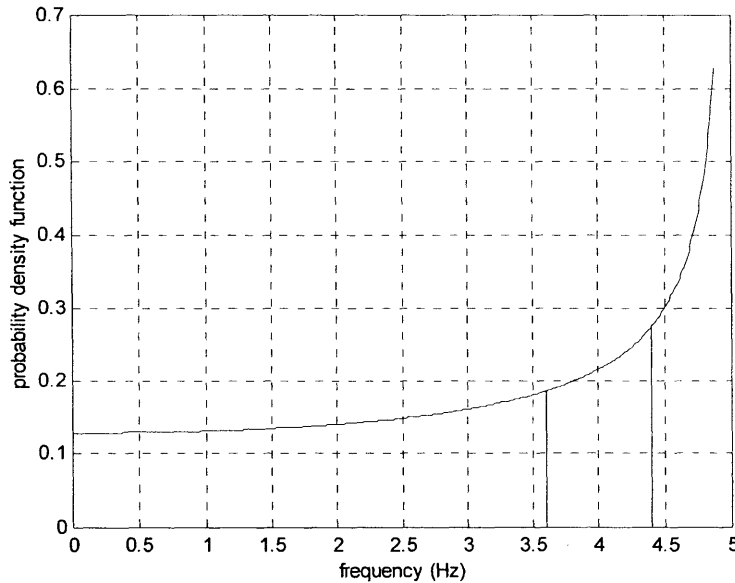


Figure 5.19. The probability density function for sinusoidal frequencies, with amplitudes 3 ft, period 5 sec. A frequency interval is shown around the natural frequency of the system (4 Hz ±10%).

## 5.7 Equivalent Reduced Damping $S_g$ for Unsteady Flow

The ultimate goal is to use $S_g$ to link the excitation and the response for a long flexible cylinder under top-end periodic motions. We seek to determine an equivalent reduced

100

damping for this unsteady flow problem. The principal idea in solving this problem is shown in Figure 5.20. A flow velocity profile of CVAR under the top-end periodic motion is illustrated in the upper left panel. For any small spatial section $\Delta x$ of the riser, there is a local sinusoidal inline velocity. The local shedding frequency is also sinusoidal due to the constant St assumption. The probability density function of the local shedding frequency can be obtained as shown in the lower right panel of Figure 5.20. For a specific frequency interval, we can calculate the probability, i.e., the duty cycle for that frequency interval at the specific location. This step is the same as the one shown in the previous section, except that here the probability density function is calculated only for the specific $\Delta x$ location. As shown in Figure 5.18, the probability density functions for different amplitudes are different. Therefore, we have to divide the whole riser into many sections, each $\Delta x$ in length. Within each section the maximum inline velocity is evaluated. Then we obtain the probability density function of frequency for each section, as shown in Figure 5.20. For a specific frequency interval, the total excitation may come from many spatial sections. For each contributing section, the associated duty cycle is evaluated according to the local probability density function. For each frequency interval, the sum of the duty cycles at all contributing sections is the total duty cycle. If this number exceeds 1.0, for example 3.7, then this means an equivalent excitation has 100% duty cycle (i.e., steady flow) over a length equal to 3.7 $\Delta x$ .
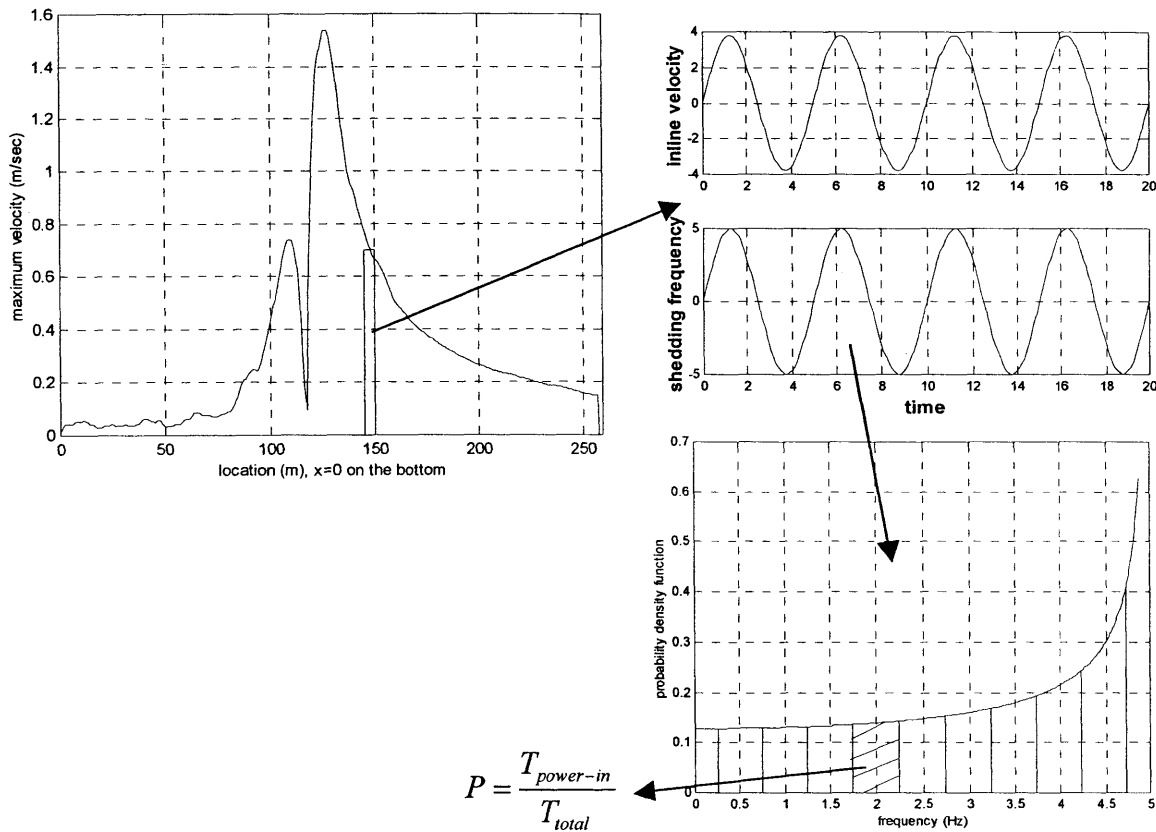
Figure 5.20. The mapping from the unsteady velocity profile to the probability density function of excitation frequency.

We propose a simple but conservative model for accumulating the effects of all distributed excitation along the riser. As in the spring mounted cylinder example, the duty cycle for a particular frequency interval at a specific spatial section is equivalent to a 100% duty cycle on a shorter section whose length is given by $\Delta x \cdot$ duty cycle=

$\dfrac{T_{power-in}}{T_{total}} \Delta x$ . The fraction of the excitation region at the frequency is thus the duty cycle

ratio $\dfrac{T_{power-in}}{T_{total}}$ . If we then add up all such sections, we obtain the equivalent length

$L_{power-in}$ of cylinder which has steady excitation at the chosen frequency interval. Therefore, the equivalent steady excitation for this specific frequency at this section

covers only $\dfrac{L_{power-in}}{L_{total}}$ of the total riser length. A very conservative assumption has been

invoked. For a specific frequency, the excitation contributed from all the spatial sections has been accumulated as if they were in the same phase. This assumption is very conservative because any two out-of-phase excitation forces will partially cancel each other, causing smaller system response. We thus pack all the equivalent steady excitation into one equivalent section, with a length equal to

$$L_{power-in}(f_j) = \Delta x \sum_{\Delta x_i} \frac{T_{power-in}(f_j)}{T_{total}} \qquad (5.59)$$

This equivalent length will be frequency dependent because the probabilities of different frequency intervals are different. Following the procedure as in the partial flow problem described in Section 5.3, we know

$$R_{total} = RL_{total} = R_{eff} L_{power-in} \qquad (5.60)$$

or we can obtain the equivalent damping coefficient as:

$$R_{eff}(f_j) = R \frac{L_{total}}{L_{power-in}(f_j)} . \qquad (5.61)$$

Two points remain to be clarified. First, we have not specified how to choose the frequency intervals as in the lower right panel of Figure 5.20. Second, we have to determine the damping coefficient $R$ used in Equation 5.61. We will discuss how to partition the frequency content first.

For linear vibration, the steady state response of the system at a certain frequency is caused by excitation at that frequency. Thus, our purpose in frequency partitioning here is to separate the contributions from different frequencies, so that we are able to use a quasi-steady model for a single frequency. In the previous section, we chose the upper bound

and the lower bound of the frequency interval by considering the lock-in bandwidth of VIV response. In the problem encountered here, the mode number is very high and thus the modal density is high. Therefore, we are not able to distinguish two adjacent modes, and the selection of the frequency bounds described in the previous section is not useful. As observed in the spectra of the response from the CVAR test as in Figure 5.17, the spectra tend to have spikes at the multiples of the excitation frequency. This phenomenon is because when the inline velocity is periodic, the vortices tend to organize themselves so that an integer number of vortices are shed during one stroke (Blevins, 1990). Based on this phenomenon, we propose to define the width of each frequency interval as $\frac{1}{T}$, where $T$ is the top-end period. This method is equivalent to considering how many vortices are shed per top-end cycle as a parameter. We will show that with this choice of $\Delta f$, we can compute damage per vortex shed. With this frequency partitioning, we then compute the duty cycle for each frequency interval. The equivalent reduced damping $S_{ge}$ for the unsteady VIV can now be written as:

$$S_{ge} = \frac{R_{eff}\omega}{\rho_f V^2} = \frac{R\omega}{\rho_f V^2} \frac{L_{total}}{L_{power-in}}, \qquad (5.62)$$

where $\omega$ is the frequency (in radians/sec) we are interested in, $V$ is the velocity associated with this frequency by the Strouhal relationship, and $L_{power-in}$ is the total equivalent length with 100% duty cycle.

For a steel riser, the damping coefficient $R$ in Equation 5.60 is mainly contributed by hydrodynamic damping. Because we are mostly interested in the response from high flow velocities, the damping outside of the power-in region corresponds to lower flow velocities. Thus, we apply the low reduced velocity damping model used in SHEAR7 to our problem (Venugopal, 1996). For a preliminary calculation, we do not include the still water term of the model. The damping coefficient per unit length can then be written as:

$$R = C_{rl}\rho_f D V_a, \qquad (5.63)$$

where $C_{rl}$ is an empirical coefficient and $V_a$ is the velocity associated with the source of damping. The coefficient $C_{rl}$ is set to 0.18 for SHEAR7, and we will use this value in our

104

unsteady case. In our problem, flow is non-uniform and unsteady, so the real damping may be time varying. Because the model we propose has a very small power-in region (only each spatial section as shown in the upper left panel of Figure 5.20), we can use the average velocity over space and time for the damping calculation. In the CVAR case, if we average the maximum inline velocities in space and then multiply the answer by $\dfrac{2}{\pi}$ (the time average of a sinusoid), we obtain a value around 13.6% of the peak inline velocity along the riser. That is, the average velocity, $V_a$, for damping computation purposes is about 13.6% of the maximum velocity. Or, the average velocity can be expressed as

$$V_a = r_a V_{\max},\qquad (5.64)$$

where $r_a$ is the fraction of peak velocity, which will be different for different riser configurations. $V_{\max}$ is the maximum inline velocity along the riser. Thus, we are able to obtain the damping coefficient $R$ by Equations 5.63 and 5.64.

If we further use the identity $\omega = 2\pi f$ and the relationship $V = \dfrac{fD}{St}$, the equivalent reduced damping $S_{ge}$ becomes

$$S_{ge} = \frac{C_{rl} D r_a V_{\max} \dfrac{L_{total}}{L_{power-in}} 2\pi f}{\dfrac{f^2 D^2}{St^2}} = 2\pi St^2 C_{rl} r_a \frac{L_{total}}{L_{power-in}} \frac{V_{\max}}{fD} = \frac{2\pi St^2 C_{rl} r_a}{f_{nd}} \frac{L_{total}}{L_{power-in}}, (5.65)$$

where the definition of the non-dimensional frequency $f_{nd} = \dfrac{fD}{V_{\max}}$ shown in Section 2.1 is used. Notice that in this expression of the equivalent reduced damping, $r_a$, the ratio of the average velocity to $V_{\max}$ is a function of the riser configuration. The factor $\dfrac{L_{total}}{L_{power-in}}$ is a function of both the configuration and the top-end excitation. That is, with the knowledge of the riser configuration and the top-end periodic excitation, we are able to calculate the equivalent reduced damping for any specific frequency we are interested in.

105

## 5.8 The $S_g$-RMS A/D Relationship for Unsteady VIV

In this section we will verify that the $S_g$-RMS A/D relationship for steady flow as shown in Figure 5.1 has an equivalent result for measured response in unsteady flow in terms of $S_{ge}$. In order to reach this goal, we have to obtain the measured RMS A/D for the same frequency intervals as used in the frequency partitioning for $S_{ge}$.

With a response spectrum, the RMS values for a frequency interval can be estimated by

$$RMS = \sqrt{\int_{f_1}^{f_2} p \, df}, \qquad (5.66)$$

where $p$ is the spectrum, and $f_1$, $f_2$ are the lower and upper bounds of the frequency interval. In the discrete domain, we just substitute the integration operator by a summation sign. As shown in Figure 5.21, the spectrum is partitioned to several frequency intervals, according to the partitioning for calculating $S_{ge}$. The nominal frequency at each frequency interval is a multiple of the top-end frequency (0.2 Hz in this example). For each interval, the spectrum is summed up to obtain the mean square acceleration for that frequency range. The circles shown in the lower panel of Figure 5.21 represent the calculated mean square value for each frequency interval. The greater the area under the spectral curve in an interval, the higher the mean square acceleration for that interval.
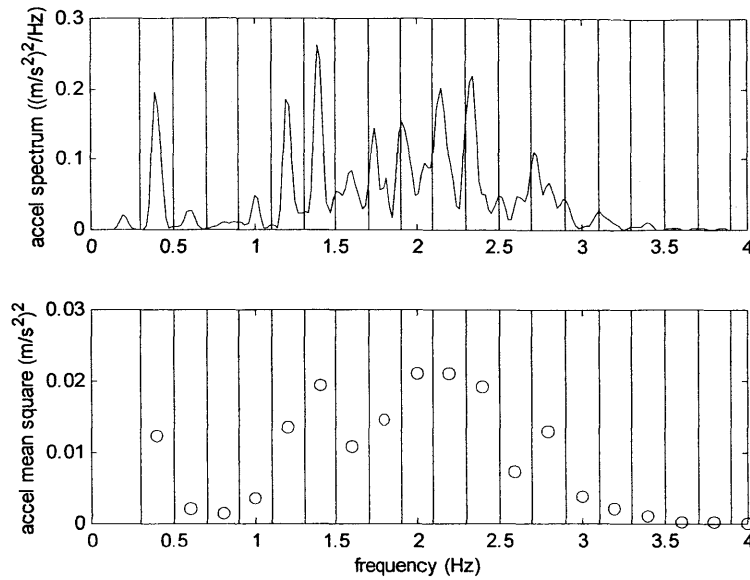
Figure 5.21. The frequency partitioning for the acceleration spectrum for CVAR, top-end amplitude 2 ft, top-end period 5 sec, pup 3. Each circle is the acceleration mean square for each frequency interval calculated from the measured spectrum.

To obtain the RMS displacement from the acceleration spectrum, we use the spectral relationship

$$S_A(\omega) = \omega^4 S_X(\omega), \tag{5.67}$$

where $\omega$ is the frequency in radians/sec that we are interested in, while $S_A(\omega)$ and $S_X(\omega)$ are the spectral density functions for the acceleration and the displacement, respectively. With this relationship, any acceleration spectrum can be converted to a displacement spectrum by dividing the acceleration spectrum by $\omega^4$. Figure 5.22 shows a pair of corresponding spectra for acceleration and displacement. As can be seen in the figure, the high frequency contents in the acceleration spectrum are suppressed due to the division of $\omega^4$, while the low frequency contents are amplified. The same frequency partitioning technique can be used for the displacement spectrum, and it yields the RMS displacements for different frequency intervals. The only difficulty in this technique is that for very low frequencies, small measurement noise will contribute to extremely large displacement spectral density (due to the division of very small $\omega^4$). Fortunately, we are only interested in the frequency ranges due to VIV, and these frequencies are not very

107

low. Thus, we just ignore the lower frequency intervals when calculating the RMS displacements. An example of the calculated RMS displacement is shown in Figure 5.23.
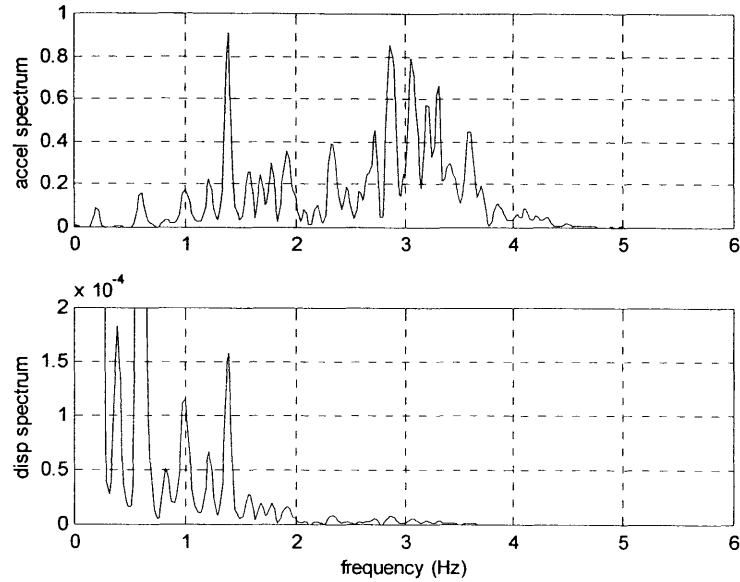


Figure 5.22. The acceleration spectrum ((m/s^2)^2/Hz) and the displacement spectrum (m^2/Hz) for CVAR, top-end amplitude 3 ft, top-end period 5 sec, pup 3.
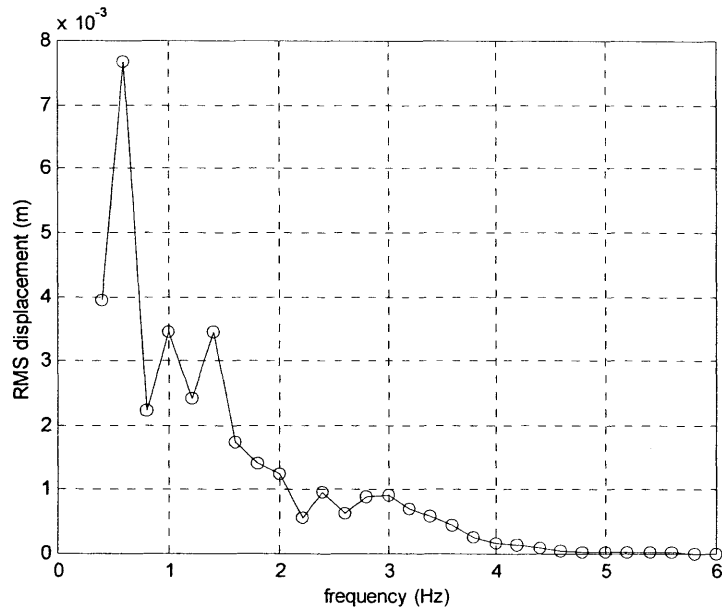


Figure 5.23. The RMS displacement of discrete frequency intervals obtained from the displacement spectrum for CVAR, top-end amplitude 3 ft, top-end period 5 sec, pup 3.

Now we are able to obtain the RMS displacement within each frequency interval for any top-end excitation. Each data point in Figure 5.23 has a corresponding $S_{ge}$ for the specific frequency interval. That is, we are able to mark a point in the $S_{ge}$-RMS A/D plot for each frequency interval under a certain top-end excitation at a specific pup. By this procedure, we can mark all the points for all the frequency intervals under all excitation patterns at all pups. Figure 5.24 demonstrates the results by marking all the data points in a plot. Every data point corresponds to the measurement of a sensor at each frequency interval for a combination of top-end amplitude and period. That is, the frequency partition technique breaks down the total response into components from different frequencies. Remarkably, all the data points fit very well with the relationship curve for the steady VIV problem. Thus, we have figured out a way to interpret the unsteady VIV response by introducing an equivalent reduced damping model for the unsteady flow.
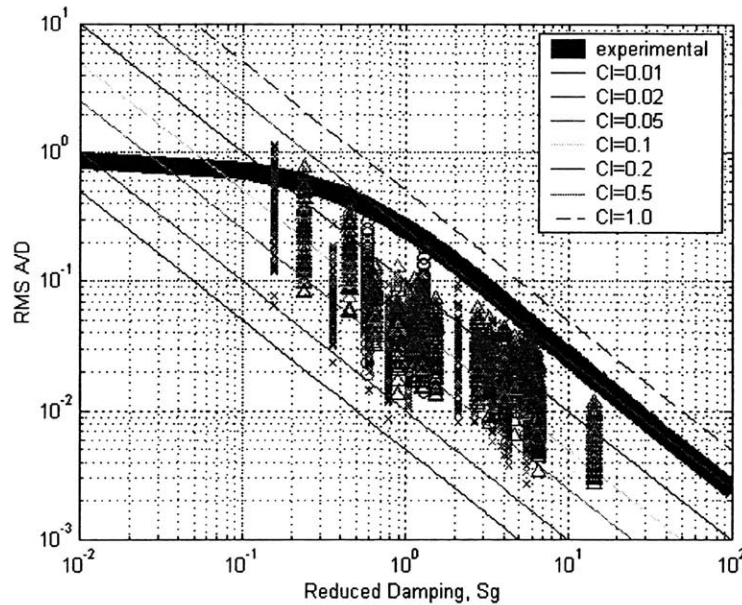


Figure 5.24. The relationship between the equivalent reduced damping $S_g$ and RMS A/D. The reduced damping is obtained from the CVAR unsteady flow profile, and the RMS displacements are from measurements with frequency partitioning. The data include all different combinations (period and amplitude) of top-end excitation, and

measurements from all pups. The very low values are from sensors far away from the location of $V_{max}$.

## 5.9 Non-dimensional Frequency

After being able to verify the usage of the equivalent reduced damping model, we would like to explore this problem in a dimensionless sense. We will introduce the importance of the non-dimensional frequency, and use it to explain the comparisons of response to different top-end excitations.

The non-dimensional frequency is defined as $f_{nd} = \dfrac{fD}{V_{max}}$. The frequency in the definition is the vibration frequency, which is caused by the shedding frequency forces. For a constant Strouhal number, $f_{nd}$ has a maximum value equal to St. Figure 5.25 shows the spectra for three different excitation frequencies with the same top-end amplitude. If we use the non-dimensional frequency in the abscissa (the spectra unit should be normalized accordingly), the rescaled spectra are shown in Figure 5.26. The spectra are rescaled by using the relationship

$$S_{xx}(f_{nd})df_{nd} = S_{xx}(f)df,$$

$$S_{xx}(f_{nd}) = \frac{df}{df_{nd}} S_{xx}(f).$$

The rescaled factor $\dfrac{df}{df_{nd}}$, which is equal to $\dfrac{V_{max}}{D}$, can be obtained from the definition of the non-dimensional frequency. The unit of the spectra is $(m/s^2)^2$ because of the normalization. Notice that when we use the non-dimensional frequency to represent the spectra, they are similar to each other. That is to say, the non-dimensional frequency content does not depend on the excitation frequency. The magnitudes of the spectra do differ for different excitation amplitudes and periods. We will discuss this difference later in terms of the displacement rather than the acceleration.
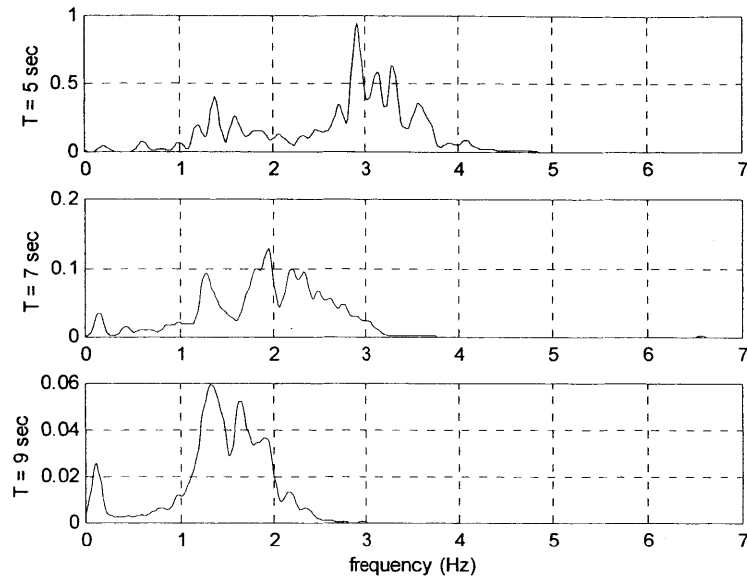
Figure 5.25. The acceleration spectra ((m/s^2)^2/Hz) of three different excitation periods for CVAR configuration. The top-end amplitude is 3 ft and the measurement is for the cross-flow pup 3.
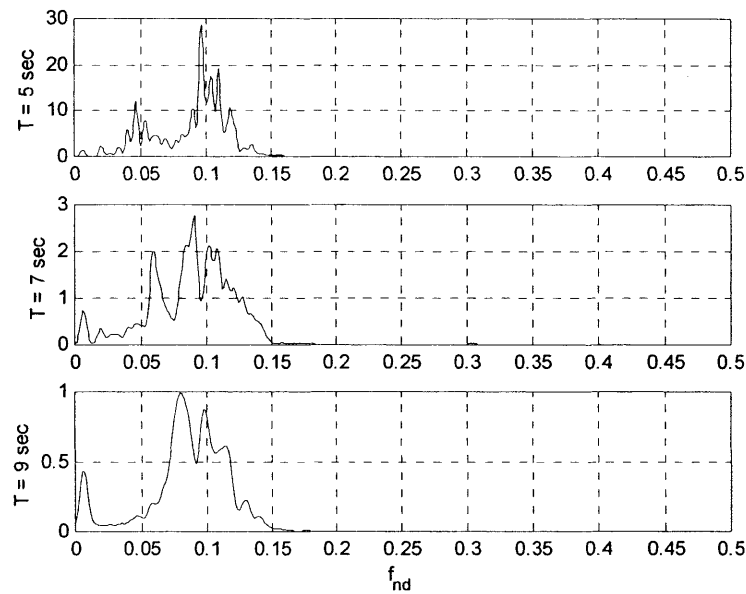


Figure 5.26. The acceleration spectra ((m/s^2)^2) of the three different excitation periods for CVAR configuration. The abscissa is expressed in terms of the non-dimensional frequency. The top-end amplitude is 3 ft and the measurement is for the cross-flow pup 3.

111

To further demonstrate the normalization with non-dimensional frequency, we randomly select three tests for CVAR with different amplitudes and different periods. The spectra with respect to the frequency are shown in Figure 5.27, and the spectra with respect to the non-dimensional frequency are illustrated in Figure 5.28. Again, the spectra in Figure 5.28 all center around the same range of $f_{nd}$. This result is remarkable and it confirms that the 'average' St number does not vary too much in different tests.



Figure 5.27. The acceleration spectra ((m/s^2)^2/Hz) of three randomly selected different excitation periods and amplitudes for the CVAR configuration. The measurement is for the cross-flow direction of pup 3.
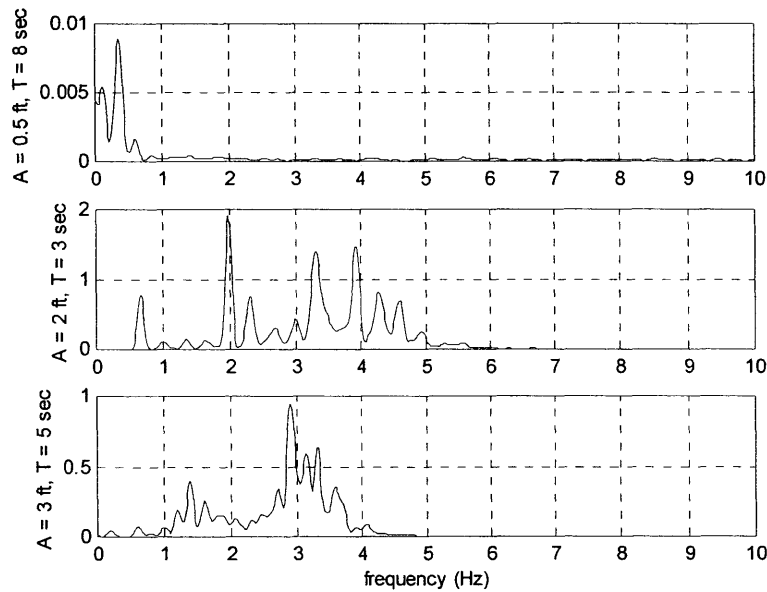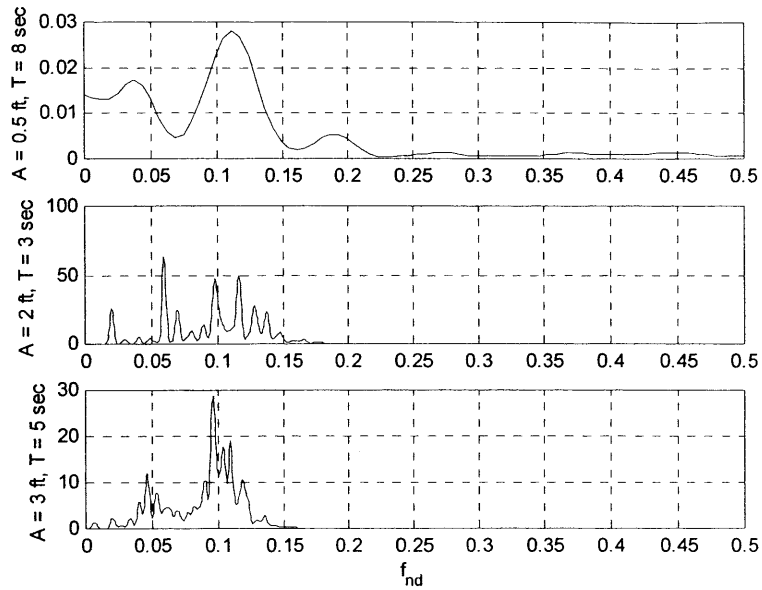
Figure 5.28. The acceleration spectra ((m/s^2)^2) of three randomly selected different excitation periods and amplitudes for CVAR configuration. The abscissa is the non-dimensional frequency. The measurement is for the cross-flow direction of pup 3.

Next we discuss the effects of the non-dimensional frequency on the power-in length

ratio $\dfrac{L_{total}}{L_{power-in}}$ . This ratio is a function of the riser configuration and the top-end

excitation. If the riser configuration is fixed, the velocity profile will have approximately similar spatial distributions even though the top-end periods or amplitudes change. The ratio of the velocities between two excitation patterns is approximately constant. Consider the probability density functions at the same location of two cases with different top-end amplitudes and periods. The probability density functions are shown in Figure 5.29. The left panel is for the amplitude 3 ft, the period 5 sec; the right panel is for the amplitude 2 ft, the period 8 sec. The frequency interval, 1/T, for the left panel is about 0.5 Hz, while it is about 0.21 Hz for the right panel. The functions are quite different, but if we integrate the areas under the curves for the shaded frequency intervals, the probabilities of the two cases will be the same. That is, the duty cycles for those specific frequency intervals are the same. A better approach to this problem is to use the non-dimensional frequency to plot the probability density function. This function is shown in

Figure 5.30. Because the abscissa is rescaled, the ordinate has also been rescaled. Using the non-dimensional frequency, the probability density function will always be the same regardless of the change of the top-end excitation. Furthermore, for the same riser configuration, if the probabilities (the duty cycle ratios) for two cases are the same, the length ratios for these two cases will be the same. The important outcome of this conclusion is that if we look at the same value of non-dimensional frequency, and if the partition width in terms of $\dfrac{\Delta f \cdot D}{V_{max}}$ is fixed, the ratio $\dfrac{L_{total}}{L_{power-in}}$ will be the same for different excitation cases.
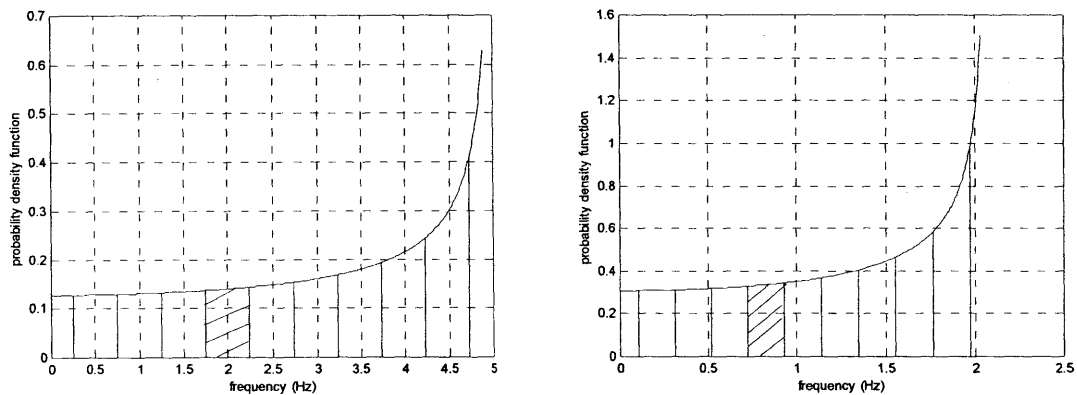


Figure 5.29. Two probability density functions of different top-end amplitudes and periods. The left panel is for amplitude 3 ft, period 5 sec; the right panel is for amplitude 2 ft, period 8 sec.

114
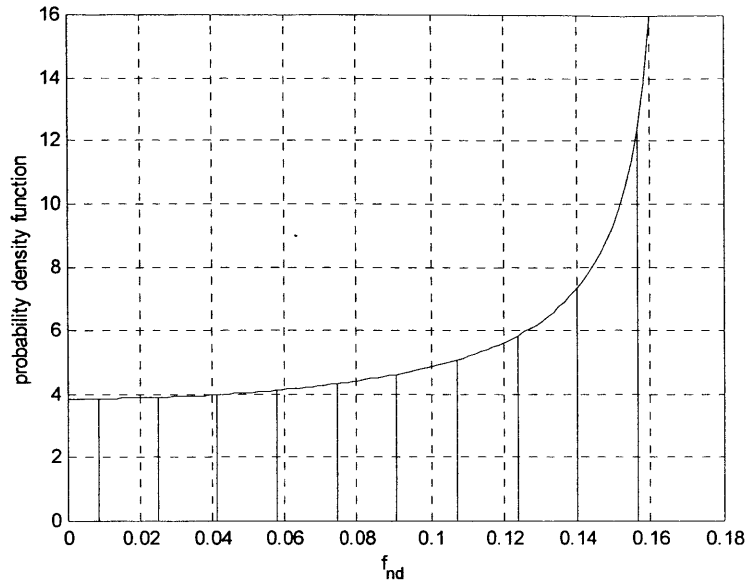
Figure 5.30. The probability density function for sinusoidal frequencies at a point, with $f_{nd}$ as the variable.

From Equation 5.66 for the equivalent reduced damping $S_{ge}$, we know that it is a function of $r_a$, $f_{nd}$ and $\dfrac{L_{total}}{L_{power-in}}$. The average velocity ratio $r_a$ is influenced by the configuration. Therefore, if we have the same configuration, the same $f_{nd}$ will yield the same $\dfrac{L_{total}}{L_{power-in}}$, and thus the same $S_{ge}$. The same $S_{ge}$ represents the same response amplitude. In brief, for the same riser configuration, the same $f_{nd}$ and the same $\dfrac{\Delta f \cdot D}{V_{max}}$, the RMS A/D will be the same regardless of the top-end excitation. Figure 5.31 demonstrates RMS A/D for three different top-end periods. Remarkably, the RMS A/D all fall into a very narrow band in the figure, indicating that the response amplitude at a certain frequency interval is only a function of the non-dimensional frequency, and not influenced by the top-end period.

115
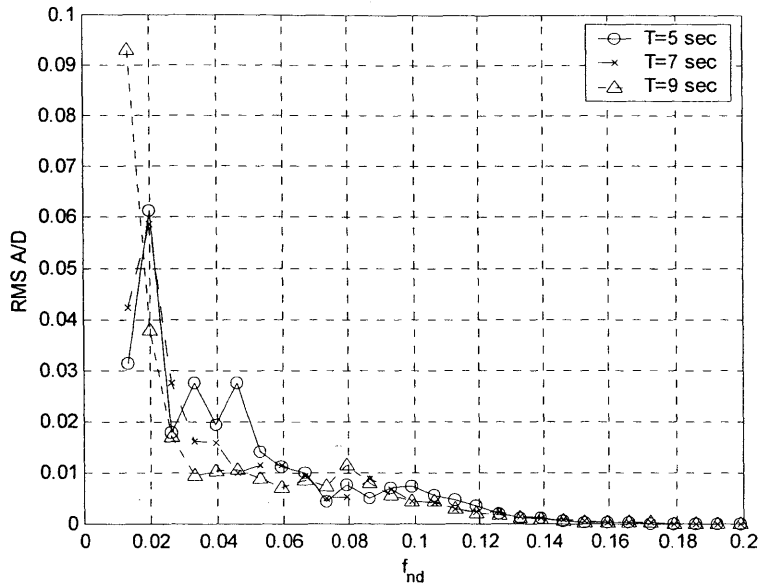
Figure 5.31. The RMS A/D from the calculation of partitioned frequency intervals. This is for CVAR tests: top-end amplitude 3 ft, top-end periods 5, 7, 9 sec, pup 3.

## 5.10 Fatigue Damage Rate Prediction

In terms of industrial needs, the most important aspect is to predict the fatigue damage rate. Though it is possible to calculate the RMS response of the simulated results, as demonstrated in Appendix 3, and then obtain the fatigue damage rate, we will illustrate a more practical method with the usage of the $S_g$ -RMS A/D relationship. That is, if we know $S_g$, we know the RMS A/D, and then we can predict the fatigue damage rate following the similar procedure introduced in SHEAR7.

Suppose a riser configuration is known, and the top-end periodic motion (e.g., the vessel motion) is also known. The inline flow velocities along the riser can be calculated by a sophisticated finite element program. With the velocity profile, we can obtain the shedding frequencies by the St relationship. A frequency partitioning technique is needed to further calculate $S_g$ for discretized frequency intervals. In the previous sections, we use the top-end frequency as the width of the frequency interval. The partitioning can also be carried out by the modal frequency if the modal density is not too high. After the

116

partitioning, we are able to obtain the probability of occurrence for each frequency interval at each location from Equation 5.58, $\Pr(f_a < f < f_b) = \dfrac{1}{\pi} \tan^{-1}\left(\dfrac{f}{f_{s0}^2 - f^2}\right)\Big|_{f_a}^{f_b}$.

The next step is to calculate the length ratio in Equation 5.61, $\dfrac{L_{total}}{L_{power-in}}$, for each

frequency interval, where $L_{power-in}(f_j) = \Delta x \sum\limits_{\Delta x_i} \dfrac{T_{power-in}(f_j)}{T_{total}}$. The duty cycle ratio $\dfrac{T_{power-in}}{T_{total}}$

is inferred from the probability just shown above. Finally, we obtain reduced damping $S_g$

for each frequency interval by Equation 5.66, $S_{ge} = \dfrac{2\pi St^2 C_{rl} r_a}{f_{nd}} \dfrac{L_{total}}{L_{power-in}}$. The coefficient

$C_{rl}$ is assigned 0.18 from the SHEAR7 model.

Now we have an equivalent $S_g$ for each frequency interval. We use the $S_g$-RMS A/D curve to infer the RMS A/D for each frequency interval. The quantity we need for the fatigue estimation is the RMS stress, or equivalently, the RMS curvature. For a wave, we know that the curvature is

$$y'' = -\gamma^2 A e^{i(\gamma x - \omega t)}, \tag{5.68}$$

where $\gamma$ is the wave number. Because we have already partitioned the frequency contents so that at each frequency interval the frequency can be regarded as a constant, and so can the wave number. We can then multiply the RMS A/D by the corresponding wave number for each frequency interval and obtain the RMS curvature. The RMS stress for each frequency interval is estimated as

$$S_{rms} = \dfrac{EDy''}{2\sqrt{2}}. \tag{5.69}$$

Next, we calculate the fatigue damage rate for each frequency interval by using the S-N curve expression for the Rayleigh distribution. The damage rate per year can be written as

$$D_n = \dfrac{\omega T}{2\pi C}(\sqrt{2}S_{rms})^b \Gamma(\dfrac{b+2}{2}), \tag{5.70}$$

117

where $\omega$ is the frequency of that interval, $T$ is the second per year (365*24*3600 sec), $b$ and $C$ follow the relationship

$$NS^b = C, \tag{5.71}$$

which is determined by the material properties, and $\Gamma$ is the Gamma function. Equation 5.71 illustrates a way to calculate the fatigue damage rate for each frequency interval. To obtain the total fatigue damage rate for the riser under a specified unsteady flow, we sum up the damage rate of all frequency intervals and get

$$D = \sum D_n. \tag{5.72}$$

That is, through the procedure described above, we are finally able to estimate the fatigue damage rate with only the knowledge of the material properties, the riser configurations, and the specifications of the top-end excitation. Considering the complexity of the unsteady VIV, this is a practical and conservative method for predicting the damage rate. This procedure has been used for the CVAR riser for all the available combinations of the top-end excitation amplitudes and periods, and the estimations of the fatigue damage rates are shown in Figure 5.32. As can be seen in the figure, when the top-end amplitude gets larger or the top-end period gets shorter, the fatigue damage gets worse. This result is as expected. When the top-end amplitude is fixed while the top-end periods vary, we know that $S_g$ is the same for the same $f_{nd}$. In order to have the same $f_{nd}$, the shorter top-end period requires higher response frequency, and vice versa, because of the constant Strouhal relationship. The same $S_g$ gives the same RMS A/D, but the RMS stresses are different. According to Equations 5.69 and 5.70, the RMS stress is proportional to $\gamma^2$. That is, for a beam, it is proportional to $\omega$, while for a string, it is proportional to $\omega^2$. For a tension beam the RMS stress will be proportional to between the first power and the second power of the frequency. Equation 5.71 shows that the damage rate is proportional to $\omega S_{rms}{}^b$. For the CVAR riser, $b$ is about 4.3. Therefore, for different top-end periods with the fixed top-end amplitude, the fatigue damage rate is inversely proportional to between 5.3th (for a beam) and 9.6th (for a string) power of the top-end period. The relationship shown in Figure 5.32 falls in between these two extreme cases (about 6.3th power by curve fitting). We also know that when the top-end period is

fixed while the top-end amplitudes differ, $S_g$ is the same for the same $f_{nd}$ if the width of

the frequency interval is properly chosen as in Figure 5.29. The same value of $f_{nd}$

requires a higher frequency for a larger top-end amplitude, and vice versa. Similar to the

case of a fixed amplitude and varying periods, the fatigue damage rate is proportional to

between 5.3th (for a beam) and 9.6th (for a string) power of the top-end amplitude. It is

not easy to verify this power dependence because there are only 3 different top-end

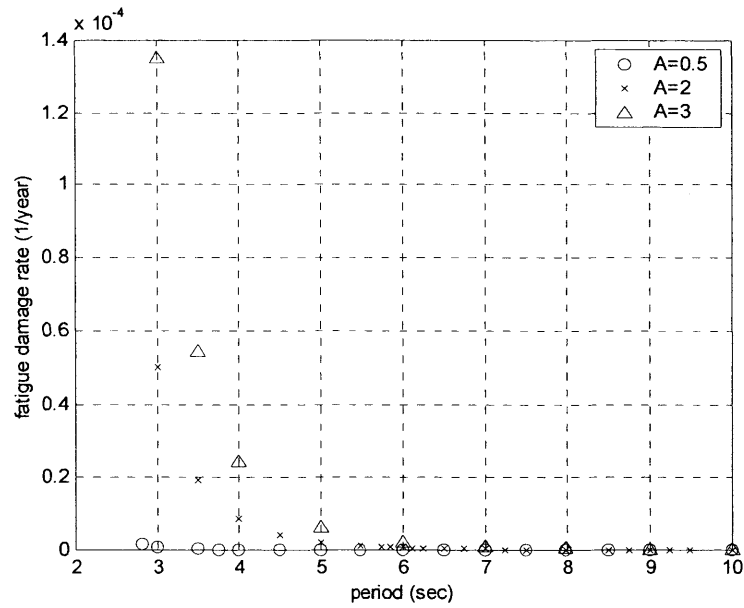amplitudes, but the results demonstrated in Figure 5.32 support this conclusion.



Figure 5.32. The fatigue damage rate estimation for three different top-end excitation
amplitudes of CVAR.

# Chapter 6 Summary

The most important results of this thesis have been shown in Chapter 5. There a VIV model for a slender structure under the top-end periodic motions has been proposed. The construction of the model is based on many important dimensionless parameters. Specifically, an equivalent reduced damping $S_g$ is estimated and the $S_g$-RMS A/D relationship is used to predict the response. Also, the discussions of the amplification factor and the effects of boundary conditions provide insights for the modification and simplification of our model. In summary, we have combined the knowledge from the theories and the experimental results to develop a novel approach to this unsteady VIV problem. In the rest of this chapter, we will review what new insights this thesis presents, how to apply the knowledge to the design of model tests, and what directions future work may take.

## 6.1 New Insights Other Than Steady Flow VIV

Several dimensionless parameters have been identified through this thesis. In previous work of others for steady current VIV, parameters such as St, Re, and the mass ratio have been extensively studied. Here, we would like to address the dimensionless parameters important to the unsteady VIV due to the top-end periodic motion.

For a long slender cylinder, the wave propagation parameter $n\zeta$ determines if we should use the modal method or the wave propagation method to approach this problem. Large $n\zeta$ makes the adjacent modes indistinguishable and thus it should be treated as a wave problem rather than a standing wave vibration problem. This is valid for both steady and unsteady VIV problems. Furthermore, we have discussed the effects of the top-end moving boundary conditions to the inline motions along the riser. The wave propagation parameter $n\zeta$ serves qualitatively as a threshold of determining the importance of the amplification factor, and also quantitatively as the solution of the amplification factor, $\dfrac{1}{\pi n\zeta}$, for small $n\zeta$. The amplification factor is important and should be carefully

investigated because it tells that small amplitude moving boundary conditions can induce large inline motions along the riser.

The solution of an infinite beam under sinusoidal finite length excitation is written in Equation 5.45 as $\dfrac{Y_{max}(x=0)}{D} \sim \dfrac{C_L}{2S_g}(1-e^{-\frac{\pi N_{in}\varsigma}{2}})$. This solution shows that for a beam with a long excitation region, the response will be governed by the ratio of two dimensionless parameters $C_L$ and $S_g$. This ratio is very important because it represents the balance between the excitation force and the damping force. A parameter to characterize the effects of the power-in length is $N_{in}\varsigma$. When $N_{in}\varsigma = 1$, the response amplitude will reach about 80% of the saturated amplitude. The relationship has been shown in Figure 5.7. For an infinite beam with the same excitation length but different frequencies, higher frequencies correspond to larger $N_{in}$, and thus the response amplitude is closer to the saturated amplitude.

For the unsteady flow problem, we have proposed a constant St model based on the observed frequency evolution. That is, the St number is a constant regardless of the sinusoidal change of the inline velocity. The KC number therefore controls how many vortices are shed during one velocity cycle. For a small KC number, the shedding frequencies are governed by the top-end excitation frequency, and mostly the shedding frequencies are multiples of the excitation frequency. As KC gets larger, more vortices are shed during one excitation cycle. We use a parameter $N = \dfrac{KC \cdot St}{\pi}$ to indicate how many vortex pairs are shed per cycle of the riser. Also, the data shows that no significant response amplitude is observed for KC<30. For a spring-mounted cylinder in uniform flow in previous research, VIV response is seen at lower KC numbers. This discrepancy can be explained by the effects of the power-in length shown just above. For the CVAR riser, the excitation region is concentrated on the center portion of the riser. For a very small KC such as 6-20, the inline velocity is small and the corresponding vibration has a

long wavelength. Thus the parameter $N_{in}\varsigma$ becomes relatively small and the response will be at only a few percent of the saturated amplitude. The vibration in a spring-mounted cylinder does not have this 'unsaturated' effect. Thus, a long flexible riser with finite length excitation requires higher KC numbers to have the same scale of response amplitude for a spring-mounted cylinder.

The work in Chapter 5 demonstrates how to develop an equivalent reduced damping model $S_{ge}$ for the unsteady VIV problem. The major concept in this work is to obtain the modification factor $\beta$ by finding the equivalent quasi-steady power-in length for the unsteady excitation. The top-end periodic motion and the riser configuration both influence the value of this factor. The agreement between the measured RMS A/D and the estimated $S_{ge}$ in Figure 5.24 supports the model we developed. An important dimensionless parameter to explain the results of different top-end excitation patterns is the non-dimensional frequency $f_{nd}$. We have demonstrated that normalizing the frequency in terms of $f_{nd}$, we obtain the similar spectra (centered at the same location) for different top-end amplitudes and periods. Also, by carefully choosing the width of the frequency interval, the response amplitude will be the same for the same $f_{nd}$. Thus, the non-dimensional frequency $f_{nd}$ is useful for both the frequency comparisons and the amplitude comparisons for any combination of the top-end excitation. Therefore, if we know the response for one combination of the top-end excitation, we will be able to infer the response for any other excitation by scaling the spectra with $f_{nd}$.

In addition to the dimensionless parameters shown above, we also consider other important parameters such as the mass ratio and Re. Because the available data is limited, we only have one mass ratio and a small range of Re. The range of Re covers only up to the scale of $10^4$, that is, supercritical Re values on the offshore risers are excluded. Thus, the results developed in this thesis can be strictly applied to subcritical flow. More

experiments should be conducted to verify or extend the usage of these results to supercritical Re values.

## 6.2 Guidelines for Model Test Experiment Design

From Equation 2.10, we showed there are 10 dimensionless parameters to characterize the unsteady VIV problem due to the top-end periodic motion. They are

$$Re_0, \frac{m}{\rho_f D^2}, \frac{EI}{TD^2}, \varsigma_s, \frac{L}{D}, \frac{h}{D}, \frac{T}{mgD}, Fr, KC, \frac{V_0/D}{\sqrt{K/m}}. \tag{6.1}$$

In principle, if we would like to build a model test for a prototype, these 10 parameters should all be the same. In practice, however, it is not possible to make all the matching between two different scales. Thus we have to sacrifice some of the matching to scale the system.

First we would like to obey the geometric similarity. For a prototype and a model, we require that all the shapes be similar, but only different in length scale. We assume the scaling between the two systems is

$$k_D = \frac{D_p}{D_m}, \tag{6.2}$$

where $D_p$ is the diameter of the prototype, while $D_m$ is the diameter of the model. The dimensionless parameters associated with the geometric similarity are $\frac{L}{D}, \frac{h}{D}$, and $KC$.

To satisfy the geometric similarity, the scaling requirements are

$$\frac{D_p}{D_m} = \frac{L_p}{L_m} = \frac{h_p}{h_m} = \frac{A_p}{A_m} = k_D. \tag{6.3}$$

That is, we have to make a model with the same length ratio for the diameter, the riser length, and the water depth. Also the top-end excitation amplitude should be in the same scale. Next, in order to have the same static geometric shape, both the mass ratios and the

124

parameters $\dfrac{T}{mgD}$ for the model test and the prototype should be the same. In practice,

gravity is not easy to change, and also the fluid will likely be the same (i.e., water). Therefore, we have

$$\begin{aligned}
\rho_{fp} &= \rho_{fm}, \\
\mu_p &= \mu_m, \\
g_p &= g_m.
\end{aligned}$$

(6.4)

The matching of the mass ratio is written as:

$$\frac{m_p}{\rho_{fp} D_p^2} = \frac{m_m}{\rho_{fm} D_m^2}.$$

(6.5)

With the same fluid density, the scaling of the mass per unit length of the structure is

$$\frac{m_p}{m_m} = \frac{D_p^2}{D_m^2} = k_D^2.$$

(6.6)

To satisfy this scaling requirement, we should use the same kind of material (i.e., the same density) for the model test and the prototype, because this scaling in Equation 6.6 is the same as the ratio of the cross-sectional area. The matching of $\dfrac{T}{mgD}$ is

$$\frac{T_p}{m_p g_p D_p} = \frac{T_m}{m_m g_m D_m},$$

(6.7)

or the scaling of the top-end tension is

$$\frac{T_p}{T_m} = \frac{m_p D_p}{m_m D_m} = k_D^3.$$

(6.8)

The tension at the top should be intentionally set to the 3$^{rd}$ power of the length ratio. With the scaling of the tension, we can scale the bending stiffness $EI$ by matching the

parameter $\dfrac{EI}{TD^2}$:

$$\frac{E_p I_p}{T_p D_p^{\,2}} = \frac{E_m I_m}{T_m D_m^{\,2}}. \tag{6.9}$$

We separately discuss the scaling of the Young's modulus and the moment of inertia. The moment of inertia is proportional to the 4$^{th}$ power of the diameter, so the scaling is

$$\frac{I_p}{I_m} = k_D^{\,4}. \tag{6.10}$$

Therefore, the scaling of the Young's modulus is

$$\frac{E_p}{E_m} = \frac{T_p D_p^{\,2}}{T_m D_m^{\,2}} \frac{I_m}{I_p} = k_D. \tag{6.11}$$

We should choose a material with a lower Young's modulus for the model. The damping ratios chosen for the model and the prototype can be the same for the matching. Now, only the parameters associated with the dynamic similarity remain. In order to match the Re number, the relationship

$$\frac{\rho_{fp} D_p V_{0p}}{\mu_p} = \frac{\rho_{fm} D_m V_{0m}}{\mu_m} \tag{6.12}$$

has to be satisfied. Because of the same fluid density and viscosity, the top-end velocity should be scaled as

$$\frac{V_{0p}}{V_{0m}} = \frac{D_m}{D_p} = \frac{1}{k_D}. \tag{6.13}$$

For matching the Fr number, we have

$$\frac{V_{0p}}{\sqrt{g_p D_p}} = \frac{V_{0m}}{\sqrt{g_m D_m}}, \tag{6.14}$$

or we have the scaling for the top-end velocity:

$$\frac{V_{0p}}{V_{0m}} = \sqrt{k_D}. \tag{6.15}$$

Equation 6.13 and Equation 6.15 conflict each other, so it is not possible to both satisfy the Froude-number scaling and the Reynolds-number scaling. That is, we have to sacrifice one of them to proceed. To decide which scaling is suitable for our problem, we consider the variables we are interested in. In general, we expect all frequencies (e.g., the top-end excitation frequency, the shedding frequency) to be in the same scale as the natural frequency. We write again the natural frequency for a tensioned beam:

$$f_{nat} = \frac{1}{2\pi} \sqrt{\frac{EI}{m_t} (\frac{n\pi}{L})^4 + \frac{T}{m_t} (\frac{n\pi}{L})^2}.$$
(6.16)

The scaling of the natural frequency is

$$\frac{f_{natp}}{f_{natm}} = \frac{\sqrt{E_p I_p / m_p L_p^4}}{\sqrt{E_m I_m / m_m L_m^4}} = \frac{\sqrt{T_p / m_p L_p^2}}{\sqrt{T_m / m_m L_m^2}} = \sqrt{\frac{1}{k_D}}.$$
(6.17)

Equation 6.15 implies the scaling of the top-end excitation frequency:

$$\frac{f_{extp}}{f_{extm}} = \frac{V_{0p} / A_p}{V_{0m} / A_m}.$$
(6.18)

Putting the Froude-number scaling for the velocity in this equation, we obtain

$$\frac{f_{extp}}{f_{extm}} = \sqrt{\frac{1}{k_D}}.$$
(6.19)

Therefore, in terms of matching the frequency, it is necessary to use the Froude-number scaling and discard the Reynolds-number scaling. The scaling of the excitation frequency should be carefully set according to Equation 6.19. Also, the maximum possible shedding frequency can be written as

$$f_s = \frac{St V_0}{D}.$$
(6.20)

Assuming constant St and using the Froude-number scaling for the velocity, we obtain

$$\frac{f_{sp}}{f_{sm}} = \frac{V_{0p} D_m}{V_{0m} D_p} = \sqrt{\frac{1}{k_D}}.$$
(6.21)

In order to have the same St without matching the Re number, the cylinder has to be roughened so that we have a nearly constant St curve with respect to Re. The last parameter to match is $\dfrac{V_0/D}{\sqrt{K/m}}$, and the scaling for the soil stiffness is:

$$\frac{K_p}{K_m} = \frac{m_p V_{0p}^{\ 2}/D_p^{\ 2}}{m_m V_{0m}^{\ 2}/D_m^{\ 2}} = k_D. \tag{6.22}$$

That is, for the model test, we have to find a material softer (with the scale as in Equation 6.22) than the soil stiffness in the prototype. In summary, to follow the Froude-number scaling, Equations 6.3, 6.6, 6.8, 6.11, 6.19, and 6.22 have to be satisfied. Also, because the Re number does not match, careful judgment should be made to assure the equivalence between the prototype and the model test.

Now we would like to examine the scaling rules for some important parameters. The added mass coefficient $C_m$ must be the same to keep the total mass per unit length the same. $C_m$ is a function of the Re number, the KC number, and the reduced velocity. The KC number has been kept the same. The effects of the Re number on the response frequency, and thus the reduced velocity, should be justified so that added mass coefficient does not vary too much. Next we test the drag force per unit length. The balance between the drag force and the total weight of the riser (including the added mass weight) should match for the model and the prototype in order to have the correct scaling of the dynamic behavior. The ratio of the drag force to the weight is $\dfrac{\frac{1}{2}\rho_f D C_D V^2}{m_t g}$.

Plugging all the scaling into this ratio, we need a constant drag coefficient for both the model and the prototype. $C_D$ is a function of Re. If we roughen the cylinder, the drag coefficient will not vary much for different Re. Therefore, a roughened cylinder will also satisfy the requirement for the drag coefficient. For the reduced damping, the matching is

$$\frac{R_p \omega_p}{\rho_{fp} V_p^{\ 2}} = \frac{R_m \omega_m}{\rho_{fm} V_m^{\ 2}}, \tag{6.23}$$

or

$$\frac{R_p}{R_m} = \frac{V_p^2 f_m}{V_m^2 f_p} = k_D^{3/2}.$$ (6.24)

For the steady flow problem, the model for the damping coefficient (the still water contribution) used in SHEAR7 again requires the equivalent effect of the Re number.

## 6.3 New Contributions

This thesis makes the following new contributions:

1. Solved the turning point problem for a tensioned beam with a linearly varying stiffness foundation.

2. Established simple rules for conservative estimation of TDP fatigue damage (effect of soil interactions). Being able to solve the complicated models such as the linearly varying foundation model and the discontinuity model, we verified that the simple pinned-pinned model is more conservative than these complicated models in term of the curvature, or equivalently the fatigue damage rate.

3. Determined the effect of the wave propagation parameter, $n\zeta$, on the response to a periodic moving boundary. The amplification effects due to the periodic moving boundary conditions are significant if $n\zeta$ is small. The factor can be up to 10 times the boundary motion amplitude. The amplification factor for small $n\zeta$ is $\dfrac{1}{\pi n\zeta}$.

4. Examined the importance of dimensionless parameters KC, reduced damping $S_g$, non-dimensional frequency, and $n\zeta$ for unsteady VIV due to top-end periodic motion. The effects of the KC number on the response frequency were discussed. The KC number also serves as a threshold for the response amplitude. The reduced damping $S_g$ is present in the solution of a damped system.

5. Developed an equivalent reduced damping $S_{ge}$ model for unsteady VIV. The equivalent reduced damping model was developed by introducing a conservative and equivalent quasi-steady model. A modification factor to include the effects of

129

the riser configuration and the top-end excitation was proposed in obtaining the equivalent reduced damping $S_{ge}$. The CVAR data was used to verify the $S_{ge}$-RMS A/D relationship, and a fatigue damage rate model was established based on this relationship.

6.  Obtained a simple formula for the effect of the excitation length on the VIV response of an infinitely long system. An important dimensionless parameter $N_{in}\varsigma$ was identified. Using the results of the finite length excitation, we are able to explain the high KC threshold observed in the response.

7.  Provided guidelines for the model test experiment design based on dimensional analysis and scaling rules. A careful derivation of the scaling rules was conducted. The Froude-number scaling was used and the matching of the Re number was compensated by roughening the cylinder for the model test.

## 6.4 Further Work

We suggest the following directions for extending the work in this thesis.

1.  Use the equivalent reduced damping model for other known velocity profiles, and verify the $S_g$-RMS A/D relationship. It will be important to test the proposed model against other sets of data. The velocity profile for the experiment is needed to obtain the equivalent reduced damping. It will be interesting to compare the response for different riser configurations.

2.  Modify the reduced damping model for the unsteady VIV by including the effects of the correlation length, the spatial decay, and the more sophisticated hydrodynamic damping model. The reduced damping model proposed in this thesis is only a first step toward this complicated unsteady VIV problem. The effects of the correlation length, the spatial decay of the power into the system, and better hydrodynamic damping model should be included to establish the prediction model.

3. Explore the unsteady VIV problem for other ranges of the KC number. There is a KC number gap between KC=40 and KC=100. Future experiments should be conducted to fill this gap. Higher KC number cases should also be explored so that the trend between the unsteady flow and steady flow problems can be characterized.

4. Conduct the full-scale test specifically for improving the unsteady VIV model. The measurement from the full-scale test can be use to verify and calibrate the unsteady VIV model proposed here. The effects of the high Re numbers can also be identified from the full-scale test.

# Appendix 1 Derivation of the Solution for the Turning Point Problem

The governing equation of a tensioned beam with linearly varying spring constant is written as:

$$EI \frac{\partial^4 y}{\partial x^4} - T \frac{\partial^2 y}{\partial x^2} + m \frac{\partial^2 y}{\partial t^2} + k(x)y = 0. \tag{1.1}$$

Assuming a harmonic solution $y = Y(x)e^{-i\omega t}$ and $k(x) = ax + m\omega^2$ as in the string case, we get

$$\frac{d^4 Y}{dx^4} - \frac{T}{EI} \frac{d^2 Y}{dx^2} + \frac{a}{EI} xY = 0. \tag{1.2}$$

Using the normalization

$$\bar{x} = \left( \frac{a}{EI} \right)^{\frac{1}{5}} x,$$

we have

$$\frac{d^4 Y}{d\bar{x}^4} - p \frac{d^2 Y}{d\bar{x}^2} + \bar{x}Y = 0, \tag{1.3}$$

where $p = \dfrac{T}{EI} \left( \dfrac{a}{EI} \right)^{-\frac{2}{5}}$, $p > 0$. We try an integral representation with the form

$$Y(\bar{x}) = \int_c e^{-\bar{x}s} f(s) ds, \tag{1.4}$$

where $f(s)$ is a function to be found to satisfy the differential equation and $c$ is a special contour discussed later. The derivatives of this integral are:

$$\frac{dY}{d\bar{x}} = \int_c e^{-\bar{x}s} (-sf(s)) ds,$$

$$\frac{d^2 Y}{d\bar{x}^2} = \int_c e^{-\bar{x}s} (s^2 f(s)) ds,$$

$$\frac{d^4 Y}{d\bar{x}^4} = \int_c e^{-\bar{x}s} (s^4 f(s)) ds,$$

and

$$\bar{x}Y = \int_c e^{-\bar{x}s} \frac{df(s)}{ds} ds - e^{-\bar{x}s} f(s) \Big|_\alpha^\beta,$$

133

where $\alpha$ and $\beta$ are the end points of the contour $c$. In order to implement the integral representation, $e^{-\bar{x}s}f(s)\big|_{\alpha}^{\beta}$ has to be zero. We can insert all the corresponding terms into Equation 1.3 and get

$$\int_{c} e^{-\bar{x}s}\left[ s^4 f(s) - ps^2 f(s) + \frac{df(s)}{ds} \right] ds = 0,$$

or

$$s^4 f(s) - ps^2 f(s) + \frac{df(s)}{ds} = 0. \tag{1.5}$$

Solving this differential equation for $f(s)$, we obtain

$$f(s) = e^{-\frac{s^5}{5}+p\frac{s^3}{3}}, \tag{1.6}$$

and

$$Y(\bar{x}) = \int_{c} e^{-\bar{x}s+p\frac{s^3}{3}-\frac{s^5}{5}} ds. \tag{1.7}$$

Thus, Equation 1.7 is the solution for a tensioned beam with a linearly varying spring constant, provided the end points $\alpha$ and $\beta$ of the contour $c$ satisfy the condition

$$e^{-\bar{x}s+p\frac{s^3}{3}-\frac{s^5}{5}}\bigg|_{\alpha}^{\beta} = 0. \tag{1.8}$$

One of the choices for the contour is to make the values at the end points convergent to 0, that is, to make $-\bar{x}s + p\frac{s^3}{3} - \frac{s^5}{5} \to -\infty$. Letting $s = \rho e^{i\theta}$, as $\rho \to \infty$, the term $-\frac{s^5}{5}$ becomes dominant. We have

$$-\frac{s^5}{5} = -\frac{\rho^5}{5}e^{i5\theta} = -\frac{\rho^5}{5}(\cos 5\theta + i\sin 5\theta).$$

If $\cos 5\theta > 0$, then $e^{-\bar{x}s+p\frac{s^3}{3}-\frac{s^5}{5}} \to 0$ as $\rho \to \infty$. Therefore, the phase has to be in the following zones:

$$-\frac{\pi}{10} < \theta < \frac{\pi}{10}, \frac{3\pi}{10} < \theta < \frac{5\pi}{10}, \frac{7\pi}{10} < \theta < \frac{9\pi}{10}, \frac{-9\pi}{10} < \theta < \frac{-7\pi}{10}, \frac{-5\pi}{10} < \theta < \frac{-3\pi}{10},$$

which are shown in Figure 1.1. Any contour that originates from one of these zones and ends in another of these zones will be a valid contour. Therefore, we have five zones and

134

four independent solutions, each of which connects two different zones. This corresponds to four solutions for a fourth order differential equation.
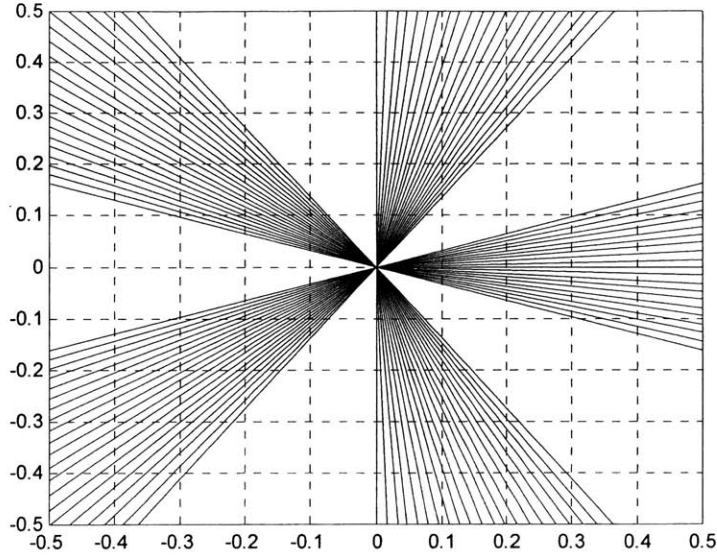


Figure 1.1. Zones of valid contour terminations.

First we explore the approximations around the turning point using Taylor's expansion. Close to the turning point $\overline{x} = 0$, we can expand the integral representation as:

$$
\begin{aligned}
Y(\overline{x}) &= \int_c e^{-\overline{x}s + p\frac{s^3}{3} - \frac{s^5}{5}} \, ds \\
&= \sum_{n=0}^{\infty} \frac{(-\overline{x})^n}{n!} \int_c s^n e^{p\frac{s^3}{3} - \frac{s^5}{5}} \, ds.
\end{aligned}
\tag{1.9}
$$

To obtain the four independent solutions, we have to assign four different contours for the integral. From the valid zones of integration in Figure 1.1, it is known that any of these contours is composed of the following integral sub-contours:

$$
\int_0^{\infty e^{-i\frac{4\pi}{5}}}, \int_0^{\infty e^{-i\frac{2\pi}{5}}}, \int_0^{\infty}, \int_0^{\infty e^{i\frac{2\pi}{5}}}, \int_0^{\infty e^{i\frac{4\pi}{5}}},
$$

or these can be written as a unified form:

$$
I_q = \int_0^{\infty e^{i\frac{2q\pi}{5}}} s^n e^{p\frac{s^3}{3} - \frac{s^5}{5}} \, ds,
\tag{1.10}
$$

where $q = -2, -1, 0, 1, 2$. This integral can be simplified by introducing the change of variable

135

$$\sigma = se^{i\frac{2q\pi}{5}}$$

and Equation 1.10 becomes

$$I_q \equiv e^{i\frac{2\pi}{5}q(n+1)} \int_0^\infty \sigma^n e^{-\frac{\sigma^5}{5}+p\frac{\sigma^3}{3}e^{i\frac{6q\pi}{5}}} \, d\sigma.$$ (1.11)

The integral has to be carried out numerically. With these sub-contour components, we have to decide the combinations of these components to form four different contour integrals. In order to make all four solutions real, four combinations are selected as follows and the contours are shown in Figure 1.2:

$$C_A = \frac{1}{2i}\sum_{n=0}^\infty \frac{(-\bar{x})^n}{n!}(I_2 - I_{-2}),$$

$$C_B = \frac{1}{2i}\sum_{n=0}^\infty \frac{(-\bar{x})^n}{n!}(I_1 - I_{-1}),$$

$$C_C = \frac{1}{2}\sum_{n=0}^\infty \frac{(-\bar{x})^n}{n!}(I_1 + I_{-1} - I_2 - I_{-2}),$$ (1.12)

$$C_D = \frac{1}{2}\sum_{n=0}^\infty \frac{(-\bar{x})^n}{n!}(2I_0 - I_1 - I_{-1}).$$

The coefficients $\frac{1}{2i}$ and $\frac{1}{2}$ are used to normalize and to make the results real. Adding up the first several terms of these series will be enough to capture the behavior around $\bar{x} = 0$ and to match with the asymptotic solutions on both sides.
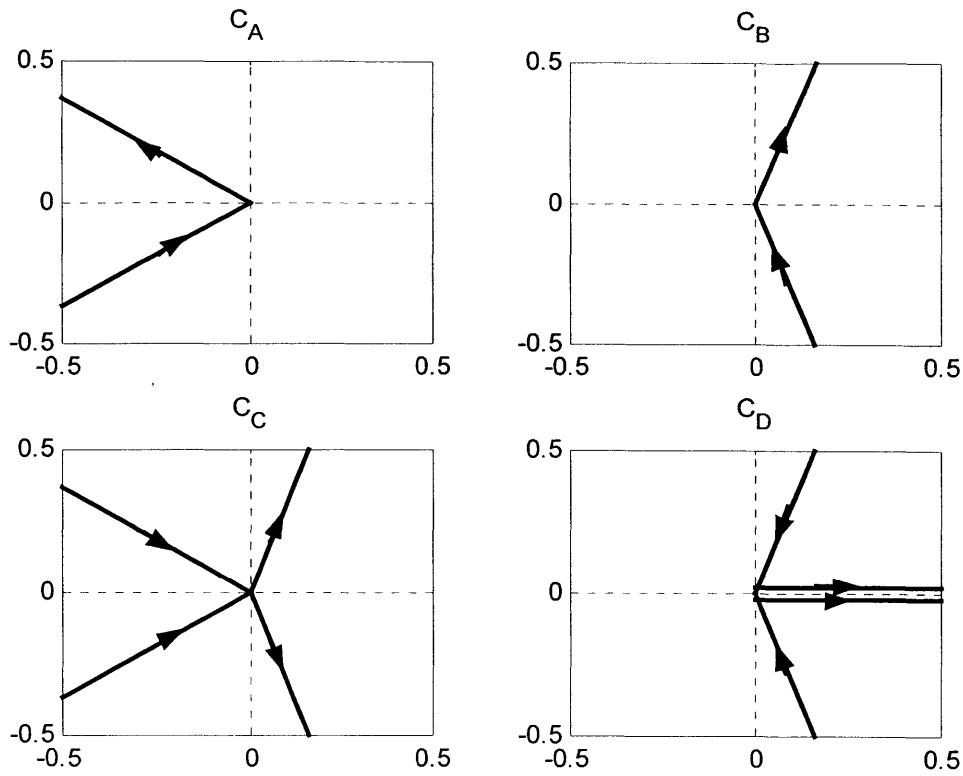
Figure 1.2. Four contours for Taylor's expansion solutions.

To use the steepest descent method for the asymptotic solutions, the saddle points have to be found first. The exponent of the integrand is

$$h(s) = -\bar{x}s + p\frac{s^3}{3} - \frac{s^5}{5}.$$  (1.13)

The derivatives of $h(s)$ are

$$h'(s) = -\bar{x} + ps^2 - s^4,$$  (1.14)

and

$$h''(s) = 2ps - 4s^3.$$  (1.15)

The saddle points have to satisfy

$$h'(s) = -\bar{x} + ps^2 - s^4 = 0.$$  (1.16)

The locations of the saddle points will depend on $\bar{x}$. The values of the saddle points are shown in Table 1.1 and the locations are shown in Figure 1.3.

Table 1.1. Saddle points for different values of $\bar{x}$. At the bottom line,

$$\theta = \tan^{-1}\frac{\sqrt{4\bar{x}-p^2}}{p}, \quad 0<\theta<\frac{\pi}{2}.$$

| Saddle point | a | b | c | d |
|---|---|---|---|---|
| $\bar{x}<0$ | $\sqrt{\dfrac{p+\sqrt{p^2-4\bar{x}}}{2}}$ | $i\sqrt{\dfrac{\sqrt{p^2-4\bar{x}}-p}{2}}$ | $-\sqrt{\dfrac{p+\sqrt{p^2-4\bar{x}}}{2}}$ | $-i\sqrt{\dfrac{\sqrt{p^2-4\bar{x}}-p}{2}}$ |
| $0<\bar{x}<\dfrac{p^2}{4}$ | $\sqrt{\dfrac{p+\sqrt{p^2-4\bar{x}}}{2}}$ | $\sqrt{\dfrac{p-\sqrt{p^2-4\bar{x}}}{2}}$ | $-\sqrt{\dfrac{p+\sqrt{p^2-4\bar{x}}}{2}}$ | $-\sqrt{\dfrac{p-\sqrt{p^2-4\bar{x}}}{2}}$ |
| $\bar{x}>\dfrac{p^2}{4}$ | $\bar{x}^{\frac{1}{4}}e^{i\frac{\theta}{2}}$ | $\bar{x}^{\frac{1}{4}}e^{-i\frac{\theta}{2}}$ | $\bar{x}^{\frac{1}{4}}e^{-i\left(\pi-\frac{\theta}{2}\right)}$ | $\bar{x}^{\frac{1}{4}}e^{i\left(\pi-\frac{\theta}{2}\right)}$ |



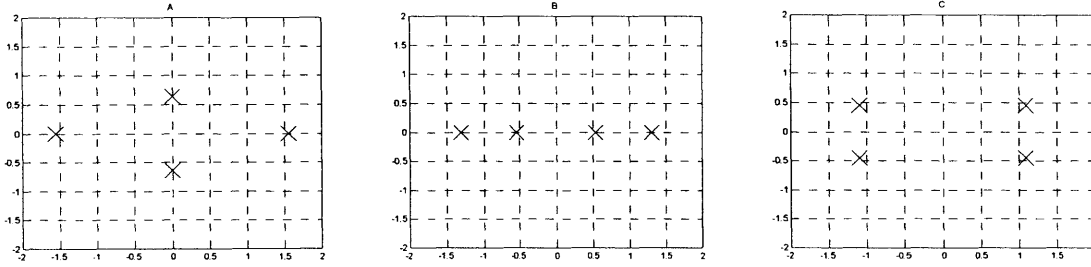Figure 1.3. The saddle point locations for A. $\bar{x}<0$, B. $0<\bar{x}<\dfrac{p^2}{4}$, C. $\bar{x}>\dfrac{p^2}{4}$.

The steepest descent contours have $\mathrm{Im}\big(h(s)\big)=\text{constant}$. Letting $s=s_r+is_i$, we get

$$h(s_r+is_i)=(-\bar{x}s_r+\frac{p}{3}s_r^3-ps_rs_i^2-\frac{1}{5}s_r^5+2s_r^3s_i^2-s_rs_i^4)$$
$$+i(-\bar{x}s_i+ps_r^2s_i-\frac{p}{3}s_i^3-s_r^4s_i+2s_r^2s_i^3-\frac{1}{5}s_i^5). \tag{1.17}$$

For a contour passing through a saddle point, the imaginary part of Equation 1.17 has to satisfy

$$-\bar{x}s_i+ps_r^2s_i-\frac{p}{3}s_i^3-s_r^4s_i+2s_r^2s_i^3-\frac{1}{5}s_i^5=\mathrm{Im}(h(s_0)), \tag{1.18}$$

138

where $s_0$ is the value of a saddle point. With Equation 1.18 and the locations of saddle points as shown in Table 1.1, we can plot the steepest descent contours and identify specific paths to have maximum real part of $h(s)$ at the saddle points.

When $\bar{x} < 0$, the steepest descent contours for four saddle points are shown in Figure 1.4. The thin lines are those with constant imaginary $h(s)$, while the thick lines are the integration paths with maximum real parts of $h(s)$ at the saddle points.
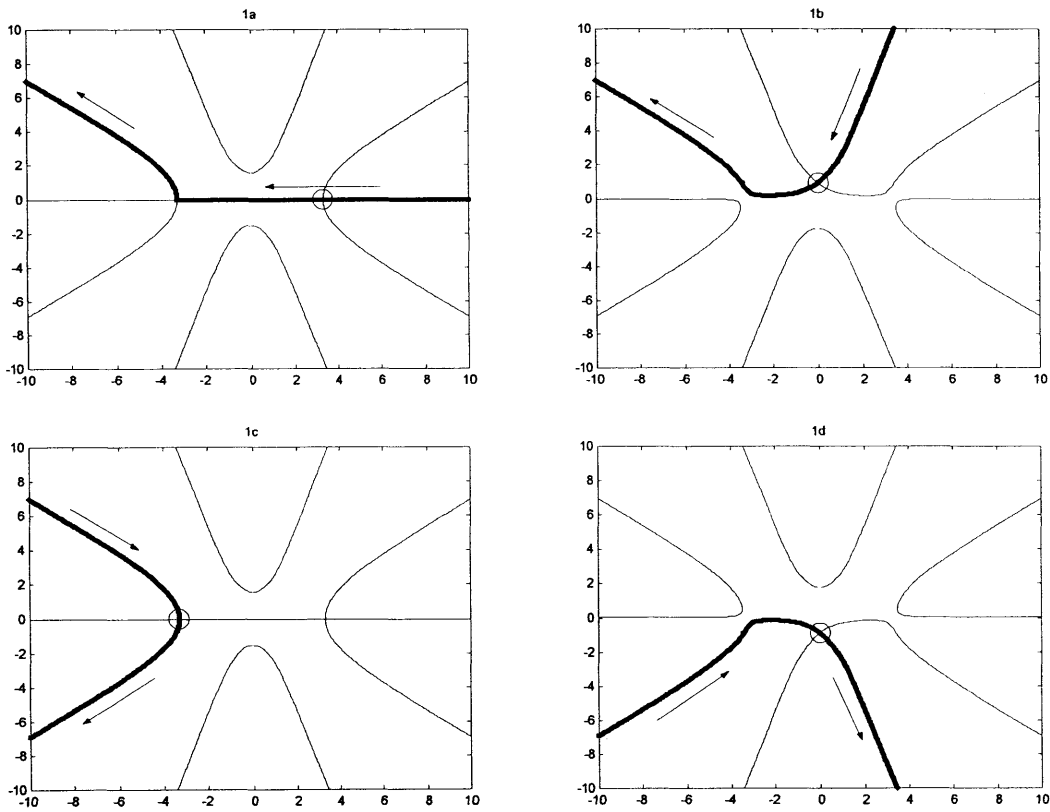


Figure 1.4. The steepest descent contours (thin lines) and the integration paths (thick lines) of all four saddle points (marked in circles) for $\bar{x} < 0$. Arrows are the directions of integration.

139

To illustrate how to carry out the asymptotic solution by the steepest descent method, we calculate the solution for the case 1a, that is, the saddle point $s_{1a} = \sqrt{\dfrac{p + \sqrt{p^2 - 4\bar{x}}}{2}}$ for $\bar{x} < 0$. Expanding $h(s)$ around the saddle point, we get

$$h(s) = h(s_{1a}) + \underbrace{h'(s_{1a})(s - s_{1a})} + \frac{h''(s_{1a})}{2!}(s - s_{1a})^2 + \dots .\qquad(1.19)$$

The second term of the right side vanishes because of the requirement of a saddle point. The terms $h(s_0)$ and $h''(s_0)$ can be carried out by plugging the value of the saddle point into Equations 1.13 and 1.15. Thus, the solution becomes

$$Y(\bar{x}) \sim e^{h(s_{1a})} \int_c e^{\frac{h''(s_{1a})}{2!}(s - s_{1a})^2} \, ds. \qquad(1.20)$$

To further simplify the integral in Equation 1.20, let

$$\sigma^2 = -\frac{h''(s_{1a})}{2!}(s - s_{1a})^2,$$

where

$$\begin{aligned} h''(s_{1a}) &= 2ps_{1a} - 4s_{1a}^3 \\ &= -\sqrt{2p + 2\sqrt{p^2 - 4\bar{x}}} \sqrt{p^2 - 4\bar{x}}. \end{aligned}\qquad(1.21)$$

Thus, we get

$$\sigma = \pm\sqrt{\frac{\sqrt{2p + 2\sqrt{p^2 - 4\bar{x}}}\sqrt{p^2 - 4\bar{x}}}{2}}(s - s_{1a}),$$

and we have to decide which sign carries the correct integration direction. The direction we like in the $\sigma$ domain is from $-\infty$ to $+\infty$, while from Figure 1.4 1a the assigned integration direction in the $s$ domain is nearly from $+\infty$ to $-\infty$. Therefore, we have to select the negative sign to have a consistent integration direction, that is,

$$\sigma = -\sqrt{\frac{\sqrt{2p + 2\sqrt{p^2 - 4\bar{x}}}\sqrt{p^2 - 4\bar{x}}}{2}}(s - s_{1a}),\qquad(1.22)$$

or

$$\sigma = -g_{1a}(\bar{x})(s - s_{1a}),\qquad(1.23)$$

where

140

$$g_{1a}(\bar{x}) \equiv \sqrt{\frac{\sqrt{2p + 2\sqrt{p^2 - 4\bar{x}}\sqrt{p^2 - 4\bar{x}}}}{2}}.$$ (1.24)

Plugging Equation 1.23 into Equation 1.20, the solution becomes

$$Y(\bar{x}) \sim \frac{e^{h(s_{1a})}}{-g_{1a}(\bar{x})} \int_{left}^{right} e^{-\sigma^2} d\sigma.$$ (1.25)

Because the main contribution for the integration in the equation is around the saddle point, that is, around $\sigma = 0$, we can extend the integration region and the solution will not change much. We thus can write the asymptotic solution as

$$Y(\bar{x}) \sim \frac{e^{h(s_{1a})}}{-g_{1a}(\bar{x})} \int_{-\infty}^{\infty} e^{-\sigma^2} d\sigma,$$ (1.26)

or

$$Y(\bar{x}) \sim \frac{\sqrt{\pi} e^{h(s_{1a})}}{-g_{1a}(\bar{x})}.$$ (1.27)

This is the asymptotic solution of 1a. Similar procedures can be followed to obtain the solutions for 1b, 1c and 1d. The results are shown in Table 1.2.

Table 1.2. The asymptotic solutions of four saddle points for $\bar{x} < 0$.

| 1a | 1b |
|---|---|
| $Y_{1a}(\bar{x}) \sim \dfrac{\sqrt{\pi} e^{h(s_{1a})}}{-g_{1a}(\bar{x})}$ | $Y_{1b}(\bar{x}) \sim \dfrac{\sqrt{\pi} e^{h(s_{1b})}}{e^{i\frac{3\pi}{4}} g_{1b}(\bar{x})}$ |
| $g_{1a} = \sqrt{\dfrac{\sqrt{2p + 2\sqrt{p^2 - 4\bar{x}}}\sqrt{p^2 - 4\bar{x}}}{2}}$ | $g_{1b} = \sqrt{\dfrac{\sqrt{2\sqrt{p^2 - 4\bar{x}} - 2p}\sqrt{p^2 - 4\bar{x}}}{2}}$ |
| 1c | 1d |
| $Y_{1c}(\bar{x}) \sim \dfrac{\sqrt{\pi} e^{h(s_{1c})}}{i g_{1c}(\bar{x})}$ | $Y_{1d}(\bar{x}) \sim \dfrac{\sqrt{\pi} e^{h(s_{1d})}}{e^{i\frac{\pi}{4}} g_{1d}(\bar{x})}$ |
| $g_{1c} = \sqrt{\dfrac{\sqrt{2p + 2\sqrt{p^2 - 4\bar{x}}}\sqrt{p^2 - 4\bar{x}}}{2}}$ | $g_{1a} = \sqrt{\dfrac{\sqrt{2\sqrt{p^2 - 4\bar{x}} - 2p}\sqrt{p^2 - 4\bar{x}}}{2}}$ |

To match the solutions close to the turning point by Taylor's expansion method, we have to combine the asymptotic solutions correctly to generate the same integration paths. Table 1.3 shows the matching between Taylor's expansion solutions and the asymptotic solution for $\bar{x} < 0$.

Table 1.3. The matching between Taylor's expansion solutions and the asymptotic solution for $\bar{x} < 0$.

| Taylor's | $C_A$ | $C_B$ | $C_C$ | $C_D$ |
|---|---|---|---|---|
| Asymptotic | $-\dfrac{(1c)}{2i}$ | $-\dfrac{(1b)+(1c)+(1d)}{2i}$ | $\dfrac{(1d)-(1b)}{2}$ | $\dfrac{-2(1a)+(1b)-(1d)}{2}$ |

Figure 1.5 shows the steepest descent contours and the integration paths for $0 < \bar{x} < \dfrac{p^2}{4}$. The solutions can be obtained by the same procedure described above for $\bar{x} < 0$. Notice that $p = \dfrac{T}{EI}\left(\dfrac{a}{EI}\right)^{-2/5}$, where $a$ is the slope of the linearly varying spring constant. In our case $p$ may be small, so that the solutions in this range can actually be covered by Taylor's expansion around the turning point $\bar{x} = 0$. In this situation we can skip the calculations of the asymptotic solutions in this range.
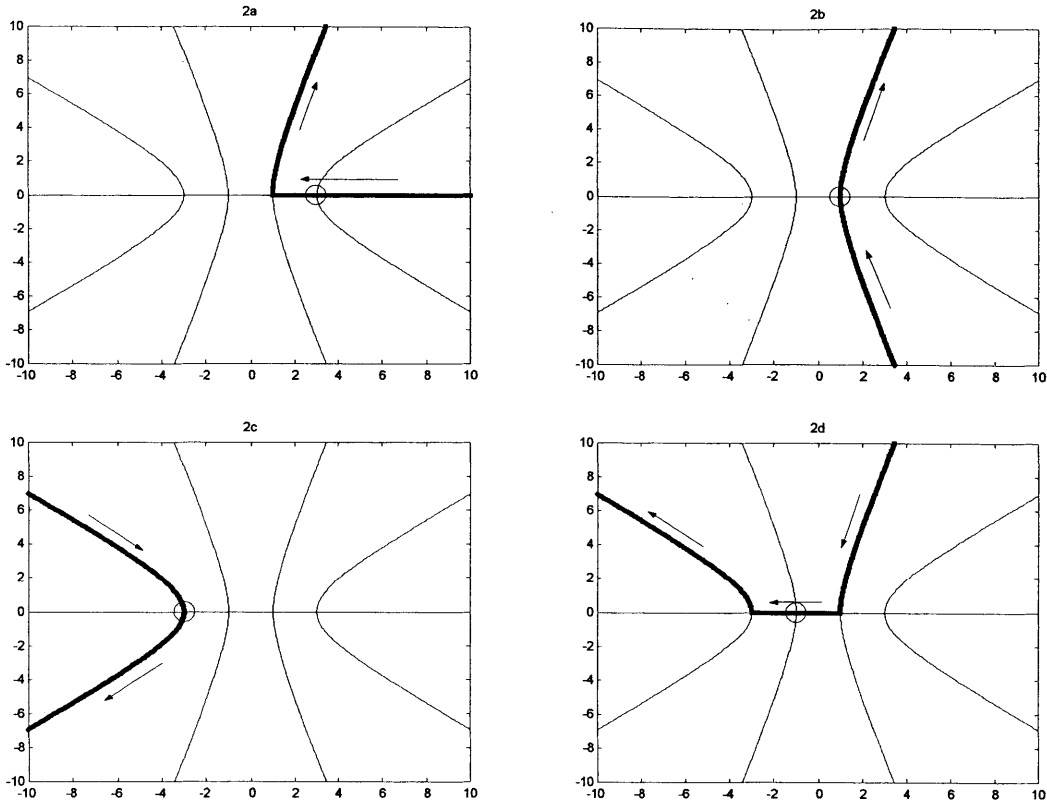
Figure 1.5. The steepest descent contours (thin lines) and the integration paths (thick lines) of all four saddle points (marked in circles) for $0 < \bar{x} < \dfrac{p^2}{4}$. Arrows are the directions of integration.

The steepest descent contours and the integration paths for $\bar{x} > \dfrac{p^2}{4}$ are shown in Figure 1.6. Following similar steps and assigning a relation

$$A^2 e^{2i\phi} \equiv -p\bar{x}^{-\frac{1}{4}} e^{i\frac{\theta}{2}} + 2\bar{x}^{-\frac{3}{4}} e^{i\frac{3\theta}{2}}, \tag{1.28}$$

where $A > 0$ and $0 < \phi < \dfrac{\pi}{2}$, we obtain the asymptotic solutions in Table 1.4. To match the solutions from the integration paths with the solutions around the turning point, the combinations of these asymptotic solutions are shown in Table 1.5.
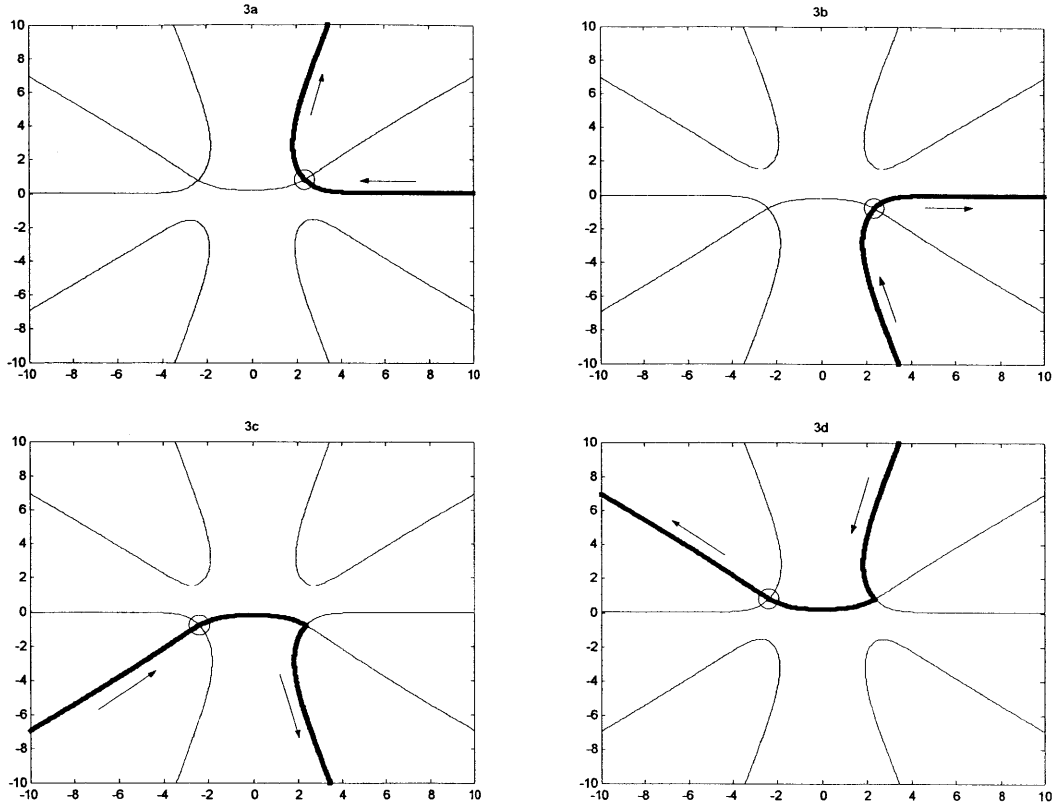
Figure 1.6. The steepest descent contours (thin lines) and the integration paths (thick lines) of all four saddle points (marked in circles) for $\bar{x} > \dfrac{p^2}{4}$. Arrows are the directions of integration.

Table 1.4. The asymptotic solutions of four saddle points for $\bar{x} > \dfrac{p^2}{4}$.

| 3a | 3b | 3c | 3d |
|---|---|---|---|
| $Y_{3a}(\bar{x}) \sim \dfrac{\sqrt{\pi}e^{h(s_{3a})}}{-Ae^{i\phi}}$ | $Y_{3b}(\bar{x}) \sim \dfrac{\sqrt{\pi}e^{h(s_{3b})}}{Ae^{-i\phi}}$ | $Y_{3c}(\bar{x}) \sim \dfrac{\sqrt{\pi}e^{h(s_{3c})}}{Ae^{i(\phi-\frac{\pi}{2})}}$ | $Y_{3d}(\bar{x}) \sim \dfrac{\sqrt{\pi}e^{h(s_{3d})}}{-Ae^{i(\frac{\pi}{2}-\phi)}}$ |

144

Table 1.5. The matching between Taylor's expansion solutions and the asymptotic solution for $\bar{x} > \dfrac{p^2}{4}$.

| Taylor's | $C_A$ | $C_B$ | $C_C$ | $C_D$ |
|---|---|---|---|---|
| Asymptotic | $\dfrac{(3a)+(3b)+(3c)+(3d)}{2i}$ | $\dfrac{(3a)+(3b)}{2i}$ | $\dfrac{(3c)-(3d)}{2}$ | $\dfrac{(3b)-(3a)}{2}$ |

Now we are able to patch together all the solutions for the left side, right side, and close to the turning point to get a global solution. Figure 1.7 shows four solutions for a typical tensioned beam with linearly varying stiffness. To obtain a physically meaningful solution for a specific problem, boundary conditions have to be imposed to decide the weighting of each of these four solutions.
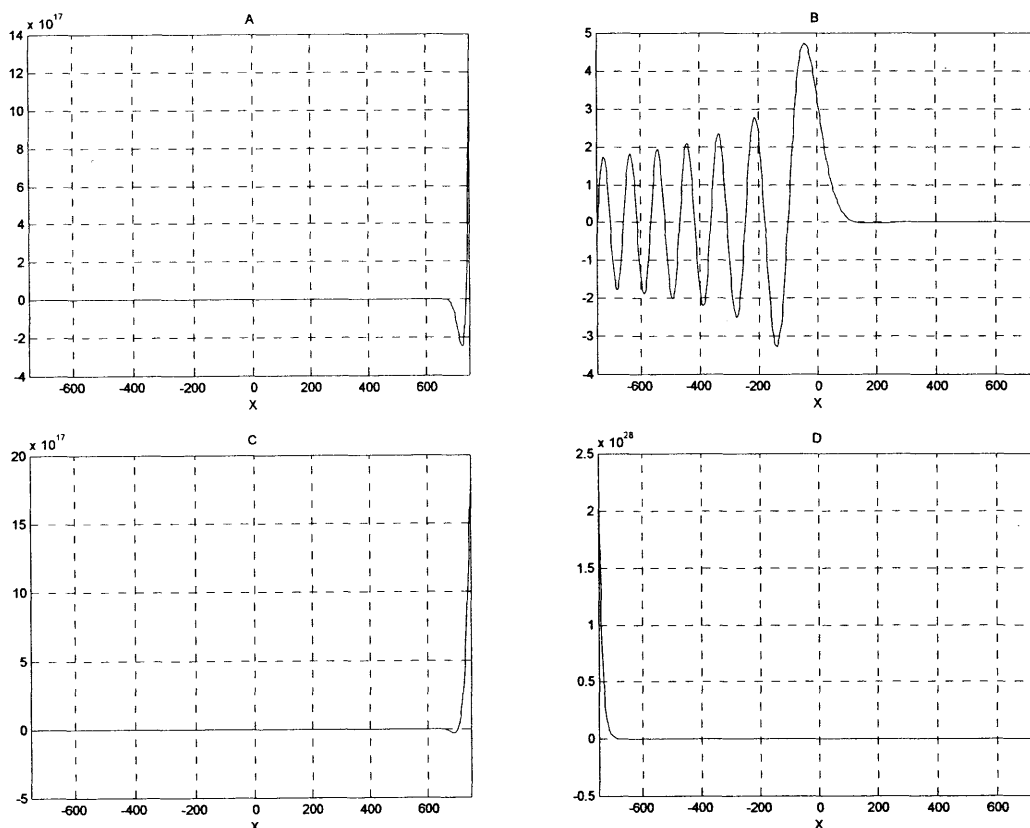


Figure 1.7. Four solutions for a typical tensioned beam with linearly varying spring constant.

145

# Appendix 2 Derivation of the Green's Function Solutions

For a curved riser under a top-end periodic motion, the loading (lift force due to vortices) along the riser is unsteady in time and varying in space, as shown in the previous chapter. We introduce Green's function method to solve this kind of problem. That is, we solve the impulse response first, and then use the convolution integral to obtain the solutions for arbitrary forcing functions. There are two types of Green's function as for our purpose: one of them is the response for a harmonic excitation, and the other is the response for a Dirac delta function in both time and space. Green's function for the second type is called the double Green's function. We will address each of these types separately in the following two sub-sections.

## 2.1 Green's Function for a Harmonic Excitation

The governing equation for a damped tensioned beam with an elastic foundation under a harmonic excitation at a single point can be written as:

$$EI\frac{\partial^4 y}{\partial x^4} - T\frac{\partial^2 y}{\partial^2 x} + m\frac{\partial^2 y}{\partial t^2} + c\frac{\partial y}{\partial t} + ky = \delta(x)e^{-i\omega t}, \qquad (2.1)$$

where $\delta(x)$ is the Dirac delta function located at $x = 0$. To illustrate how to proceed, we first consider a simpler case, an infinitely long tensioned beam under a harmonic excitation. The equation for this problem is written as:

$$EI\frac{\partial^4 y}{\partial x^4} - T\frac{\partial^2 y}{\partial^2 x} + m\frac{\partial^2 y}{\partial t^2} = \delta(x)e^{-i\omega t}. \qquad (2.2)$$

Assuming a harmonic response function $y(x,t) = Y(x)e^{-i\omega t}$, the equation becomes

$$EI\frac{d^4 Y}{dx^4} - T\frac{d^2 Y}{d^2 x} - m\omega^2 Y = \delta(x). \qquad (2.3)$$

The differential equation can be further simplified to an algebraic equation by integral transformation. The Fourier transform is suitable for this equation. The Fourier transform and its inverse we use are written as:

147

$$\overline{Y}(\gamma) = \frac{1}{\sqrt{2\pi}} \int_{-\infty}^{\infty} Y(x)e^{i\gamma x}dx,$$

$$Y(x) = \frac{1}{\sqrt{2\pi}} \int_{-\infty}^{\infty} \overline{Y}(\gamma)e^{-i\gamma x}d\gamma.$$

After the Fourier transformation, the equation becomes

$$EI\gamma^4\overline{Y} + T\gamma^2\overline{Y} - m\omega^2\overline{Y} = \frac{1}{\sqrt{2\pi}},$$  (2.4)

or

$$\overline{Y}(\gamma) = \frac{1}{\sqrt{2\pi}} \frac{1}{EI\gamma^4 + T\gamma^2 - m\omega^2}.$$  (2.5)

The inverse Fourier transform gives the solution

$$Y(x) = \frac{1}{2\pi} \int_{-\infty}^{\infty} \frac{e^{-i\gamma x}}{EI\gamma^4 + T\gamma^2 - m\omega^2} d\gamma.$$  (2.6)

We can evaluate the integral by the residue theory. The poles of the integrand satisfy

$$EI\gamma^4 + T\gamma^2 - m\omega^2 = 0.$$  (2.7)

This equation is exactly the dispersion relation for a tensioned beam. That is, the root loci we discussed in Section 3.2 are important for deciding the locations of poles for the Green's function solutions. As shown in Figure 3.3 (in the text), two roots for this dispersion relation are in the real axis while two other roots are in the imaginary axis:

$$\gamma = \pm\sqrt{\frac{-T + \sqrt{T^2 + 4m\omega^2 EI}}{2EI}}, \pm i\sqrt{\frac{T + \sqrt{T^2 + 4m\omega^2 EI}}{2EI}}.$$  (2.8)

The integration contour depends on the value of $x$. Due to the numerator of the integrand, the term $e^{-i\gamma x}$, we select the contours for $x > 0$ and $x < 0$ as shown in Figure 2.1. The added contours in the lower and the upper planes, respectively, are selected such that $e^{-i\gamma x}$ vanishes as the contour radii go to infinity. The figure shows that for $x > 0$, we have to add up the residues for $\gamma_3$ and $\gamma_4$, while for $x < 0$, we have to add up the residues for $\gamma_1$ and $\gamma_2$. The residue for $\gamma_3$ is

$$\text{Res}\Big|_{\gamma=\gamma_3} = \frac{e^{-i\gamma x}}{(EI\gamma^4 + T\gamma^2 - m\omega^2)/(\gamma - \gamma_3)}\Big|_{\gamma=\gamma_3}$$

$$= \frac{e^{i\sqrt{\frac{-T+\sqrt{T^2+4m\omega^2 EI}}{2EI}}\,x}}{-2\sqrt{T^2+4m\omega^2 EI}\,\sqrt{\dfrac{-T+\sqrt{T^2+4m\omega^2 EI}}{2EI}}}.$$

Similarly, we can get the residue for $\gamma_4$, which is

$$\text{Res}\Big|_{\gamma=\gamma_4} = \frac{e^{-\sqrt{\frac{T+\sqrt{T^2+4m\omega^2 EI}}{2EI}}\,x}}{2i\sqrt{T^2+4m\omega^2 EI}\,\sqrt{\dfrac{T+\sqrt{T^2+4m\omega^2 EI}}{2EI}}}.$$

Adding the contributions of these two residues together, we are able to write the solution for $x > 0$:

$$y(x,t) = Y(x)e^{-i\omega t} = \frac{1}{2\pi}e^{-i\omega t}(-2\pi i)\sum_{\gamma_3,\gamma_4}\text{Res}$$

$$= \frac{ie^{i\left(\sqrt{\frac{-T+\sqrt{T^2+4m\omega^2 EI}}{2EI}}\,x-\omega t\right)}}{2\sqrt{T^2+4m\omega^2 EI}\,\sqrt{\dfrac{-T+\sqrt{T^2+4m\omega^2 EI}}{2EI}}} - \frac{e^{-\sqrt{\frac{T+\sqrt{T^2+4m\omega^2 EI}}{2EI}}\,x}e^{-i\omega t}}{2\sqrt{T^2+4m\omega^2 EI}\,\sqrt{\dfrac{T+\sqrt{T^2+4m\omega^2 EI}}{2EI}}}. \qquad (2.9)$$

The first term of the solution is a propagating wave, while the second term is an evanescent wave. The similar procedure can be used in solving the solution for $x < 0$. Combining the solutions for $x > 0$ and $x < 0$, the unified solution can be written as:

$$y(x,t) = \frac{1}{2\sqrt{T^2+4m\omega^2 EI}}\left[\frac{ie^{i\left(\sqrt{\frac{-T+\sqrt{T^2+4m\omega^2 EI}}{2EI}}\,|x|-\omega t\right)}}{\sqrt{\dfrac{-T+\sqrt{T^2+4m\omega^2 EI}}{2EI}}} - \frac{e^{-\sqrt{\frac{T+\sqrt{T^2+4m\omega^2 EI}}{2EI}}\,|x|}e^{-i\omega t}}{\sqrt{\dfrac{T+\sqrt{T^2+4m\omega^2 EI}}{2EI}}}\right]. \qquad (2.10)$$

For a damped tensioned beam with an elastic foundation, we first locate the four poles of the integrand. The root loci in Section 3.2 provide the information about where these poles are and how the integration contour should be selected. Figure 2.2 shows an integration contour for $x > 0$. We can then follow the same procedure with the residue theory and obtain the solution:

$$y(x,t) = Y(x)e^{-i\omega t} = \frac{1}{2\pi}e^{-i\omega t}(-2\pi i)\sum_{\gamma_3,\gamma_4}\text{Res.} \tag{2.11}$$

The procedure is also valid for $x < 0$ and thus we are able to get the solution for all $x$.
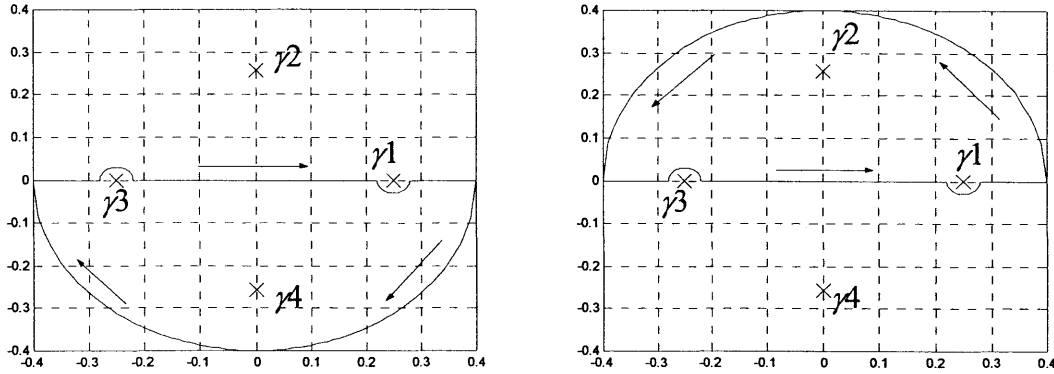


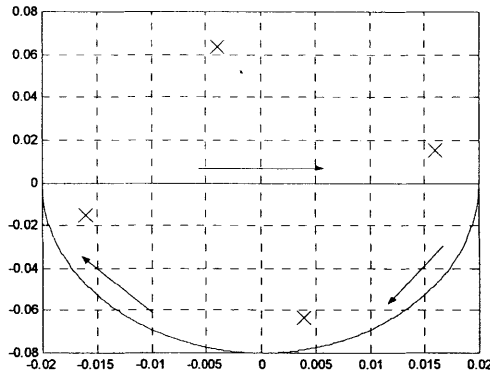Figure 2.1. The integration contours for a tensioned beam. The left panel is for $x > 0$ and the right panel is for $x < 0$.



Figure 2.2. The integration contours for a damped tensioned beam with an elastic foundation when $x > 0$.

For a finite system, we cannot use the Fourier transform in an infinite domain just developed above. We again use the tensioned beam without damping as an example, but now we set the region to be $0 < x < l$, where $l$ is the total length of the system. The governing equation is

$$EI\frac{\partial^4 y}{\partial x^4} - T\frac{\partial^2 y}{\partial^2 x} + m\frac{\partial^2 y}{\partial t^2} = \delta(x-\xi)e^{-i\omega t}, \tag{2.12}$$

where $\xi$ is the location of the sinusoidal excitation. The steady state solution of the problem can be written as $y(x,t) = Y(x)e^{-i\omega t}$, and inserting this solution into the equation, we get

$$EI\frac{d^4Y}{dx^4} - T\frac{d^2Y}{d^2x} - m\omega^2 Y = \delta(x-\xi), \qquad (2.13)$$

which is valid in $0 < x < l$. Due to the property of the Dirac delta function, Equation 2.13 can also be shown as

$$EI\frac{d^4Y}{dx^4} - T\frac{d^2Y}{d^2x} - m\omega^2 Y = 0, \qquad x \neq \xi. \qquad (2.14)$$

Solving Equation 2.14 for both sides of the delta function, we obtain

$$\begin{aligned}
Y_1(x) &= A_1 \sin\alpha_1 x + B_1 \cos\alpha_1 x + C_1 \sinh\alpha_2 x + D_1 \cosh\alpha_2 x, \quad 0 < x < \xi \\
Y_2(x) &= A_2 \sin\alpha_1 x + B_2 \cos\alpha_1 x + C_2 \sinh\alpha_2 x + D_2 \cosh\alpha_2 x, \quad \xi < x < l
\end{aligned} \qquad (2.15)$$

where

$$\begin{aligned}
\alpha_1 &= \sqrt{\frac{-T+\sqrt{T^2+4m\omega^2 EI}}{2EI}}, \\
\alpha_2 &= \sqrt{\frac{T+\sqrt{T^2+4m\omega^2 EI}}{2EI}}.
\end{aligned} \qquad (2.16)$$

In order to solve the eight coefficients, we need two boundary conditions at the left end, two boundary conditions at the right end, and four boundary conditions across the delta function. Around the point of the delta function, we can integrate Equation 2.13 and get

$$EI\int_{\xi-\varepsilon}^{\xi+\varepsilon} Y^{(4)}dx - T\int_{\xi-\varepsilon}^{\xi+\varepsilon} Y''dx - m\omega^2\int_{\xi-\varepsilon}^{\xi+\varepsilon} Ydx = 1, \qquad (2.17)$$

or

$$EIY'''\big|_{\xi-\varepsilon}^{\xi+\varepsilon} - TY'\big|_{\xi-\varepsilon}^{\xi+\varepsilon} - m\omega^2\int_{\xi-\varepsilon}^{\xi+\varepsilon} Ydx = 1. \qquad (2.18)$$

Because the displacement must be continuous, the last term of the right side vanishes. Also, if the first derivative of $Y$ does not vanish, the third derivative will blow up. Thus, the second term is zero and we have

$$Y_2'''(\xi) - Y_1'''(\xi) = \frac{1}{EI}. \qquad (2.19)$$

The other three boundary conditions at the location of the delta function are

151

$$Y_1(\xi) = Y_2(\xi),$$

$$Y_1'(\xi) = Y_2'(\xi),$$

$$Y_1''(\xi) = Y_2''(\xi).$$

(2.20)

To illustrate how to proceed for the Green's function solution, we assume pinned end boundary conditions for both ends of the tensioned beam. That is, we have the four boundary conditions

$$Y(0) = 0, Y''(0) = 0,$$

$$Y(l) = 0, Y''(l) = 0.$$

(2.21)

Imposing these four boundary conditions, we obtain the simplified solutions as

$$Y_1(x) = A_1 \sin \alpha_1 x + C_1 \sinh \alpha_2 x,$$

$$Y_2(x) = A_2(\sin \alpha_1 x - \tan \alpha_1 l \cos \alpha_1 x) + C_2(\sinh \alpha_2 x - \tanh \alpha_2 l \cosh \alpha_2 x).$$

(2.22)

Now the unknowns are reduced to four. Imposing the first and the third conditions of Equation 2.20, we get the relationships between coefficients:

$$A_1 = A_2(1 - \frac{\tan \alpha_1 l}{\tan \alpha_1 \xi}),$$

$$C_1 = C_2(1 - \frac{\tanh \alpha_2 l}{\tanh \alpha_2 \xi}).$$

(2.23)

Plugging these two relationships into Equation 2.22 and imposing the other two boundary conditions, we finally obtain the Green's function solutions for both sides of the Dirac delta function, written as:

$$Y_1(x) = \frac{1}{EI(\alpha_1^2 + \alpha_2^2)}[-\frac{(\tan \alpha_1 \xi - \tan \alpha_1 l)\cos \alpha_1 \xi \sin \alpha_1 x}{\alpha_1 \tan \alpha_1 l} +$$

$$+ \frac{(\tanh \alpha_2 \xi - \tanh \alpha_2 l)\cosh \alpha_2 \xi \sinh \alpha_2 x}{\alpha_2 \tanh \alpha_2 l}], \quad 0 < x < \xi$$

$$Y_2(x) = \frac{1}{EI(\alpha_1^2 + \alpha_2^2)}[-\frac{\sin \alpha_1 \xi(\sin \alpha_1 x - \tan \alpha_1 l \cos \alpha_1 x)}{\alpha_1 \tan \alpha_1 l} +$$

$$+ \frac{\sinh \alpha_2 \xi(\sinh \alpha_2 x - \tanh \alpha_2 l \cosh \alpha_2 x)}{\alpha_2 \tanh \alpha_2 l}], \quad \xi < x < l.$$

(2.24)

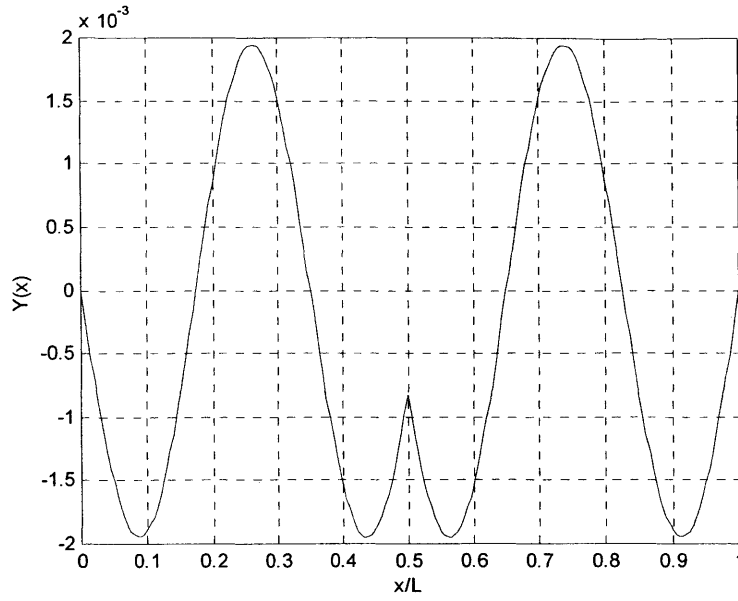An example of the Green's function solution is shown in Figure 2.3.

152

Figure 2.3. The Green's function solution of a tensioned beam for a sinusoidal excitation at the midpoint.

## 2.2 Double Green's Function

In order to solve the problem with arbitrary spatial and temporal excitation functions, we have to obtain the double Green's function and use convolution both in time and in space. We use a damped tensioned beam with elastic foundation to demonstrate this procedure. The governing equation is

$$EI\frac{\partial^4 y}{\partial x^4} - T\frac{\partial^2 y}{\partial x^2} + ky + c\frac{\partial y}{\partial t} + m\frac{\partial^2 y}{\partial t^2} = \delta(x - \xi)\delta(t),\tag{2.25}$$

where the forcing function is the Dirac delta functions both in time and in space. The system can be either finite or infinite. The solution for a finite system with pinned-pinned boundary conditions can be found in Graff (1991, pp. 178-179). We will develop a solution only for the infinite long tensioned beam here.

First we take the Fourier transform to convert the spatial parameter to $\gamma$ domain. The equation becomes

$$EI\gamma^4\bar{y} + T\gamma^2\bar{y} + k\bar{y} + c\frac{\partial\bar{y}}{\partial t} + m\frac{\partial^2\bar{y}}{\partial t^2} = \frac{e^{i\gamma\xi}}{\sqrt{2\pi}}\delta(t),\tag{2.26}$$

153

where $\bar{y}(\gamma,t)$ is the Fourier transform of $y(x,t)$. We then assume zero initial conditions and apply the Laplace transform to Equation 2.26, which becomes

$$EI\gamma^4 \bar{Y} + T\gamma^2 \bar{Y} + k\bar{Y} + sc\bar{Y} + s^2 m\bar{Y} = \frac{e^{i\gamma\xi}}{\sqrt{2\pi}}, \qquad (2.27)$$

where $\bar{Y}(\gamma,s)$ is the Laplace transform of $\bar{y}(\gamma,t)$. The transformed solution $\bar{Y}(\gamma,s)$ can be also written as

$$\bar{Y}(\gamma,s) = \frac{e^{i\gamma\xi}}{\sqrt{2\pi}m} \cdot \frac{1}{s^2 + 2\varsigma\omega_n s + \omega_n^2}, \qquad (2.28)$$

where

$$\omega_n^2 \equiv \frac{EI\gamma^4 + T\gamma^2 + k}{m},$$

$$2\varsigma\omega_n \equiv \frac{c}{m}. \qquad (2.29)$$

The inverse Laplace transform can be obtained by partial fractions and transform tables. The result is

$$\bar{y} = \frac{e^{i\gamma\xi}}{\sqrt{2\pi}m} \cdot \frac{1}{\beta - \alpha}(e^{-\alpha t} - e^{-\beta t}), \qquad (2.30)$$

where

$$\alpha = \omega_n(\varsigma + i\sqrt{1 - \varsigma^2}),$$

$$\beta = \omega_n(\varsigma - i\sqrt{1 - \varsigma^2}). \qquad (2.31)$$

This solution is valid for $\varsigma < 1$. We then need the inverse Fourier transform to determine the double Green's function. The double Green's function for this infinitely long tensioned beam with damping and elastic foundation is

$$G(x,t;\xi) = \frac{e^{-\frac{c}{2m}t}}{2\pi m} \int_{-\infty}^{\infty} \frac{e^{i\gamma(\xi - x)}}{\omega_d} \sin\omega_d t\, d\gamma, \qquad (2.32)$$

where

$$\omega_d = \sqrt{\frac{EI\gamma^4 + T\gamma^2 + k}{m} - \frac{c^2}{4m^2}}. \qquad (2.33)$$

154

Equation 2.32 is the double Green's function and it can be evaluated numerically. For the response of an arbitrary loading $q(x,t)$, we have to use this double Green's function and apply the convolution integral with the form:

$$y(x,t) = \int_0^t d\tau \int_{-\infty}^{\infty} d\xi G(x, t - \tau; \xi) q(\xi, \tau) d\xi. \tag{2.34}$$

Thus, we are able to calculate the response of any kind of unsteady forces applied to the system. This is a useful formula for us to compute the VIV response under an unsteady current.

# Appendix 3 Time Domain Response Simulation for the Unsteady VIV

To obtain the response solutions using Equation 2.34, we have to develop a model for the loading $q(x,t)$ under top-end periodic motions. From Section 5.4, we learned that the response frequencies change with time, due to the sinusoidally varying velocities. The St number is approximately invariant during the motion cycle. The frequency variations have been modeled by Bearman *et al.* (1984). We approach this problem with a similar but modified technique so that the forcing function is smooth in time.

We first focus on the loading at one point, and later we will discuss the spatial variations due to the non-uniform flow profile. The flow velocity at a point can be written as

$$V = V_0 \sin \Omega t, \tag{2.1}$$

where $V_0$ is the velocity amplitude, which varies along the riser, and the frequency $\Omega$ is the top-end excitation frequency, the same value along the riser. A novel model for the shedding frequencies is proposed here:

$$\omega = \omega_0 [\sin(2\Omega t - \frac{\pi}{2}) + 1], \tag{2.2}$$

which is plotted in Figure 3.1. By the St relationship we determine the frequency amplitude $\omega_0$ as

$$\omega_0 = \frac{\pi St V_0}{D}. \tag{2.3}$$

As shown in the figure, the maximum velocities ($\pm 1$ m/s) have the corresponding maximum shedding frequencies. By using this model, the time evolution of the frequency is smooth and the artificial effect of a discontinuous function to the response calculation is eliminated.
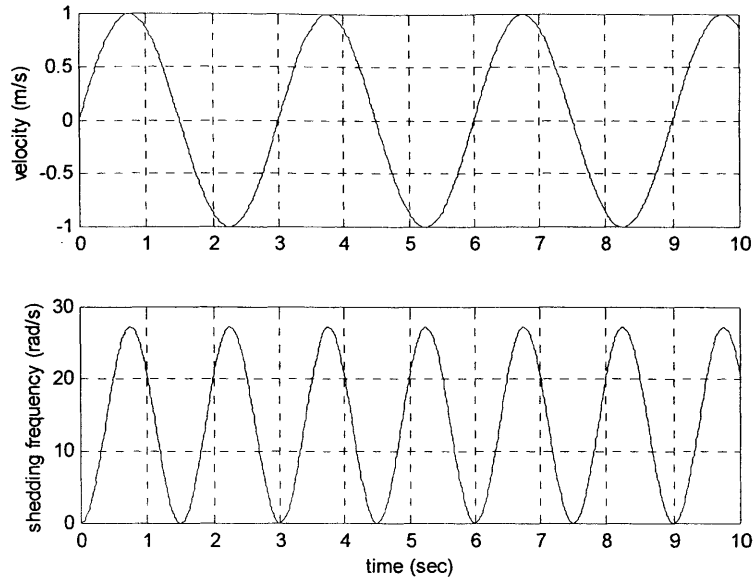
Figure 3.1. The inline flow velocity at a point and the corresponding shedding frequency model. The amplitude of the velocity is 1 m/s and the period is 3 sec.

The lift force per unit length at this location is modeled as

$$F(x,t) = \frac{1}{2} \rho_f DU^2 C_L \sin\left( \int_0^t \omega(\tau)d\tau \right). \tag{2.4}$$

The integral inside the sinusoidal function is due to the variation in time of the frequencies. The velocity $U$ now can be expressed as the shedding frequency by the St relationship:

$$U(t) = \frac{\omega(t) \cdot D}{2\pi St}. \tag{2.5}$$

We also assume a constant lift coefficient 0.5 for a simplified simulation. The time evolution of this force model is shown in Figure 3.2 At the times when the velocities are large, both the frequencies and the amplitude are large according to the model in Equation 3.4.
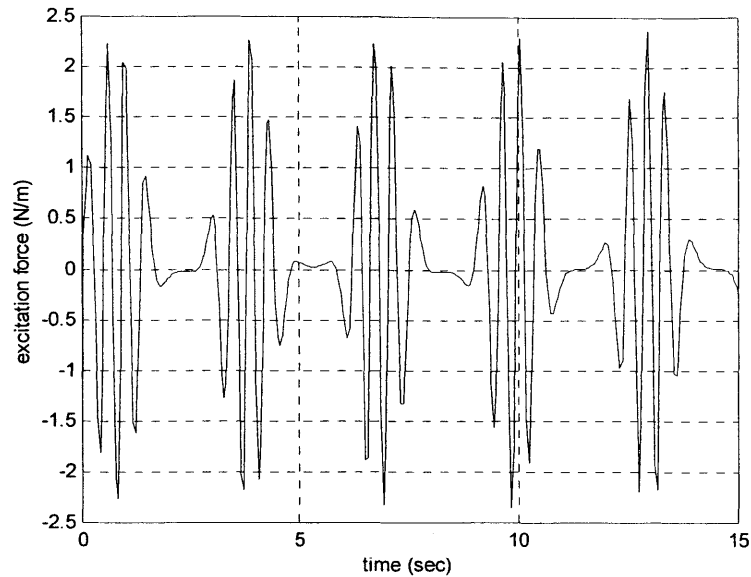
Figure 3.2. The unsteady force model at a single point. The top-end period is 3 sec.

The spatial effects due to the velocity profile should also be considered in the forcing model. We discretize the velocity profile to have fewer sections along the length. A discretized velocity profile for a CVAR test (the original profile is shown in Figure 1.5 (text)) and the corresponding maximum forces obtained from Equation 3.4 are shown in Figure 3.3. It can be seen that the larger forces are concentrated around the center portion of the riser, while the excitations at both sides are negligible. In addition to the amplitudes of the forces along the riser, we also have to assign the phase for the force at each location. This issue is very complicated requiring knowledge of the correlation length of the unsteady VIV. However, this correlation problem is not yet well understood. We thus propose a preliminary model for the phases. We assume the phase is the same for portions with the same maximum amplitudes, while the phase for each portion with different maximum amplitudes is randomly assigned. Several snapshots of the excitation forces are shown in Figure 3.4.
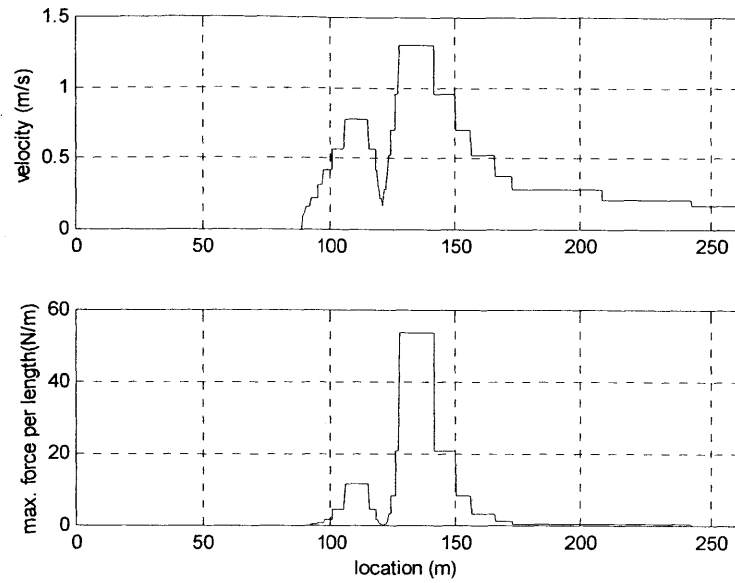
Figure 3.3. The digitized velocity profile for a CVAR test and the corresponding maximum force per unit length at each location.
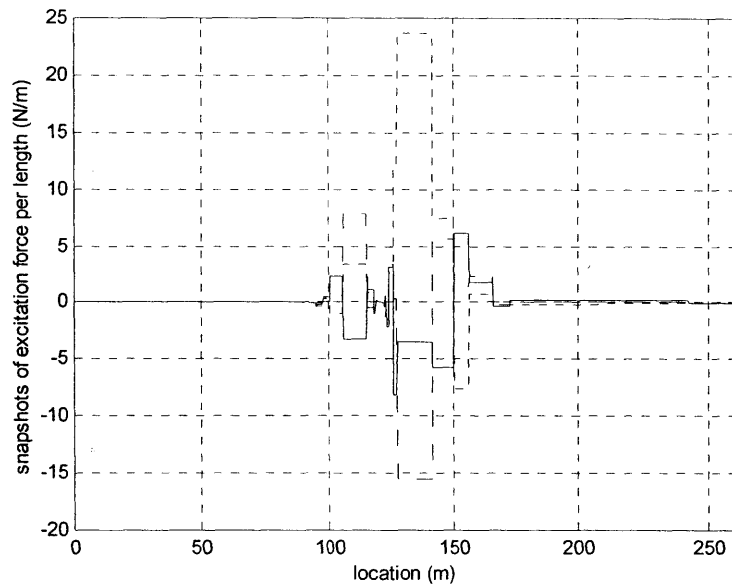


Figure 3.4. Three snapshots of the excitation forces per unit length. This force model is used for calculating the response for unsteady VIV.

160

With Green's function and the forcing model, we are able to calculate the dynamic response under the top-end periodic excitation. Figure 3.5 shows a snapshot of the response to an unsteady force at a single point $x = 0$. The time series of the force is shown in Figure 3.2. Because the system is a tensioned beam, the waves are dispersive. The high frequency components travel faster than the low frequency components. As can be seen in Figure 3.5, at both ends (toward $x = \pm 1$) the wave frequencies are high. The waves with large amplitudes at around $x = \pm 0.15$ come from just shed vortices associated with the peak inline velocity. The waves with large amplitudes at around $x = \pm 0.5$ are associated with the previous peak inline velocity, while the envelope shapes of these waves are distorted due to the dispersive characteristics and the system damping. From this snapshot, we can imagine that the response of the riser accounting for all the unsteady excitations along the whole riser will be very complicated.
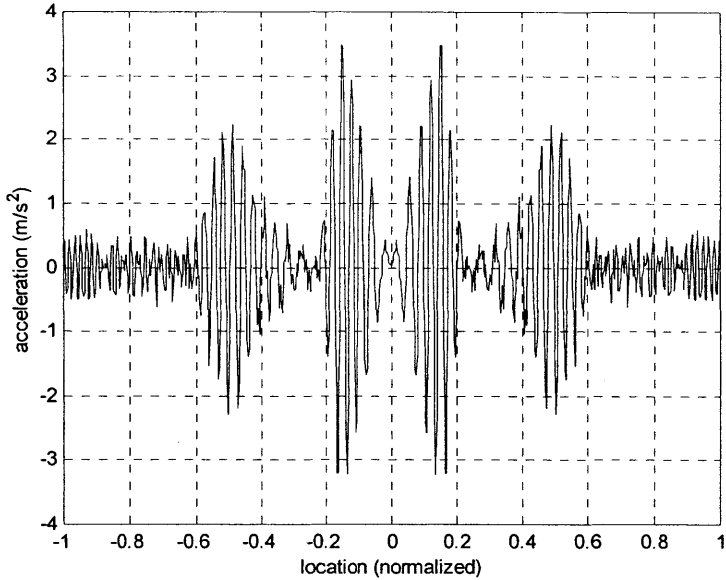


Figure 3.5. A snapshot of the calculated response under unsteady excitations at a point.

Figure 3.6 shows the times series of the experimental as well as the predicted response of the CVAR riser with respect to the top-end motion induced unsteady VIV. The response is at the location of pup 3 for the top-end excitations with the amplitude 3 ft and the period 5 sec. The two time series demonstrate similar patterns. At certain times, the

161

accelerations have large amplitudes with high frequencies, which is associated with the large inline velocity from the principal power-in region. The duration of the high frequency components tend to be longer for the predicted response. Also, the predicted accelerations are generally larger than the measurement, so this is an over-predicted model by a factor of about 1.5 to 2. Figure 3.7 displays a snapshot of the calculated response under unsteady excitations for the CVAR velocity profile with top-end amplitude 3 ft, top-end period 5 sec. The results are a sum of the response due to the unsteady excitation everywhere in the riser. From this figure we see that the response at the center portion is higher than that at both ends. This phenomenon is directly related to the flow profile of CVAR, which has the major power-in region at around $x = 0.45 : 0.55$. The time domain simulation, while not able to be shown in the thesis, is available upon request.
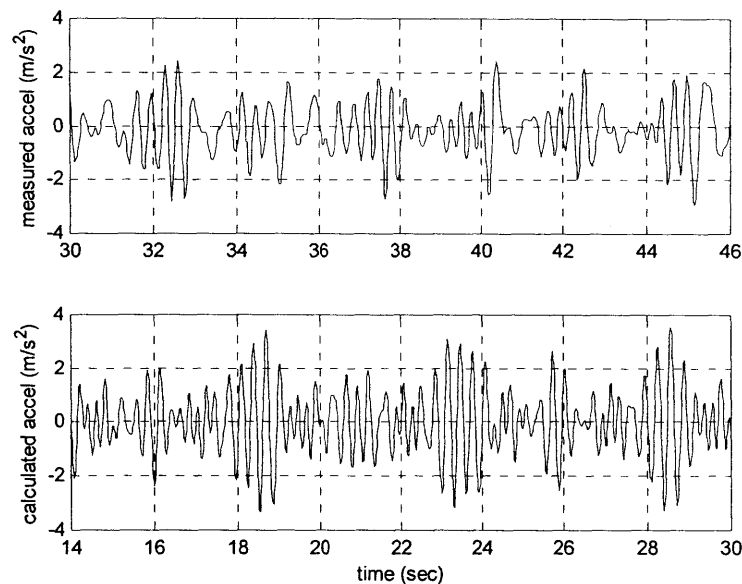


Figure 3.6. Time series for measured and calculated accelerations. The measured and the calculated accelerations are both for CVAR, top-end amplitude 3 ft, top-end period 5 sec. The measurement is at pup 3.
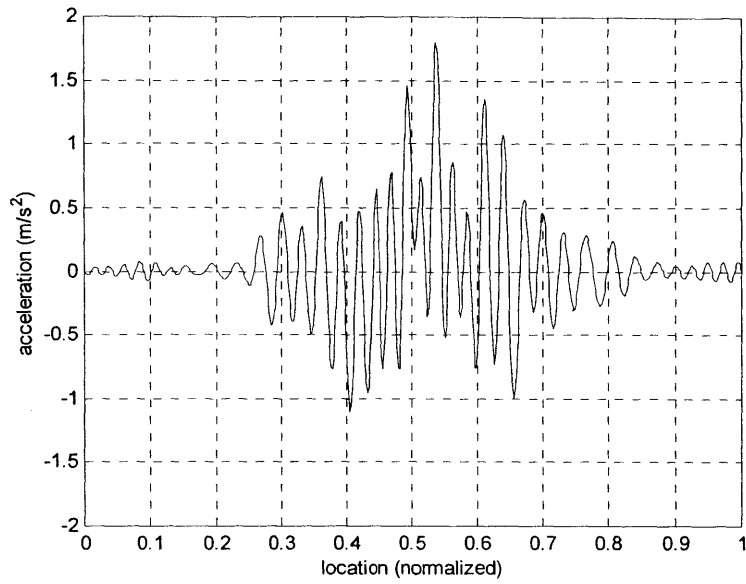
162

Figure 3.7. A snapshot of the calculated response under unsteady excitations for the CVAR velocity profile with top-end amplitude 3 ft, top-end period 5 sec.

# Reference

Bearman, P. W. 1984 Vortex Shedding from Oscillating Bluff Bodies. *Ann. Rev. Fluid Mech.*, **16,** pp195-222.

Bearman, P. W., Graham, J. M. R. and Obasaju, E. D. 1984 A Model Equation for the Transverse Forces on Cylinders in Oscillatory Flows, *Appl. Ocean Res.*, **6,** pp 166-172.

Blevins, R. D. 1990 *Flow-induced vibrations*. Van Nostrand.

Ferrari, J. A. and Bearman, P. W. 2000 Multi-modal Behavior of Deepwater Risers, Workshop on Vortex-induced Vibrations of Offshore Structures, Sao Paulo, Brazil, August 2000.

Graff, K. F. 1991 *Wave Motion in Elastic Solids*. Dover.

Griffin, Owen M. 1980 Cold Water Pipe Design for Problems Caused by Vortex-Excited Oscillations. *OTEC,* Naval Research Laboratory, Washington, D.C., March 14, 1980

Griffin, O. M. Vortex-induced Vibrations of Marine Cables and Structures, NRL Memorandum Report 5600.

Hartlen, R. T. and Currie, I. G. 1970 Lift Oscillator Model of Vortex-induced Vibration. *J. Eng. Mech. Div., ASCE,* **96,** (EM8), 577-591.

Justesen, P. 1989 Hydrodynamic forces on large cylinders in oscillatory flow. *Journal of Waterway, Port, Coastal and Ocean Engineering, ASCE* **115(4),** 497-514.

Kozakiewicz, A., Fredsoe, J. and Sumer, B. M. 1995 Forces on pipelines in oblique attack. Steady current and waves. Proceedings of 5th International Offshore and Polar Engineering Conference, The Hague, Netherlands, June 11-16, 1995, Vol. II, 174-183.

Richardson, K. 2001 A New Application of the Reduced Damping Parameter to Flow-Induced Vibration of Long Cylinders. B.S. Thesis, Massachusetts Institute of Technology.

Sarpkaya, T. and Isaacson, M. de St. Q. 1979 *Wave Forces on Offshore Structures – Theory and Application.*

Sarpkaya, T. 1976 In-line and transverse forces on smooth and sand-roughened cylinders in oscillatory flow at high Reynolds numbers. Naval Postgraduate School, Monterey, CA, Tech. Rep. NPS-69SL76062.

Sarpkaya, T. 1986 Force on a circular cylinder in viscous oscillatory flow at low Keulegan-Carpenter numbers. *Journal of Fluid Mechanics* **165,** 61-71.

Sumer, B. M. and Fredsoe, J. 1988 Transverse vibrations of an elastically mounted cylinder exposed to an oscillating flow. *Journal of Offshore Mechanics and Arctic Engineering, ASME,* **110,** 387-394.

Triantafyllou, M. S. 1991 Dynamics of cables, towing cables, and mooring systems. *The Shock and Vibration Digest,* **23(7),** 3-8.

Vandiver, J. Kim 1997 *SHEAR7 Program Theoretical Manual.* MIT Department of Ocean Engineering.

Vandiver, J. K. 1993 Dimensionless parameters important to the prediction of vortex-induced vibration of long, flexible cylinders in ocean currents. *Journal of Fluids and Structures* **7,** 423-455.

Venugopal, M. 1996 Damping and Response Prediction of a Flexible Cylinder in a Current, Doctoral Dissertation, Massachusetts Institute of Technology.

Williamson, C. H. K. 1985 Sinusoidal flow relative to circular cylinders. *Journal of Fluid Mechanics* **155,** 141-174.

Williamson, C. H. K. and Roshko, A. 1988 Vortex formation in the wake of an oscillating cylinder. *Journal of Fluids and Structures* **2,** 355-381.